Quantitative Susceptibility Mapping and Susceptibility-based Distortion Correction of Echo Planar Images

by

Clare Poynton

B.S., Biomedical Engineering
Johns Hopkins University (2004)

Submitted to the Harvard-MIT Division of Health Sciences and Technology
in partial fulfillment of the requirements for the degree of

Doctor of Philosophy in Medical Engineering

at the

MASSACHUSETTS INSTITUTE OF TECHNOLOGY

February 2012

Author .....
Harvard-MIT Division of Health Sciences and Technology
January 27, 2012

Certified by .....
William Wells III
Associate Professor of Radiology, Harvard Medical School and Affiliated Faculty of the Harvard-MIT Division of Health Sciences and Technology
Thesis Supervisor

Accepted by .....
Ram Sasisekharan
PhD/Director, Harvard-MIT Division of Health Sciences and Technology/Edward Hood Taplin Professor of Health Sciences & Technology and Biological Engineering

Quantitative Susceptibility Mapping and Susceptibility-based Distortion Correction of Echo Planar Images

by

Clare Poynton

Submitted to the Harvard-MIT Division of Health Sciences and Technology
on January 27, 2012, in partial fulfillment of the
requirements for the degree of
Doctor of Philosophy in Medical Engineering

Abstract

The field of medical image analysis continues to expand as magnetic resonance imaging (MRI) technology advances through increases in field strength and the development of new image acquisition and reconstruction methods. The advent of echo planar imaging (EPI) has allowed volumetric data sets to be obtained in a few seconds, making it possible to image dynamic physiological processes in the brain. In order to extract meaningful information from functional and diffusion data, clinicians and neuroscientists typically combine EPI data with high resolution structural images. Image registration is the process of determining the correct correspondence.

Registration of EPI and structural images is difficult due to distortions in EPI data. These distortions are caused by magnetic field perturbations that arise from changes in magnetic susceptibility throughout the object of interest. Distortion is typically corrected by acquiring an additional scan called a fieldmap. A fieldmap provides a direct measure of the magnetic perturbations, allowing distortions to be easily computed and corrected. Fieldmaps, however, require additional scan time, may not be reliable in the presence of significant motion or respiration effects, and are often omitted from clinical protocols.

In this thesis, we develop a novel method for correcting distortions in EPI data and registering the EPI to structural MRI. A synthetic fieldmap is computed from a tissue/air segmentation of a structural image using a perturbation method and subsequently used to unwarp the EPI data. Shim and other missing parameters are estimated by registration. We obtain results that are similar to those obtained using fieldmaps, however, neither fieldmaps nor knowledge of shim coefficients is required. In addition, we describe a method for atlas-based segmentation of structural images for calculation of synthetic fieldmaps. CT data sets are used to construct a probabilistic atlas of the head and corresponding MRI is used to train a classifier

that segments soft tissue, air, and bone. Synthetic fieldmap results agree well with acquired fieldmaps: 90% of voxel shifts show subvoxel disagreement with those computed from acquired fieldmaps. In addition, synthetic fieldmaps show statistically significant improvement following inclusion of the atlas.

In the second part of this thesis, we focus on the inverse problem of reconstructing quantitative magnetic susceptibility maps from acquired fieldmaps. Iron deposits change the susceptibility of tissue, resulting in magnetic perturbations that are detectable with high resolution fieldmaps. Excessive iron deposition in specific regions of the brain is associated with neurodegenerative disorders such as Alzheimer's and Parkinson's disease. In addition, iron is known to accumulate at varying rates throughout the brain in normal aging. Developing a non-invasive method to calculate iron concentration may provide insight into the role of iron in the pathophysiology of neurodegenerative disease. Calculating susceptibility maps from measured fieldmaps is difficult, however, since iron-related field inhomogeneity may be obscured by larger field perturbations, or 'biasfields', arising from adjacent tissue/air boundaries. In addition, the inverse problem is ill-posed, and fieldmap measurements are only valid in limited anatomical regions.

In this dissertation, we develop a novel atlas-based susceptibility mapping (ASM) technique that requires only a single fieldmap acquisition and successfully inverts a spatial formulation of the forward field model. We derive an inhomogeneous wave equation that relates the Laplacian of the observed field to the D'Alembertian of susceptibility, and eliminates confounding biasfields. The tissue/air atlas we constructed for susceptibility-based distortion correction is applied to resolve ambiquity in the forward model arising from the ill-posed inversion. We include fourier-based modeling of external susceptibility sources and the associated biasfield in a variational approach, allowing for simultaneous susceptibility estimation and biasfield elimination. Results show qualitative improvement over two methods commonly used to infer underlying susceptibility values and quantitative susceptibility estimates show stronger correlation with postmortem iron concentrations than competing methods.

Thesis Supervisor: William Wells III
Title: Associate Professor of Radiology, Harvard Medical School and Affiliated Faculty of the Harvard-MIT Division of Health Sciences and Technology

Acknowledgments

I would like to acknowledge my thesis adviser, Sandy Wells, for his direct contributions to this work and outstanding mentorship throughout my time at MIT. He made many positive contributions to my intellectual development and overall experience in graduate school for which I am sincerely grateful. I would also like to thank my thesis committee members: Mark Jenkinson, Elfar Adalsteinsson, and Greg Sorensen. I would like to thank Mark for letting me spend time with his group in Oxford and for his mentorship over the past six years. Mark's collaboration was enormously valuable to me, especially in guiding the early development of this research. I would like to acknowledge Elfar for his advice on quantitative susceptibility mapping, for his overall enthusiastic support, and for connecting me with Adolf Pfefferbaum, who graciously provided the data that made the latter part of this work possible. I would like to thank Greg for insightful discussions about the clinical implications of this research, especially for integrated MR-PET systems and perfusion imaging.

I would like to acknowledge Polina Golland for providing funding and support for this work throughout my time at CSAIL. I would like to thank Carlo Pierpaoli for contributing to thoughtful discussions regarding this research and for providing us with excellent DTI data. Alex Golby let me observe several neurosurgeries during my time at MIT and contributed valuable clinical data to this work, which was supported in part by the Surgical Planning Laboratory at Brigham and Women's Hospital. I would like to thank my mentors in college, especially Mike McCaffery and Tilak Ratnanather, for their teaching and encouragement. Finally, I would like to thank my life-long friends and family, especially my mother, brother, and sister for their love and loyalty.

Contents

List of Figures

Chapter 1

Introduction

1.1 Medical Image Analysis

The field of medical image analysis continues to expand as new imaging modalities, acquisition, and reconstruction methods are developed. Advances in medical image processing are providing neuroscientists and clinicians with powerful tools to investigate neurobiological function in both health and disease. Medical imaging technologies such as positron emission technology (PET), electroencephalography (EEG), or magnetoencephalography (MEG) provide primarily functional information about the brain, while modalities such as computed tomography (CT) and x-ray provide images of anatomical structure. In contrast, magnetic resonance imaging (MRI) is unique in its versatility, providing structural or functional information depending on the pulse sequence that is used.

In order to extract meaningful information from neuroimaging data, clinicians and neuroscientists typically combine low resolution functional data with high resolution structural images. Image registration algorithms provide a means for obtaining the correct correspondence between data sets. Registration is necessary for comparing information from multiple modalities or time points for the same subject, and for evaluating differences across subjects. Registration is a problem of critical importance in medical imaging, since registration errors may reduce the accuracy of any subsequent analysis. Since different imaging methods produce data that vary in intensity

properties, artifacts and sensitivity to underlying physical properties, the challenges of a particular registration problem depend primarily on the type of images involved (ie. structural MRI and CT). Once accurate registration results are obtained, further analysis such as segmentation of specific brain regions, voxel-based morphometry, calculation of cortical thickness, estimation of diffusion tensors, or quantitative susceptibility mapping (QSM) can be performed.

1.2 Thesis Overview

The focus of this thesis is on modeling the relationship between magnetic susceptibility and the observed magnetic field. Specifically, we aim to solve two closely related problems: the correction of susceptibility-based distortion in echo planar images (EPI), and the reconstruction of quantitative susceptibility maps of the brain. Correcting susceptibility-based distortion in EPI is necessary for obtaining accurate registration of functional and structural neuroimaging data. Quantifying susceptibility differences in specific brain regions arising from iron deposition may provide valuable insight into normal aging and neurodegenerative disease.

1.2.1 Susceptibility-based Distortion Correction of EPI Data

In the first part of this thesis we investigate the problem of registering EPI data to structural MRI. EPI is a widely used pulse sequence for obtaining functional MRI (fMRI) and diffusion tensor imaging (DTI) data [82]. Its high temporal resolution allows an entire volume to be acquired in a few seconds, making it possible to image dynamic physiological processes in the brain. Acquiring EPI data over multiple time points in fMRI experiments allows the blood oxygen level dependent (BOLD) effect to be measured, which is correlated with underlying neuronal activity [88]. Similarly, acquiring EPI data with multiple directions of diffusion weighting allows DTI data to be reconstructed, providing information about the underlying tissue microstructure. Accurate registration of EPI and structural MRI is critical in FMRI and DTI studies, but difficult to achieve due to magnetic susceptibility differences that cause distortions

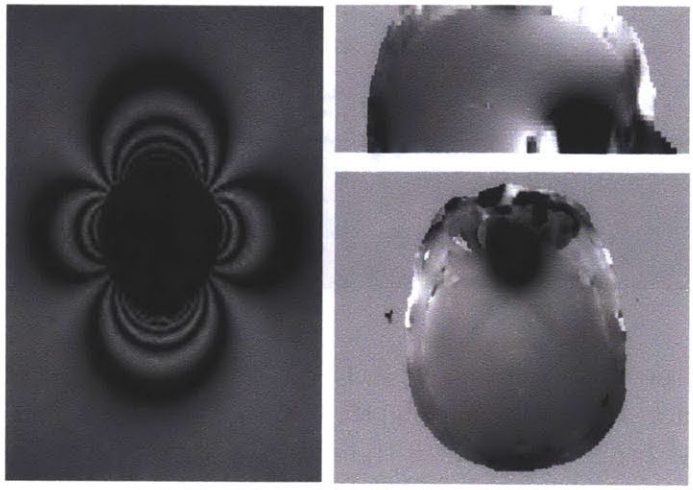

(a) (b)

Figure 1-1: Field perturbations caused by susceptibility boundaries. An air-filled ping-pong ball immersed in water creates perturbations in the magnetic field that extend out from the air/water interface as shown by the fieldmap in (a) [115]. Similar field perturbations are found near the air-filled sinuses in the human head as shown in the sagittal (top) and axial (bottom) views of the fieldmap in (b).

in EPI data.

Magnetic Susceptibility

EPI distortions are caused by magnetic field perturbations that arise from changes in magnetic susceptibility throughout the object of interest. Magnetic susceptibility, χ, is a physical property that describes the extent to which a material becomes magnetized when placed in an external magnetic field. In biological samples there is an important susceptibility difference between tissue and air. Soft tissue and bone are diamagnetic with susceptibilities of approximately $\chi_{tissue} = -9.1 \times 10^{-6}$ and $\chi_{bone} = -11.4 \times 10^{-6}$, while air is paramagnetic, $\chi_{air} = 0.4 \times 10^{-6}$ [62, 50]. Magnetic susceptibility is a unitless quantity that is often expressed in parts per million (ie. -9.1 ppm). When a diamagnetic sample is placed in the MRI scanner, it will generate a local magnetic field that opposes the direction of the external field. A paramagnetic material will augment the applied field by generating a local magnetic field that is parallel to it. As a result, substantial perturbations in the field arise at boundaries between materials with large susceptibility differences such as tissue/air

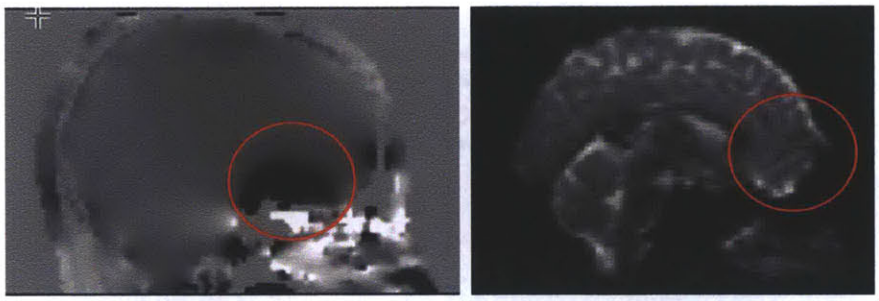

(a) (b)

Figure 1-2: Field perturbations result in EPI distortion. Tissue/air interfaces around the sinuses produce field perturbations that extend into the inferior frontal and temporal lobes of the brain as shown in the circled area of the fieldmap (a). The field inhomogeneity produces distortion in EPI data that is primarily constrained to be along the phase-encode axis. This is shown by the anterior/posterior deformation of the EPI data in (b).

interfaces. Fig. 1-1a shows an image of the magnetic field (or 'fieldmap') obtained after an air-filled ping-pong ball is placed in water. Large perturbations in the field can be seen near the water/air boundary. Similarly, the human head contains tissue/air boundaries near the auditory canals and the sphenoid, ethmoid, and frontal sinuses. This results in large perturbations in the field that extend into the frontal and temporal lobes of brain as shown in Fig. 1-1b.

Distortion in Echo Planar Images

In MRI experiments, perturbations in the local magnetic field can in principle be computed from the phase of the MR signal. In a dual gradient echo sequence, the field inhomogeneity is proportional to the difference in the MR phase divided by the difference in echo times of the two gradient echo acquisitions [63]. Due to the design of EPI sequences, magnetic field inhomogeneities result in signal loss and geometric distortion of the reconstructed images [63, 53, 118, 18]. The distortion at each location is proportional to the field inhomogeneity at that position and is typically constrained to be a 'pixel shift' along the phase-encode direction. For example, field perturbations in the inferior frontal lobe of the brain (Fig. 1-2a) produce distortion in the anterior/posterior direction of EPI data (Fig. 1-2b). Previous studies have shown that

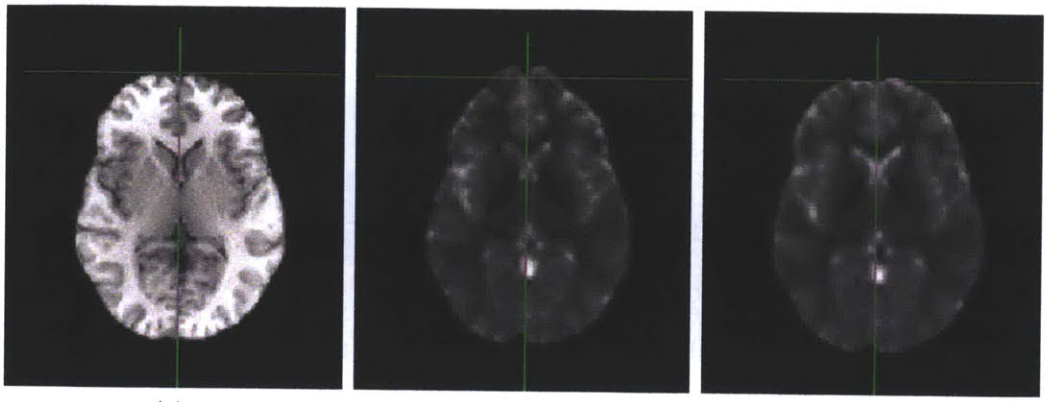

(a) (b) (c)

Figure 1-3: Fieldmap-based Distortion Correction. A structural MRI (a) and distorted EPI (b) show substantial differences in shape especially in the anterior region of the brain. Correcting the distortion using an acquired fieldmap results in the EPI shown in (c) and allows accurate registration of the corrected EPI to structural MRI.

correcting geometric distortion in EPI data increases the accuracy of co-registration to structural MR [30, 53]. Accurate registration is necessary for precise anatomical localization of functional activation computed from EPI data. This is especially important in single-subject studies (ie. pre-surgical evaluation) [53]. Therefore, field inhomogeneity and distortion is a significant problem in functional neuroimaging.

Fieldmap-based Distortion Correction

EPI distortion is typically corrected by acquiring an additional scan called a fieldmap. A fieldmap provides a direct measure of the field inhomogeneity, allowing distortions to be directly computed from the image and applied to correct the EPI [63]. Examples of a T1-weighted structural MRI, distorted EPI, and EPI following correction with a measured fieldmap are shown in Fig. 1-3. Unlike the distorted EPI, the shape of the corrected EPI closely resembles that of the structural image; the effect of unwarping is most evident in the anterior region of the brain. After correction, the EPI can be registered to the structural image or other medical imaging data sets.

1.2.2 Atlas-based Quantitative Susceptibility Mapping

Recently, there has been increasing evidence that iron accumulation in specific regions of the brain is implicated in neurodegenerative disorders such as Parkinson's, Alzheimer's, and Multiple Sclerosis [125, 85, 72, 75, 57, 90]. Iron is involved in many metabolic and cellular functions throughout the body, but the transport of iron into the brain, the regulation of iron homeostasis, and its role in the pathophysiology of neurodegenerative disease remains unknown. Iron enters the blood stream by absorption from the gastrointestinal tract and is transported across the blood-brain barrier (BBB) by a mechanism that is still poorly understood [20]. Within the brain, the concentration of iron varies substantially between brain regions and throughout the lifespan [3, 5]. Regions of the brain that are associated with motor functions (extrapyramidal regions) tend to have more iron than non-motor regions, suggesting iron imbalance may be linked to movement disorders [70]. Iron is involved in myelin synthesis [20] and the normal function of neuronal tissue. For example, it serves as a cofactor for essential proteins such as the enzyme tyrosine hydroxylase, which is required for dopamine synthesis. Elevated amounts of iron in the brain is hypothesized to cause oxidative-stress induced neurodegeneration [125]. While increasing iron concentration in neurodegenerative disease and normal aging was first described in histopathological studies (a review of these early studies can be found in [70]), non-invasive imaging methods such as MRI and ultrasound are now being applied to study iron distribution in-vivo [4, 6, 5, 46, 44, 123, 91, 98, 11, 124].

Since iron is ferromagnetic, iron deposits cause small changes in the magnetic susceptibility of tissue that measurably affect the local field and corresponding phase of the MR signal. These field pertubations can be modeled as the convolution of a dipole-like kernel with the spatial susceptibility distribution. In the fourier domain, the kernel exhibits zeros along a conical surface, which prevents direct inversion of the fieldmap (by complex division) and makes the problem ill-posed. In addition, the field can only be measured in regions where the MR signal is valid (ie. soft tissue). The result is a challenging ill-posed inverse problem [79]. Furthermore, it is critical

to note that susceptibility differences between normal brain tissue (which is assumed to have approximately the same susceptibility as water) and iron-rich tissue is more than an order of magnitude less than the susceptibility difference between tissue and air ($\chi_{tissue} - \chi_{air} \approx -9.5$ ppm). As a result, field perturbations due to tissue/air interfaces create a background field that obscures the subtle iron-related effects of interest. This background field is often referred to simply as B_0 inhomogeneity [51, 35], but we will refer to it as the 'biasfield' in analogy to the biasfield observed in MR intensity data as a result of $B1$ inhomogeneity [120]. Non-local field effects from the neck and torso, imperfect shimming meant to improve field homogeneity, and changes in respiration also contribute to the biasfield and corrupt the phase effects of interest. Thus, eliminating biasfields is critical for accurate susceptibility estimation. Susceptibility values can be inferred from MRI data using methods that compute parameters closely related to underlying susceptibility values, or they can be estimated directly using quantitative susceptibility mapping (QSM) techniques.

Susceptibility Mapping: Initial Techniques

Early approaches to susceptibility mapping allowed susceptibility differences to be inferred from closely related parameters such as relaxation rates or phase. For example, in susceptibility-weighted imaging (SWI), developed by Haacke et al., the observed phase is high-pass filtered to remove biasfields as shown in Fig. 1-4a. The filtered phase and magnitude data are then combined to produce a composite image which enhances the susceptibility-related phase constrast [47, 46].

A second important susceptibility-related technique is the field-dependent transverse relaxation rate increase (FDRI) [4]. FDRI has a high specificity for ferritin, which is responsible for storing the largest fraction of iron in the brain that is not found in hemoglobin or iron-containing enzymes (non-haem iron)[3]. The ferritin complex consist of a multi-subunit protein shell (apoferritin) surrounding a crystalline core of hydrous ferric oxide that may be made up of as many as 4500 ferric iron atoms [105]. Ferritin has been shown to exert a strong magnetic effect that results in marked T2 shortening in-vitro [69, 68, 89] and in-vivo [106, 19]. In FDRI, maps of the transverse

relaxation rate ($R_2 = 1/T_2$) are computed from spin-echo EPI acquisitions obtained at two different field strengths (ie. 1.5 and 3 Tesla). The difference in R_2 divided by the difference in field strength gives the FDRI (Fig. 1-4b). In-vivo and in-vitro experiments have demonstrated that FDRI is a specific quantitative measure of tissue ferritin content [4].

Quantitative Susceptibility Mapping

Recently several methods have been developed to directly solve the inverse problem and provide quantitative estimates of magnetic susceptibility from measured fieldmaps [31, 79, 98]. These methods invert a fourier model relating susceptibility to magnetic field that was described by Marques and Bowtell [84]. Biasfields are removed using preprocessing strategies that have shown promising results [78, 97, 98], but may prevent subsequent QSM algorithms from recovering from imperfections in background field estimation. These methods address the ill-posed nature of the inverse problem by employing regularization strategies [31] or obtaining multiple acquisitions, in which the subject is required to repeatedly rotate the head through different angles [79, 98]. An example of a QSM multi-angle acquisition result (QSM-MAA) is shown in Fig. 1-4c.

1.3 Problem Statement and Contributions

This dissertation focuses on two related problems: the correction of distortion in echo planar MRI and the quantification of magnetic susceptibility in the brain. EPI distortion is typically corrected using fieldmap-based methods. Although these techniques offer a post-processing correction strategy that is fast and easy to implement, fieldmaps require additional scan time, may not be reliable in the presence of significant motion or respiration effects, and are often omitted from clinical protocols. In this work, we develop a susceptibility-based distortion correction algorithm. An atlas-based classifier is constructed from CT data and used to obtain tissue/air susceptibility models from structural MRI. These are used as input to a forward model

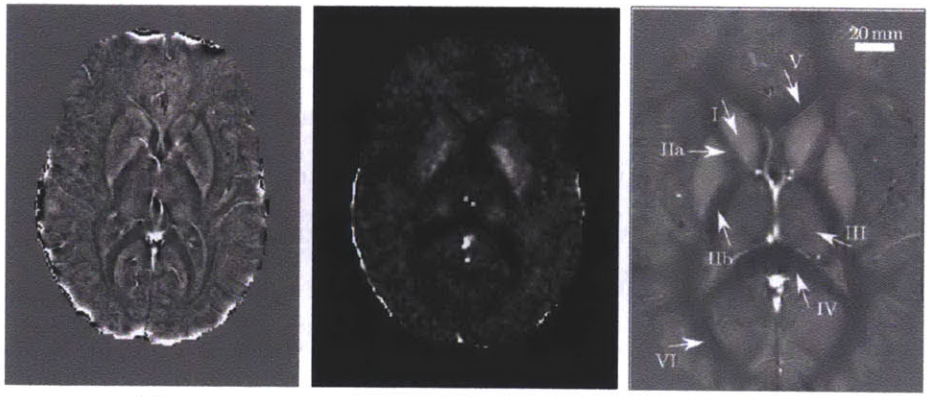

(a) (b) (c)

Figure 1-4: Susceptibility Imaging Methods. SWI and FDRI results from the same subject are shown in (a) and (b) respectively. The high-pass filtered phase image from SWI provides strong image contrast throughout the brain, while iron-rich regions adjacent to the ventricles are clearly visible in the FDRI. FDRI has been shown to correlate well with postmortem iron concentrations, but both methods provide measurements that are only indirectly related to susceptibility values [91]. Results from QSM-MAA for a different subject are shown in (c) with several regions of interest labeled in white (reprinted, with permission, from [98]). This approach provides both adequate image contrast and quantitative susceptibility estimates, but requires multiple acquisitions with the head positioned at different orientations in the scanner.

derived in image space from Maxwell's equations [59]; the output is an initial estimate of the perturbing field. A novel registration algorithm for estimating unknown shim parameters is used to compute a final synthetic fieldmap, which is then applied to unwarp the EPI data. We obtain results that agree well with acquired fieldmaps, providing a method suitable for retrospective registration and distortion correction of EPI data.

Postmortem studies and the development of imaging techniques such as SWI, FDRI, and QSM-MAA have provided increasing evidence of iron accumulation in specific brain regions in neurodegenerative disease and normal aging. While SWI allows excellent visualization of veins, microhemorraghes, and other structures exhibiting local susceptibility differences, it does not provide truly quantitative susceptibility estimates. In addition, mean SWI values in iron-rich regions of interest in the brain have been shown to correlate poorly with postmortem iron estimates [91]. In contrast, FDRI correlates well with postmortem iron concentrations in both young and

elderly subjects [91]. FDRI requires images to be collected on two separate scanners, however, making it impractical for most studies. QSM-MAA results have showed strong correlation between estimated susceptibility values and postmortem iron concentration in a subset of brain regions, but require multiple image acquisitions with the head positioned at various orientations in the scanner.

In this thesis we develop a novel atlas-based susceptibility mapping (ASM) technique that requires only a single acquisition and successfully inverts the forward model relating magnetic susceptibility to the observed field. By taking the Laplacian of the observed field, we eliminate low frequency biasfields, and obtain a wave equation relating the Laplacian of the field to the D'Alembertian of susceptibility. A tissue/air atlas is used to resolve ambiquity in the forward model arising from the ill-posed inversion. We include fourier-based modeling of external susceptibility sources and the associated biasfield in a variational approach, allowing for simultaneous susceptibility estimation and biasfield elimination. Quantitative susceptibility maps are computed by solving the optimization problem using standard conjugate gradient techniques. Mean susceptibility values in multiple brain regions including the thalamus (TH), caudate (CD), putamen (PT), and globus pallidus (GP) are computed and compared to those from other methods. Results show substantial improvement over those obtained with SWI and agree well with those obtained from FDRI and QSM-MAA. Furthermore, they show excellent correlation with postmortem iron measurements.

In conclusion, our primary contributions to the field of medical image analysis include:

- An atlas-based classifier for obtaining tissue/air/bone susceptibility models from T1-weighted structural MRI;
- A novel registration algorithm for estimating synthetic fieldmaps from tissue/air susceptibility models and correcting distortion in EPI data;
- Derivation of a wave equation relating the D'Alembertion of susceptibility to the Laplacian of the observed field, which eliminates low frequency biasfields due to external sources;

- A variational atlas-based susceptibility mapping (ASM) technique, which uses a tissue/air atlas to resolve ambiguity in a spatial formulation of the forward model and incorporates fourier-based modeling of external susceptibility sources, producing results that correlate strongly with postmortem iron measurements.

1.4 Thesis outline

The organization of this dissertation is as follows: Chapter 2 provides a concise review of the MR physics relating magnetic susceptibility to the magnetic field, the phase of the MR signal, and EPI distortion. Existing methods for correcting distortion and calculating synthetic fieldmaps are reviewed; the challenges and current approaches to solving the inverse problem are discussed. In Chapter 3 we describe our susceptibility-based distortion correction algorithm, which allows estimation of synthetic fieldmaps for unwarping and registration of EPI data to structural MR. We present results from correction of both FMRI and DTI data. In Chapter 4, we construct an atlas-based classifier for segmentation of tissue/air/bone susceptibility models from structural MRI and quantify the corresponding improvement in synthetic fieldmap estimates. In Chapter 5, we develop an atlas-based method for quantitative susceptibility mapping, that relates the Laplacian of the observed field to the D'Alembertion of susceptibility. We then revise the model to incorporate the strengths of fourier-based inversion for estimation of external susceptibility sources. Results are validated against postmortem iron concentrations and other methods commonly used to infer underlying susceptibility values. In Chapter 6, we summarize the contributions of this thesis, and discuss interesting future directions for this work, including the estimation of quantitative susceptibility time-series from perfusion studies.

Chapter 2

Background and Related Work

In this chapter we provide a concise description of the magnetic resonance imaging (MRI) experiment under ideal conditions, showing how applied magnetic fields interact with hydrogen nuclei to generate high resolution images that reveal detailed anatomical structure. We consider the effect of each external field in turn and review how a classical description of MRI physics can be used to explain three key facts of the MRI experiment. We then consider how magnetic susceptibility differences cause magnetic field perturbations, which lead to distortion in echo planar images (EPI). We discuss existing methods to correct these distortions, including the acquisition of magnetic field maps and the calculation of synthetic ones. Two of these synthetic field models are discussed in detail. Finally, we describe the inverse problem of computing susceptibility distributions from the measured field and review existing methods for quantitative susceptibility mapping (QSM). We begin by presenting a brief comparison of MRI to the widely known technology of computed tomography (CT).

2.1 MRI: Comparison to CT

CT became clinically available in the early 1970s and was the first imaging method made possible by modern computing [22]. As a tomographic imaging method, CT provides an image ('graph') of a slice ('tomo') of anatomy, excluding any structures

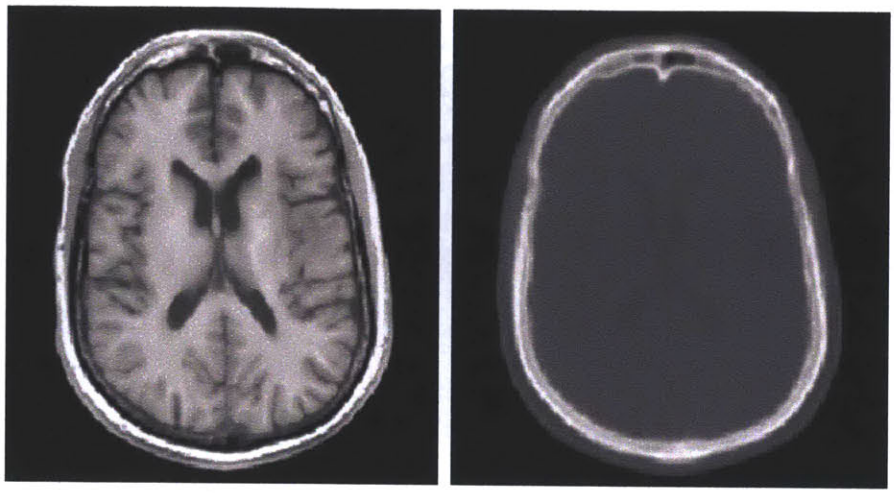

(a) (b)

Figure 2-1: CT and Structural MRI. Axial cross-sections of a T1-weighted structural image (a) and CT (b) of a patient at Brigham and Women's Hospital have substantially different intensity properties. The MRI shows excellent contrast within the soft tissue of the brain, while the CT shows strong contrast between bone and soft tissue.

above or below the slice of interest. CT advanced the practice of medicine by reducing the need for exploratory surgery. Modern CT scanners can easily acquire 5 mm thick slices along a 30cm length of the patient in 10 seconds, providing a rapid way of identifying a wide range of pathologies [22]. While CT is essentially a two dimensional technology, MRI is inherently three dimensional. One has the choice of collecting data and using three dimensional reconstruction techniques or aquiring data from a series of two dimensional slices [49]. In either case, images are viewed as a set of tomographic slices, but image acquisition occurs on a time-scale of minutes (often tens of minutes for a typical scan). In addition, MRI and CT differ in the form of energy used for image acquisition, the physical properties that produce image constrast, and the resolutions that are typically achieved in clinical settings.

The physical machinery of CT consists of rotating mechanical gantries that produce images based on the absorption of X-ray photons, while MRI consists of a stationary system that acquires images through the use of rapidly varying magnetic fields that interact with loosely bound hydrogen nuclei [49]. In contrast to CT, MRI uses only non-ionizing radiation that can be applied with great versatility. The 'input

signals' used in CT are X-ray pulses of uniform strength that vary in direction and the 'output signals' are attenuated X-rays, which result in spatially encoded information. In MRI, the input signals are magnetic fields that can vary in strength, duration, frequency, and direction, while the output signals are time-varying magnetic fields that contain temporally encoded information about the object [49].

In CT, a single spatially varying physical property, $\mu(x, y, z)$, the X-ray attenuation coefficient is being imaged. In MRI, three spatially varying physical properties, $M_0(x, y, z)$, $T_1(x, y, z)$, and $T_2(x, y, z)$, are being imaged. $M_0(x, y, z)$ is related to the distribution of mobile hydrogen nuclei (or those in the liquid state) and provides the 'shape' of the image, similar to $\mu(x, y, z)$. $T_1(x, y, z)$ and $T_2(x, y, z)$ are 'relaxation times' that are a function of local properties of the object and provide image contrast [49]. An example of a CT and MRI from a patient scanned at Brigham and Women's Hospital shows substantial differences in image contrast (Fig. 2-1). The highest spatial resolutions of CT and MRI that can usually be achieved in clinical settings are 0.4 mm and 1.0 mm respectively, although MRI resolution can improve at higher magnetic field strength [22]. The versatility of MRI, its relative safety due to non-ionizing radiation, excellent contrast and high resolution make it an invaluable tool for both clinical diagnosis and scientific investigation.

2.2 Basic Components of the MRI system

MRI systems have five basic components that control the imaging process, allowing the exchange of energy between magnetic fields and the sample's hydrogen nuclei to be precisely controlled. These are:

1. A *magnet*, which provides a strong (ie. 3 Tesla), uniform, static magnetic field, $\vec{B}_0$.

2. A *RF transmitter*, which delivers a time-varying radiofrequency (RF) magnetic field, $\vec{B}_1(t)$, to the sample.

3. A *gradient system*, which produces time-varying magnetic fields, $\vec{G}(t)$, of precisely controlled spatial variation across the sample that allow spatial encoding.

4. A *detection system* consisting of one or more receive coils that convert RF energy from the sample into a complex output signal, $S(t)$.

5. An *imaging system* that includes a computer for image reconstruction and display [49].

To understand how input signals (RF fields) interact with the intrinsic sample properties, $M_0(x, y, z)$, $T_1(x, y, z)$, $T_2(x, y, z)$, to produce an image, we will consider how each of the principal magnetic fields in the scanner interact with the hydrogen nucleus. We aim to describe three observations or facts of the MRI experiment:

1. The *rate of precession* (cycles per second) of a proton in a magnetic field is proportional to the *strength* of the field.

2. There is *no signal* emitted by a proton when it is at its equilibrium position in alignment with the magnetic field. There *is signal* when the proton has been forced out of alignment, making some angle relative to the magnetic field.

3. If the magnetic field can be made non-uniform in a *controlled manner*, then by Fact 1, protons at different points in space will precess at different frequencies [49].

We will start with a simple physical and mathematical model of the interaction between a proton and the $\vec{B}_0$ field, adding additional fields to the model until the sample geometry can be related directly to the complex data recorded in k-space. While reviewing this classical description of image acquisition, we will assume ideal, homogeneous fields are applied. We will then extend the model to describe how inhomogeneity in the $\vec{B}_0$ field and magnetic susceptibility differences in heterogenous samples affect the MRI signal and resulting images.

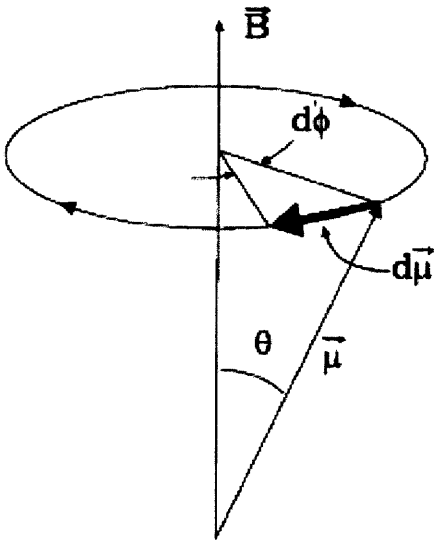

Figure 2-2: Precession of the Magnetic Moment. In the presence of a static external field, a proton with magnetic moment, $\vec{\mu}$, will precess about the direction of the main field, $\vec{B}_0$, accumulating phase $d\vec{\phi}$ during a differential time, dt (reprinted, with permission, from [45]).

2.3 Image Acquisition

2.3.1 The B_0 Field and a Physical Model of Precession

Protons have intrinsic angular momentum, or 'spin', that can be conceptualized as circulating charge that has an associated magnetic moment. The magnetic moment, $\vec{\mu}$, is related to the spin angular momentum vector, $\vec{J}$, by:

$$\vec{\mu} = \gamma \vec{J} \tag{2.1}$$

where γ is the gyromagnetic ratio, which depends on the particle of interest [45]. For protons,

$$\gamma = 2.675 \times 10^8 \text{ rad/s/T} \tag{2.2}$$

although the related quantity, 'gamma-bar', is often used instead:

$$\gamma = \frac{\gamma}{2\pi} = 42.58 \text{ MHz/T} \tag{2.3}$$

where 1 Tesla (T) = 10,000 Gauss (G). In a constant magnetic field, $\vec{B}_0$, the magnetic moment experiences a net torque:

$$\vec{\tau} = \vec{\mu} \times \vec{B}_0 \quad . \tag{2.4}$$

A non-zero torque implies the angular momentum must change according to:

$$\frac{d\vec{J}}{dt} = \vec{\tau} \quad . \tag{2.5}$$

By combining Eq. 2.1, Eq. 2.4 and Eq. 2.5, we obtain:

$$\frac{d\vec{\mu}}{dt} = \gamma\vec{\mu} \times \vec{B}_0 \quad , \tag{2.6}$$

which is the fundamental equation of motion describing precession of the magnetic moment in the external magnetic field as shown in Fig. 2-2 [45]. The geometry of Fig. 2-2 shows that the proton axis traverses an arc of length:

$$|d\vec{\mu}| = \mu \sin\theta \, |d\phi| \quad . \tag{2.7}$$

Combining this with $|d\vec{\mu}| = \gamma\mu B_0 \sin\theta \, dt$ gives $\gamma B_0 \, dt = |d\phi|$, which leads to the *Larmor* precession frequency:

$$\omega_0 = \frac{d\phi}{dt} = -\gamma B_0 \quad , \tag{2.8}$$

for $\vec{B}_0 = B_0\hat{z}$, which causes a clockwise precession about the z-axis. In coordinate form, Eq. 2.6 can be re-written as a set of coupled differential equations,

$$d\mu_x/dt = \gamma B_0 \mu_y \tag{2.9}$$

$$d\mu_y/dt = -\gamma B_0 \mu_x \tag{2.10}$$

$$d\mu_z/dt = 0 \quad , \tag{2.11}$$

where μ_x, μ_y, and μ_z represent the x, y, and z components of the magnetic moment, respectively. These equations have the solution,

$$\mu_x(t) = \mu_x^0 \cos\omega_0 t - \mu_y^0 \sin\omega_0 t \tag{2.12}$$

$$\mu_y(t) = \mu_x^0 \sin\omega_0 t + \mu_y^0 \cos\omega_0 t \tag{2.13}$$

$$\mu_z(t) = \mu_z^0 \quad . \tag{2.14}$$

Thus, Eq. 2.6 is an equation of motion that explains our first observation that a proton in a static magnetic field will precess at a rate that is proportional to the main field strength, which is referred to as the Larmor frequency [49]. The motion of the spin creates a time-varying magnetic field that induces a current in the nearby detector coil. In practice, bulk samples consist of a large number of protons. Assume the main field lies along the z-axis, $\vec{B}_0 = B_0\hat{z}$, and consider a collection of protons with axes at a fixed angle, θ, relative to $\vec{B}_0$, which are all precessing at frequency, ω_0, but with arbitrary position along the precession path. In this case, the sum of the transverse components of the magnetic moments, μ_x and μ_y, will cancel while the μ_z components will add, producing a net magnetization along the main field direction $\vec{M} = M_0\hat{z}$. In this equilibrium condition the net magnetization is static and no signal will be produced. If the system can be perturbed, however, such that the net magnetization makes some angle, θ, relative to the main field direction, then M will undergo precession according to:

$$\frac{d\vec{M}}{dt} = \gamma\vec{M} \times \vec{B}_0 \quad , \tag{2.15}$$

which allows a signal to be detected by the receive coil. Eq. 2.15 is a simplified version of the well-known Bloch equation and explains our second observation from section 2.2. This perturbation away from equilibrium is accomplished by application of an RF field [49].

2.3.2 The RF Field and Resonance

The RF transmitter produces a time-varying magnetic field given by:

$$\vec{B}_1(t) = 2B_1(t)\cos(\omega t)\,\hat{x} \quad , \tag{2.16}$$

where $B_1(t)$ is a modulation function that turns the RF field on and off [49]. This is a linearly polarized field since it oscillates in only one direction, but it can also be written as the sum of two circularly polarized fields of opposite polarization:

$$\vec{B}_1(t) = B_1(t)\left[\cos(\omega t)\,\hat{x} + \sin(\omega t)\,\hat{y}\right] + B_1(t)\left[\cos(\omega t)\,\hat{x} - \sin(\omega t)\,\hat{y}\right] \quad . \tag{2.17}$$

Since nuclei are known to be affected by only one of these fields, we can take the RF field to be:

$$\vec{B}_1(t) = B_1(t)\cos(\omega t)\,\hat{x} - B_1(t)\sin(\omega t)\,\hat{y} \quad . \tag{2.18}$$

To determine how the addition of the RF field affects the magnetization, one could substitute the total field,

$$\vec{B}(t) = B_0\hat{z} + \vec{B}_1(t) \quad , \tag{2.19}$$

into the Bloch equation (Eq. 2.15), but the awkwardness of the mathematics will obscure our intuition [49]. Instead, it is useful to analyze the effect of the RF field in a rotating reference frame. Consider a reference frame undergoing a negative (clockwise) rotation about the z-axis with frequency ω relative to the laboratory frame, which is equal to the frequency of the applied RF. It's angular velocity is given by:

$$\vec{\Omega} = -\omega\hat{z} \quad . \tag{2.20}$$

The unit vectors in the rotating frame, $\hat{x}'$, $\hat{y}'$, and $\hat{z}'$ are given by:

$$\hat{x}' = \cos(\omega t)\,\hat{x} - \sin(\omega t)\,\hat{y} \tag{2.21}$$

$$\hat{y}' = \sin(\omega t)\,\hat{x} + \cos(\omega t)\,\hat{y} \tag{2.22}$$

$$\hat{z}' = \hat{z} \quad . \tag{2.23}$$

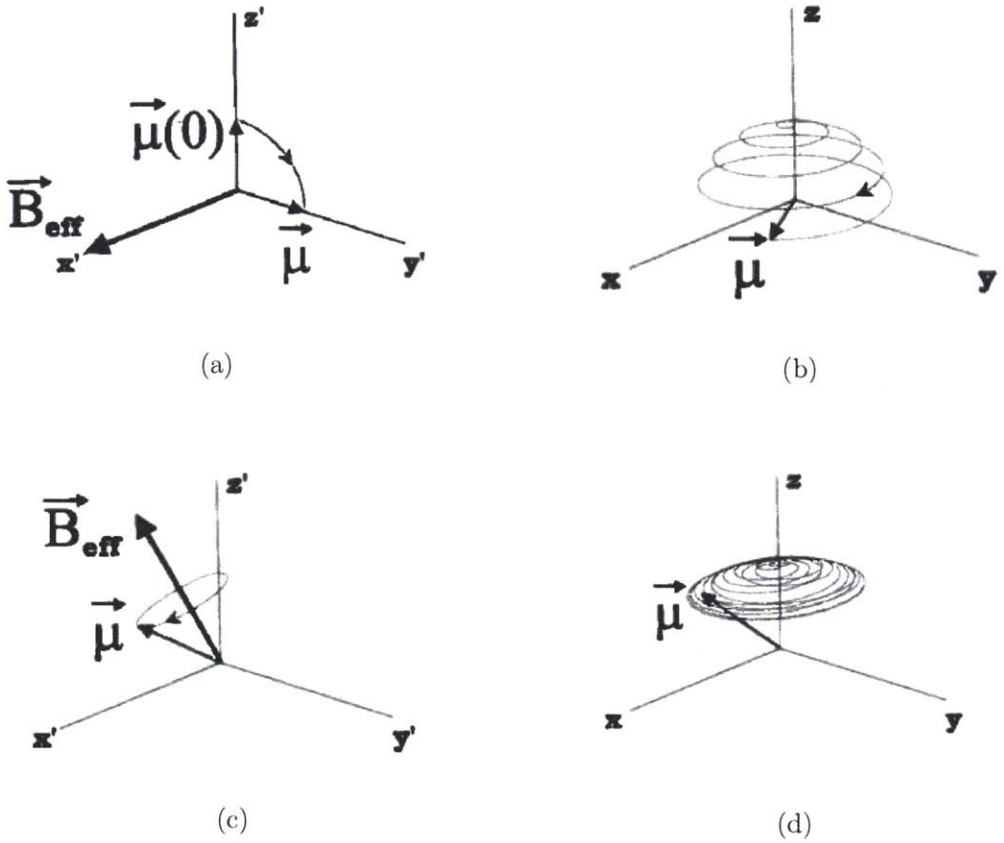

Figure 2-3: RF Excitation. The effect of an on-resonance RF pulse on a magnetic moment in the rotating frame is shown in (a) and its corresponding motion in the laboratory frame is shown in (b). The effect of an off-resonance RF field on the magnetic moment in the rotating frame is shown in (c) and its motion in the laboratory frame is shown in (d) (reprinted, with permission, from [45])

Given a proton precessing in the laboratory frame as shown in Fig. 2-3, it's motion in the rotating frame is described by:

$$\left(\frac{d\vec{\mu}}{dt}\right)' = \gamma\vec{\mu} \times \vec{B}_{eff} \quad , \tag{2.24}$$

where $\vec{B}_{eff}$ is the 'effective magnetic field' in the rotating frame, which is given by:

$$\vec{B}_{eff} = \vec{B} + \frac{\vec{\Omega}}{\gamma} \quad . \tag{2.25}$$

The effective magnetic field is the superposition of the total applied magnetic field, $\vec{B}$, and a fictitious magnetic field with a magnitude $|\vec{\Omega}|/\gamma$ and direction that is the same as the angular frequency vector, $\vec{\Omega}$, defining the rotating frame. Notice that if the rotating frame is rotating at the Larmor frequency, $\vec{\Omega} = -\gamma B_0 \hat{z}$, and the total applied field is $B_0\hat{z}$, then $(d\vec{\mu}/dt)' = 0$ and there is no motion of the magnetic moment in the rotating frame.

In the rotating frame, the RF field given in Eq. 2.18 simplfies to $\vec{B}_1 = B_1\hat{x}'$ after substitution of the expression for $\hat{x}'$. Combining Eqs. 2.19, 2.20, and 2.25, the motion of a magnetic moment vector in the rotating frame is:

$$\left(\frac{d\vec{\mu}}{dt}\right)' = \gamma\vec{\mu} \times \vec{B}_{eff} \tag{2.26}$$

$$= \vec{\mu} \times \left[\left(\gamma B_0 - \gamma\left(\omega/\gamma\right)\right)\hat{z}' + \gamma B_1 \hat{x}'\right] \quad . \tag{2.27}$$

When the frequency of the RF field in the laboratory frame matches the Larmor frequency, $\omega = \gamma B_0$, and the magnetic moment will precess about the $\hat{x}'$ direction according to:

$$\left(\frac{d\vec{\mu}}{dt}\right)' = \omega_1 \vec{\mu} \times \hat{x}' \quad , \tag{2.28}$$

where $\omega_1 = \gamma B_1$. For a RF pulse applied for a fixed time, τ, the magnetic moment (or net magnetization) will be rotated towards the transverse plane through an angle, θ, called the 'flip angle':

$$\theta = \gamma B_1 \tau \quad . \tag{2.29}$$

For a net magnetization, $M = M_0\hat{z}$, an RF pulse with a flip angle of 90° will rotate it fully into the transverse plane. Once the RF pulse is turned off, the magnetization will precess about the z-axis in the laboratory frame, generating a signal in the receive coil. If the magnetization remained in the transverse plane and did not return to its equilibrium position along the main field direction, the MRI signal would persist indefinitely, which is clearly not observed. Instead, the return to equilibrium occurs as a result of two physical relaxation processes, 'longitudinal' (or spin-lattice) relaxation and 'transverse' (or spin-spin) relaxation. These processes result from time-dependent

energy transfer between the nuclei and their surroundings due to local interactions and collisions [49]. Longitudinal relaxation determines the evolution of M_z towards its equilibrium value M_0 and is characterized by the time constant T_1. Transverse relaxation causes a loss of coherence or 'de-phasing' of the transverse magnetization, $M_x\hat{x} + M_y\hat{y}$, as individual spins become randomly oriented, resulting in a complete loss of transverse magnetization at equilibrium. This process is characterized by the time constant T_2. The result of T_1 and T_2 relaxation is a free-induction decay (FID) of the MRI signal. This behavior is characterized by the full Bloch equation:

$$\frac{d\vec{M}}{dt} = \gamma\vec{M} \times \vec{B} - (M_x\hat{x} + M_y\hat{y})/T_2 - (M_z - M_0)\hat{z}/T_1 \quad , \tag{2.30}$$

where $\vec{M}$ is the net magnetization, $\vec{B}$, is the applied field, T_1 and T_2 are the logitudinal and transverse relaxation times, and M_x, M_y, and M_z are the x, y, and z components of the magnetization respectively. M_0 is the equilibrium magnetization that exists if the sample is placed in a static B_0 field for a time that is long compared to T_1.

The Bloch equation provides a phenomenological model of the MRI experiment that describes the time dependent change in the net magnetization in the presence of an applied field. This model allows the MRI experiment to be described as a 'black box', where the input signal $\vec{B}(t)$ interacts with characteristic properties of the sample, M_0, T_1, and T_2, according to Eq. 2.30 to produce the output signal $\vec{M}(t)$. Including these local relaxation effects, the solution to Eq. 2.30 is given by:

$$M_x(t) = e^{-t/T_2}(M_x^0 \cos\omega_0 t - M_y^0 \sin\omega_0 t) \tag{2.31}$$

$$M_y(t) = e^{-t/T_2}(M_x^0 \sin\omega_0 t + M_y^0 \cos\omega_0 t) \tag{2.32}$$

$$M_z(t) = M_z^0\, e^{-t/T_1} + M_0(1 - e^{-t/T_1}) \quad , \tag{2.33}$$

where M_x^0, M_y^0, and M_z^0 are the x, y, and z components of M^0, the sample magnetization at $t = 0$. For mathematical convenience, the transverse magnetization is defined

in the complex plane as, $M = M_x + iM_y$, which gives the more compact solution:

$$M(t) = M^0 \exp(i\omega_0 t - t/T_2) \quad , \tag{2.34}$$

where $M^0 = M_x^0 + iM_y^0$. The receive coil sums the output signal across the entire sample, resulting in the MRI signal,

$$S(t) \propto \int M^0(\vec{x}) \exp(i\omega_0 t - t/T_2(\vec{x}))d\vec{x} \propto \int M^0(\vec{x}) \exp(i\phi(t) - t/T_2(\vec{x}))d\vec{x} \quad , \tag{2.35}$$

where $\phi(t) = \omega_0 t$. Additional details of the detection system are given in [49].

2.3.3 Gradients and Spatial Encoding

The previous two sections described how the B_0 and RF fields produce a time-varying signal, but MRI technology is compelling because of its ability to capture detailed spatial information about the object. Recall the third fact about MRI from section 2.2: the application of an inhomogeneous field causes protons at different locations to precess at different frequencies, which are proportional to the field at their position. Given the observed frequency and knowledge of the local field strength throughout the sample, the location of the spins can be recovered. In MRI, this 'spatial encoding' is achieved by application of three orthogonal gradient fields: the x-gradient, y-gradient, and z-gradient.

Application of a linear gradient produces a total field that increases linearly as a function of position. For example, assuming the main field is directed along the z-axis, a linear x-gradient, $G_x(t) = \partial B_z(t)/\partial x$, results in a total field directed along z that varies as a function of the x-coordinate:

$$\vec{B}(x, y, z, t) = B_0 \hat{z} + G_x(t) x \, \hat{z} \quad . \tag{2.36}$$

Since gradients may change with time, this time dependence is made explicit in Eq. 2.36. More importantly, Eq. 2.36 shows that our physical model of precession now becomes spatially dependent. Instead of a single net magnetization vector precessing

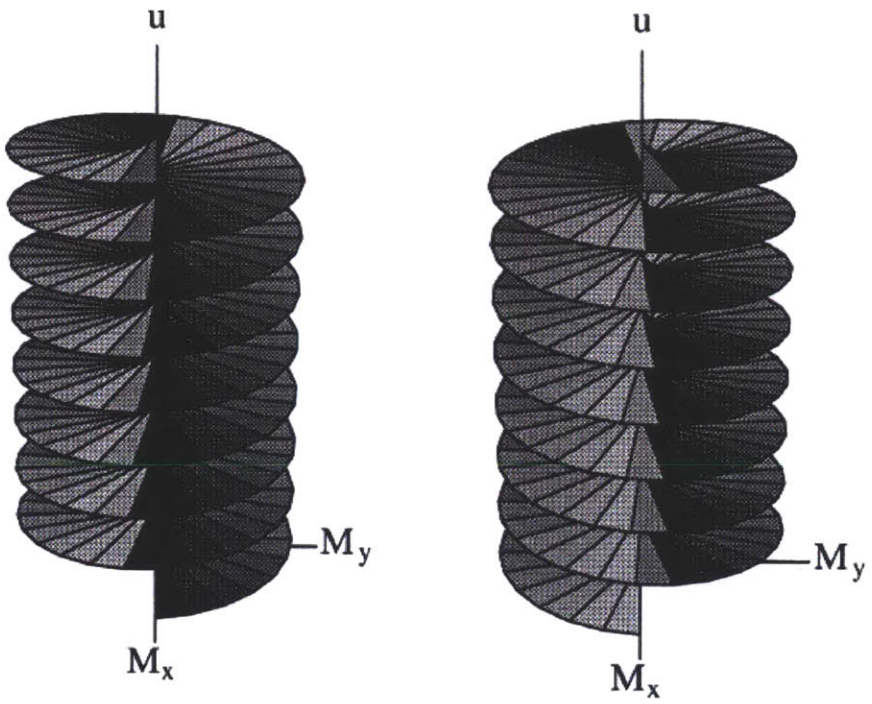

(a) (b)

Figure 2-4: Spatial Modulation of the Transverse Magnetization along gradient axis u. Application of a linear gradient along u modulates the phase of the transverse magnetization as a function of position along u resulting in a right-handed transverse magnetization helix, $e^{i(k_u u+\theta)}$, as shown in (a) or a left-handed helix, $e^{i(-k_u u+\theta)}$, as shown in (b). The phase offset, $\theta = 0$, in both (a) and (b) (reprinted, with permission, from [103]).

about the z-axis after RF excitation, the precession of each spin (or each collection of nuclei) about $\hat{z}$ at a given position along the x-axis is given by:

$$\omega(x, y, z, t) = -(\gamma B_0 + \gamma G_x(t)x) \quad . \tag{2.37}$$

For a gradient that is fixed in time, spins located along the x-axis are now distinguishable due to their difference in frequency; this is the essence of spatial encoding. Furthermore, a spin located at position (x, y, z) for some time τ after excitation, will accumulate phase specified by:

$$\phi(\tau) = \int_0^\tau \omega(t)\, dt = -\gamma \int_0^\tau B(x, y, z, t)\, dt \quad . \tag{2.38}$$

Therefore, the phase of a spin at a given time-point is also spatially dependent [114]. The strength of the gradient may be measured in Gauss/cm (CGS units) or mTesla/m (MKS) units, where 1 G/cm = 10 mT/m. State of the art gradient coils can produce gradient strengths up to 40 mT/m. For a 1.5 T magnet, a spin located at $x = 10$ cm would experience a total field of 1.504 T, which is only a small deviation from the main field strength. In general, application of all three gradients results in a frequency:

$$\omega = -\gamma(G_x(t)x + G_y(t)y + G_z(t)z) \tag{2.39}$$

$$= -\gamma \vec{G}(t) \cdot \vec{r} \quad , \tag{2.40}$$

where $\vec{G}(t) = (\partial B_z/\partial x,\ \partial B_z/\partial y,\ \partial B_z/\partial z)$ and $\vec{r}$ is the position vector [114]. The phase accumulated at time t is given by:

$$\phi(t) = \int \omega(t)\, dt = -\gamma \int B(x, y, z, t)\, dt \tag{2.41}$$

$$= -\gamma \int (G_x(t)x + G_y(t)y + G_z(t)z)\, dt \quad . \tag{2.42}$$

Eq. 2.42 can be expressed more concisely using 'k-space' formalism:

$$\phi(\tau) = -(k_x(t)x + k_y(t)y + k_z(t)z) \quad = \quad -\vec{k}(t) \cdot \vec{r} \quad , \tag{2.43}$$

where $k_x(t) = \gamma \int G_x(t)\, dt$, $k_y(t) = \gamma \int G_y(t)\, dt$ and $k_z(t) = \gamma \int G_z(t)\, dt$. In practice it is often useful to acquire data from a single two dimensional section or 'slice' of the object. This 'slice-selection' process is accomplished by turning on the z-gradient just before the RF pulse. This causes the spins along the z-axis to precess with frequency $\omega(z,t) = -(\gamma B_0 + \gamma G_z z)$. Note that at the isocenter ($z = 0$), $\omega = \omega_0$. If the RF pulse has frequency $\omega = -(\omega_0 + \omega')$, then the plane of spins excited by the RF pulse (and tipped towards the transverse plane) is given by:

$$z = \omega'/\gamma G_z \quad . \tag{2.44}$$

If the RF pulse contains a range of frequencies, $\Delta\omega$, then a slice of thickness, $\Delta z = \Delta\omega/\gamma G_z$, will be excited [114].

Consider turning on a linear gradient along x after the RF pulse and slice selection gradient tips a slice of spins into the transverse plane. The spins will precess at a frequency that is a linear function of their position, and the MRI signal can be sampled until the spins relax to equilibrium. A fourier transform of the signal will yield a spectrum of frequencies present, which identify the spins' positions. This process is called 'frequency encoding' and the x-gradient is termed the 'read-out' gradient.

Similarly, consider applying a linear field gradient with constant strength, $G_y = \partial B_z/\partial y$, along y for a short period of time, τ, after the RF pulse. While the gradient is on, the spins will precess in the transverse plane at frequencies that are a linear function of their location along y. Once the gradient is turned off, the spins will have accumulated phase values that are dependent on their precession frequencies, $\phi(y) = \tau\omega(y)$. In general, the phase is a function of a spin's position and the gradient history between excitation and measurement [114]. Application of this y-gradient causes the spins' transverse magnetization vectors to precess in the transverse plane, and can be

represented as helix along the y-axis. This helix, or magnetization grating, remains once the gradient is turned off since all of the spins will then precess at the Larmor frequency. The longitudinal component of the spin's magnetization vector remains unaffected by the applied gradient. Following the convention that the transverse magnetization lies in a complex plane, the helix is described by $e^{i(k_y y+\theta)}$, where θ represents any overall initial phase offset, and $k_y = \gamma \int_0^\tau G_y \, dt$. k_y can be interpreted as the spatial frequency of the helix, or in other words, the periodicity with which the transverse magnetization rotates through 2π (Fig. 2-4) [103]. While the gradient is left on, the value of k_y increases linearly in time, and the helix is wound more tightly.

In general, a helix $e^{i(k_u u+\theta)}$ can be created after application of a gradient along any direction, $\hat{u}$. If the object being imaged is a uniform sample, such as a water phantom, then the transverse magnetization vectors of the helix will cancel so that no net signal is generated. If the sample is a rack of water-filled test tubes or some other object with periodic structure that matches the spatial frequency of the helix, then a strong signal will be generated [114]. By controlling the timing of the y-gradient, the signal from a range of spatial frequencies can be recorded for the sample, which is referred to as 'phase-encoding'. A read-out gradient applied along x after the phase-encode gradient produces a helix of magnetization along the x-axis, allowing spatial frequencies along two orthogonal directions to be measured and recorded in k-space as a function of the coordinates (k_x, k_y). Applying a read-out or phase-encode gradient that decreases linearly as a function of position (ie. one with negative polarity) results in a helix that is wound in the opposite sense, corresponding to $k_x < 0$ or $k_y < 0$.

2.3.4 Gradient Echo and Echo Planar Pulse Sequences

Gradient echo and echo planar pulse sequences are two commonly used acquisitions that we will refer to often throughout this thesis. In a typical gradient echo experiment, negative phase encode and read-out gradients are applied following excitation and slice selection. After the phase-encode gradient is turned off, the direction of the read-out gradient is reversed, causing the negatively wound magnetization helix to slowly unwind and then re-wind in the positive sense. As the signal is sampled, a

single line of k-space is acquired. This experiment is repeated for every value of k_y by altering the initial strength of the phase-encode gradient until each line of k-space is sampled. Thus, a single line of k-space is acquired for each RF pulse. A key advantage to gradient echo imaging is that the RF pulse resets the transverse magnetization before the acquisition of each line of k-space. This reduces the effects of field inhomogeneities or other phase errors (that will be discussed in more detail in the next section). The disadvantage is that the sequence is slow; acquiring 64 lines of k-space for 30 slices to cover the entire head can take up to 20 seconds [114]. In contrast, in echo planar imaging, the polarity of the read-out gradient is reversed after each line of k-space is acquired, allowing the next line to be obtained after incrementing the phase-encode gradient. Repeatedly switching the direction of the read-out gradient while applying phase-encode 'blips' allows all of k-space to be traversed following a single RF pulse. This greatly increases the speed of the experiment: acquiring 64 lines of k-space for 30 slices can be done in less than 3 seconds [114]. EPI allows dynamic physiological processes, such as the blood-oxygenation level dependent (BOLD) response to be imaged [88], which forms the basis of fMRI. The primary disadvantage of EPI is its increased sensitivity to phase errors due to the use of a single RF pulse.

2.3.5 The Imaging Equation

Once the MRI signal is sampled and recorded in k-space for each spatial frequency, (k_x, k_y), using a gradient echo or EPI pulse sequence, all that remains is to reconstruct an image from this information. Recall that Eq. 2.43, represents the phase accumulation due to the affect of three orthogonal gradients. When imaging a single slice using the read-out and phase-encode gradients, this simplifies to: $\phi(t) = -(k_x(t)x + k_y(t)y)$. Since the magnetization at a given location, $M^0(x, y, z)$, is proportional to the density of spins at that location, and the corresponding phase created by the gradients is $\phi(t) = -(k_x(t)x + k_y(t)y)$, Eq. 2.35 can be rewritten as:

$$S(t) = \iint \rho(x, y) e^{-i(k_x(t)x + k_y(t)y)} e^{(-t/T_2(x,y))}\, dx\, dy \quad , \tag{2.45}$$

where the signal at time t, $S(t)$, is equivalent to the signal recorded in k-space at (k_x, k_y). Ignoring relaxation effects, Eq. 2.45 can be simplified:

$$S(k_x, k_y) = \iint \rho(x, y) e^{-i(k_x x + k_y y)} dx dy \quad . \tag{2.46}$$

We can also write Eq. 2.46 as:

$$S(k_x, k_y) = \iint \rho(x, y) e^{-i2\pi(k_x x + k_y y)} dx dy \quad , \tag{2.47}$$

where $k_x(t) = \gamma \int G_x(t)\, dt$, $k_y(t) = \gamma \int G_y(t)\, dt$ and $\gamma = \gamma/(2\pi)$. Eq. 2.47 is a 2D fourier integral over spatial coordinates (in units of m) with spatial frequency coordinates (in units of m^{-1}) as conjugate fourier variables. Therefore, by taking the inverse fourier transform of the k-space data we obtain the distribution of spin density in the object, which is the image of interest:

$$\rho(x, y) = F^{-1}\left[S(k_x, k_y)\right] = \iint S(k_x, k_y) e^{i2\pi(k_x x + k_y y)} dk_x dk_y \quad . \tag{2.48}$$

2.4 B_0 Field Inhomogeneity and EPI Distortion

EPI forms the basis of most fMRI and DTI studies and is widely used in both basic neuroscience and clinical research in areas such as pre-surgical planning and MR-guided intervention [25]. EPI-based fMRI and DTI acquisitions provide information that is distinct from conventional anatomical (or structural) imaging done in most clinical settings. A significant limitation of EPI, however, is its sensitivity to magnetic field inhomogeneity. Perturbations in the field result in signal loss and geometric distortion in EPI data [63, 53, 118, 18]. Previous studies have shown that correcting geometric distortion in functional images increases the accuracy of co-registration to structural MR [30, 53]. Precise anatomical localization of functional activation is especially important in single-subject studies (ie. pre-surgical evaluation) and in cases where the structural MR is used as an anatomical reference [53].

In the previous section, we showed how precisely controlled RF and gradient fields

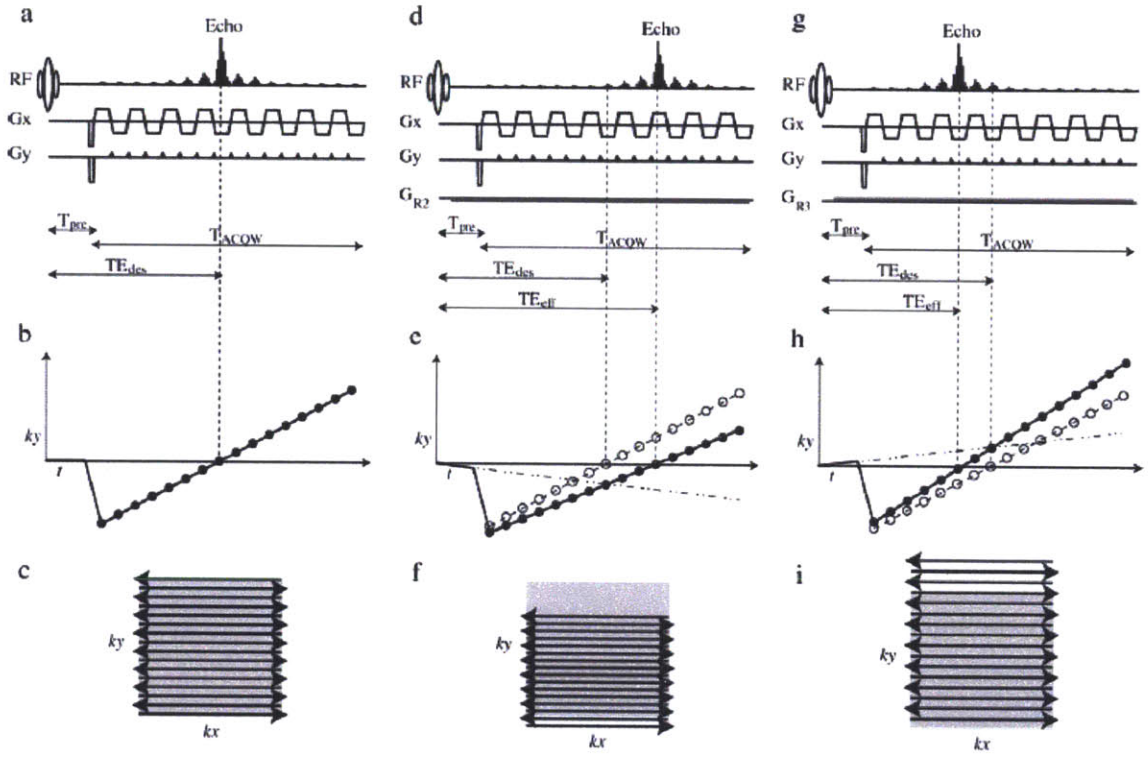

Figure 2-5: The Effect of Susceptibility Field Gradients on a Gradient Echo EPI k-space Trajectory . The RF excitation, signal, and gradient history for an EPI with no local susceptibility gradients is shown in (a). The corresponding values of $k_y(t)$ and the scan trajectory in 2-Dimensional k-space are shown in (b) and (c) respectively. The effects of susceptibility field gradients that are anti-parallel and parallel to the blipped phase encode gradient are shown in (d-f) and (g-i) respectively. The open circles in the plot of $k_y(t)$ plot show the desired evolution of $k_y(t)$ while the solid circles show its actual value due to the susceptibility effects. The result is a compression or expansion of k-space leading to subsequent distortion of the image after taking the inverse fourier transform (reprinted, with permission, from [25]).

can be applied in the presence of a uniform, static B_0 field to manipulate the net magnetization and generate the MRI signal. It was shown that image reconstruction from the MRI signal assumes the total field in the scanner is the superposition of known linear gradient fields and a uniform B_0 field. In practice, however, gradient linearity is compromised to achieve high gradient strength and fast switching [64] and the B_0 field exhibits inhomogeneities as high as several hundred parts per million (ppm) due to limitations on magnet design and manufacture [27]. In addition, heterogeneous biological samples exhibit magnetic susceptibility differences that produce local field gradients, causing perturbations in the applied field.

To improve magnetic field homogeneity, MR scanners have a shim system that consists of superconducting active shims, ferromagnetic passive shims, and room-temperature spherical harmonic shim coils. The superconducting active shims and ferromagnetic passive shims can reduce field inhomogenity to within a few ppm before subjects or samples are placed in the magnet [27]. The spherical harmonic shim coils consist of the three linear gradients and five second order shims that produce fields based on the spherical harmonic expansion [27, 71]:

$$B_z(x,y,z) = \sum_n r^n P_n^m(\cos\theta)[a_{m,n}\cos(m\varphi) + b_{m,n}\sin(m\varphi)] \quad , \tag{2.49}$$

where r, θ, and φ are spherical coordinates, $a_{m,n}$ and $b_{m,n}$ are coefficients and $P_n^m(\cos\theta)$ are associated Legendre orthogonal polynomials of the first kind, degree n and order m. Eq. 2.49 is a solution of the Laplace equation, $\nabla^2 B_z = 0$, where B_z is the z-component of the total magnetic field in the MRI scanner; it can also be written in Cartesian coordinates, which is shown explicitly up to the second degree and order:

$$\begin{aligned} B_z(x,y,z) = {} & a_{0,0} + a_{0,1}z + a_{1,1}x + b_{1,1}y + \\ & a_{0,2}(z^2 - \rho^2/2) + 3a_{1,2}xz + 3b_{1,2}yz + 3a_{2,2}(x^2 - y^2) + 6b_{2,2}xy + \ldots \end{aligned} \tag{2.50}$$

where $\rho^2 = x^2 + y^2$ [71]. The process of 'shimming' typically refers to using these coils to correct low order spatial perturbations of the field caused by subjects or samples

in the scanner. Imperfect shimming and higher order perturbations, however, result in residual subject-specific inhomogeneity.

These perturbing fields can be approximated as linear field gradients over local regions of the object. The addition of such a gradient will cause a change in precession frequency of the transverse magnetization, $\Delta\omega$. The MRI signal from Eq. 2.45 now becomes:

$$S(t) = \iint \rho(x,y) e^{-i(k_x(t)x + k_y(t)y + \Delta\omega(x,y)t)} e^{(-t/T_2^*(x,y))} dxdy \quad . \tag{2.51}$$

The relaxation time constant T_2 has been replaced by T_2^*, where

$$\frac{1}{T_2^*} = \frac{1}{T_2} + \frac{1}{T_2'} \quad . \tag{2.52}$$

T_2' represents the decay rate due to external field inhomogeneity [45]. Consider a region of interest, $R2$, in a heterogeneous sample with spatially varying magnetic susceptibility. In the presence of an external magnetic field, such as B_0, these susceptibility differences cause field perturbations that can often be approximated as a linear 'susceptibility field gradient', G_{R2}, which exists in the region of interest. Consider a susceptibility gradient that lies along the same axis as the phase-encode gradient, G_y. If G_{R2} has opposite polarity relative to G_y, then the value of k_y will increase more slowly over time and the k-space data will be compressed and shifted. In contrast, if G_{R2} has the same polarity relative to G_y, then the value of k_y will increase more rapidly over time, causing a corresponding expansion of k-space as shown in Fig. 2-5 [25]. Taking the inverse fourier transform causes subsequent expansion of the image in the first case and compression in the second.

The field perturbations and associated image distortions are greatest near boundaries between materials with large susceptibility differences. For biological samples, there is an important susceptibility difference between tissue and air. Soft tissue and bone have similiar susceptibilities of ($\chi_t \approx -9.1 \times 10^{-6}$) [62] and ($\chi_b \approx -11.4 \times 10^{-6}$) [50], which counteract the applied field, while air interacts only weakly with the field ($\chi_a \approx 0.4 \times 10^{-6}$) [62]. This is critical in human studies where air-tissue interfaces in

the sphenoid and ethmoid sinuses and auditory canals produce large perturbations in the field in the frontal and temporal lobes of the brain [27].

Distortions due to magnetic susceptibility differences are subject, pulse-sequence, and field strength dependent. The problem of signal loss in EPI has been addressed elsewhere [26] as well as the effects of B_0 inhomogenity on other functional imaging acquisitions such as spiral pulse sequences [64, 87] and will not be discussed here. Instead, we limit our focus to the correction of geometric distortion in EPI data.

2.5 Distortion Correction Strategies

For single-shot EPI acquisitions there are several existing techniques for correcting geometric distortion. The majority of these are fieldmap based methods [118, 63, 53]. Fieldmaps can be obtained from a variety of pulse sequences, but are typically computed from a double-echo gradient recalled echo (GRE) sequence. In this sequence, k-space data, $S(k_x, k_y)$, is collected at two different echo times. Taking the inverse fourier transform of both data sets according to Eq. 2.48 produces complex data in image space, typically in Cartesian form. This can then be easily converted into magnitude and phase images at both time points. In most applications, the phase information is discarded and only the magnitude image is retained for scientific analysis or clinical use. In section 2.3.3, however, we saw that phase data contains important information about the field: the phase is a function of the total field a spin experiences from excitation until sampling (Eq. 2.41). Taking the difference in phase images acquired at different echo times, causes phase contributions from applied gradients and RF inhomogeneity to cancel, leaving only the phase due to B_0 inhomogeneity (assuming negligible chemical shift artifacts). The field inhomogeneity, or 'fieldmap', is calculated according to:

$$\Delta B_0(x, y, z) = \frac{\Delta\phi(x, y, z)}{\gamma \Delta TE} \quad , \tag{2.53}$$

where $\Delta\phi$ is the phase difference, γ is the gyromagnetic ratio in rad/sec/T and ΔTE is the difference in echo times between the two GRE sequences [63]. Thus, a fieldmap provides a direct measure of the B_0 inhomogeneity at each point in the image. The fieldmap can subsequently be converted into a transformation to correct the distorted EPI. Due to the low bandwidth of EPI in the phase encode direction, the required transformation reduces to a set of one-dimensional translations along that direction, which can be computed for each pixel in the brain. For example, for a phase encode direction along y, the distortion is given by:

$$\Delta y(x,y,z) = \frac{\gamma \Delta B_0(x,y,z) N_y t_{dwell}}{2\pi} \quad , \tag{2.54}$$

where $\Delta y(x,y,z)$ is the pixel shift in the phase encode direction, N_y is the number of voxels in the y direction, and t_{dwell} is the dwell time of the EPI sequence.

Fieldmap techniques, however, have several limitations. First, they require additional scan time, which may be difficult to accomodate in clinical studies. Second, a single fieldmap may not be valid for unwarping each EPI volume if there are significant effects due to motion or respiration in the timeseries. Finally, fieldmaps are not available in many retrospective studies.

Other correction methods have been proposed including the acquisition of bipolar field gradient images [18], the use of a multi-reference scan for correction during reconstruction [116], and k-space energy spectrum analysis [25]. Correction techniques based on modified EPI acquisitions also increase scan time [18] while ones that require retention of the complex EPI data may not be practical [25].

More recently, magnetic field models have been developed to estimate the static field inhomogeneity from subject specific susceptibility models [62, 67]. Koch et al. have extended these models beyond estimating the field to applying them for distortion correction. Their method, however, relies on registering another subject's CT data to the subject of interest in order to generate the tissue/air susceptibility model, and therefore may not account well for differences in individual anatomy. It also requires detailed knowledge of the shim system to implement the unwarping. In

the next section we discuss the use of magnetic field models to calculate synthetic fieldmaps in more detail.

2.6 Synthetic Field Maps and the Forward Model

Methods that seek to estimate synthetic fieldmaps from magnetic susceptibility distributions have relied on iterative approaches [16, 17, 77, 29, 112], on a perturbation solution of Maxwell's equations in image space [62], or on Fourier-based methods [83, 96, 84]. In this section, we describe two of these approaches in more detail: the spatial formulation [62], which is used in the synthetic fieldmap estimation and atlas-based QSM technique developed later in this thesis, and the method in [84] which has formed the basis for work in QSM by other investigators. The spatial formulation from [62] is summarized below.

2.6.1 Spatial Formulation of the Forward Model

The derivation of the spatial formulation of the forward model begins with a macroscopic description of magnetic fields in diamagnetic and paramagnetic materials via Maxwell's equations of magnetostatics [54]:

$$\nabla \cdot B = 0 \tag{2.55}$$

$$\nabla \times H = J \tag{2.56}$$

The magnetic induction, B, is related to the magnetic field, H, by $B = \mu H$ where μ is the magnetic permeability. In Eq. 2.55 and Eq. 2.56, B is the fundamental field of interest, while H is the derived field that takes into account in an average way, the contribution of atomic charges and currents to the macroscopic current density, J [54]. Assuming $J = 0$ over some finite region of interest (the object is non-conductive), then $\nabla \times H = 0$, implying $H = \nabla\phi$, where ϕ is the magnetic scalar potential. The

magnetic field in the scanner can now be related to ϕ and μ according to:

$$B = \mu H = \mu \nabla \phi \quad . \tag{2.57}$$

The permeability is related to the magnetic susceptibility, χ, by:

$$\mu = \mu_0(1 + \chi) \quad , \tag{2.58}$$

where μ_0 is the permeability of free space. Eqs. 2.55, 2.57 and 2.58 can be combined to give:

$$\nabla \cdot B = \nabla \cdot \mu \nabla \phi = \nabla \cdot \mu_0(1 + \chi) \nabla \phi = 0 \quad . \tag{2.59}$$

Assuming μ_0 and χ are known, obtaining a solution for B, requires solving for the unknown magnetic scalar potential. Using a perturbation approach, we begin by expanding the susceptibility as:

$$\chi = \chi_0 + \delta \chi_1 \quad , \tag{2.60}$$

where χ_0 is the susceptibility of air (0.4 ppm) and δ is a constant equal to the difference between the susceptibility of air and the tissue of interest (ie. -9.5 ppm in the case of brain tissue). χ_1 is a 'scaled' version of the susceptibility difference and can take on continuous values when using a complex tissue model, but will take values of 0 or 1 for a simple two-tissue model [62]. Similarly, ϕ is expanded in a series:

$$\phi = \phi_0 + \delta \phi_1 + \delta^2 \phi_2 + \ldots \tag{2.61}$$

We also expand B:

$$B = B^{(0)} + \delta B^{(1)} + O(\delta^2) \quad . \tag{2.62}$$

Substituting expansions up to first order from Eqs 2.60, 2.61, and 2.62 into Eq. 2.59 gives:

$$\nabla \cdot (B^{(0)} + \delta B^{(1)}) = \nabla \cdot \mu_0(1 + \chi_0 + \delta \chi_1) \nabla(\phi_0 + \delta \phi_1) = 0 \quad . \tag{2.63}$$

The zeroth and first order terms in δ are:

$$\nabla \cdot B^{(0)} = \mu_0(1+\chi_0)\nabla^2\phi_0 = 0 \tag{2.64}$$

$$\nabla \cdot B^{(1)} = \mu_0(1+\chi_0)\nabla^2\phi_1 + \mu_0\nabla\cdot(\chi_1\nabla\phi_0) = 0 \tag{2.65}$$

Rearranging Eq. 2.65 gives a 3D Poisson equation:

$$\nabla^2\phi_1 = \frac{-1}{1+\chi_0}(\nabla\cdot(\chi_1\nabla\phi_0)) \quad . \tag{2.66}$$

The Green's function for this equation is:

$$G(\mathbf{x}) = \frac{-1}{4\pi r} \tag{2.67}$$

where $\mathbf{x} = (x, y, z)$ and $r = \| \mathbf{x} \| = \sqrt{x^2+y^2+z^2}$. The Poisson equation has the solution:

$$\phi_1(\mathbf{x}) = \iiint G(\mathbf{x}-\mathbf{x}\prime)f(\mathbf{x}\prime)d\mathbf{x}\prime \tag{2.68}$$

$$\phi_1(\mathbf{x}) = G * f \tag{2.69}$$

where $f = \frac{-1}{1+\chi_0}(\nabla\cdot(\chi_1\nabla\phi_0))$. In MRI, since we are interested in only the z-component of the magnetic induction, Eqs. 2.57 becomes:

$$B_z = \mu H_z = \mu\frac{\partial\phi}{\partial z} \tag{2.70}$$

Substituting expansions up to first order from Eqs 2.60 and 2.61 and the z-component of 2.62 into Eq. 2.70 gives:

$$B_z^{(0)} + \delta B_z^{(1)} = \mu_0(1+\chi_0+\delta\chi_1)\frac{\partial(\phi_0+\delta\phi_1)}{\partial z} \tag{2.71}$$

$$= \mu_0(1+\chi_0+\delta\chi_1)\left(\frac{\partial\phi_0}{\partial z} + \delta\frac{\partial\phi_1}{\partial z}\right) \quad . \tag{2.72}$$

The zeroth and first order terms in δ are:

$$B_z^{(0)} = \mu_0(1+\chi_0)\frac{\partial \phi_0}{\partial z} \tag{2.73}$$

$$B_z^{(1)} = \mu_0\left(\chi_1\frac{\partial \phi_0}{\partial z} + (1+\chi_0)\frac{\partial \phi_1}{\partial z}\right) \quad . \tag{2.74}$$

Eq. 2.74 can be rewritten using Eq. 2.73 to give:

$$B_z^{(1)} = \frac{\chi_1}{1+\chi_0}B_z^{(0)} + \mu_0(1+\chi_0)\frac{\partial \phi_1}{\partial z} \quad , \tag{2.75}$$

Since,

$$\frac{\partial \phi_1}{\partial z} = \frac{\partial}{\partial z}(G * f) = G * \frac{\partial f}{\partial z} = \frac{\partial G}{\partial z} * f \quad , \tag{2.76}$$

Eq. 2.75 can now be written as:

$$B_z^{(1)} = \frac{\chi_1}{1+\chi_0}B_z^{(0)} + \mu_0(1+\chi_0)\left(\frac{\partial G}{\partial z} * \frac{-1}{1+\chi_0}(\nabla\cdot(\chi_1\nabla\phi_0))\right) \quad . \tag{2.77}$$

Finally, inspection of Eq. 2.64 shows $\nabla\phi_0 = \frac{B^{(0)}}{\mu_0(1+\chi_0)}$, which can be combined with Eq. 2.77 to give:

$$B_z^{(1)} = \frac{\chi_1}{1+\chi_0}B_z^{(0)} - \frac{1}{1+\chi_0}\left(\left(\frac{\partial^2 G}{\partial x \partial z}\right) * \left(\chi_1 B_x^{(0)}\right) + \left(\frac{\partial^2 G}{\partial y \partial z}\right) * \left(\chi_1 B_y^{(0)}\right) + \left(\frac{\partial^2 G}{\partial z^2}\right) * \left(\chi_1 B_z^{(0)}\right)\right) \quad . \tag{2.78}$$

Lorentz Correction

The solution in Eq. 2.78 is valid for continuous media. Given the discrete nature of the ^1H nuclei in MRI, it is necessary to calculate the desired field from the continuous solution using the Lorentz Correction [99, 45]. The corrected field is given by $B_{LC} = B - \frac{2}{3}\mu_0 M$ where $M = \chi H$ is the magnetization of the material. Combining this equation with Eq. 2.57 and Eq. 2.58 gives $B_{LC} = \mu_0(1+\chi/3)\nabla\phi$. Comparing this to the uncorrected field, $B_{LC} = \mu_0(1+\chi)\nabla\phi$, shows that the Lorentz Corrected solution can be found by replacing χ with $\chi/3$ in equations involving only χ and ϕ terms [62]. This gives the zeroth and first order corrected fields:

$$B_{LC}^{(0)} = \mu_0\left(1+\frac{1}{3}\chi_0\right)\nabla\phi_0 \tag{2.79}$$

$$B_{LC}^{(1)} = \frac{1}{3}\mu_0\chi_1\nabla\phi_0 + \mu_0\left(1+\frac{1}{3}\chi_0\right)\nabla\phi_1 \tag{2.80}$$

which can be combined with Eq. 2.76 to give:

$$B_{LC,z}^{(1)} = \frac{\chi_1}{3+\chi_0}B_{LC,z}^{(0)} - \frac{1}{1+\chi_0}\left(\left(\frac{\partial^2 G}{\partial x \partial z}\right)*(\chi_1 B_{LC,x}^{(0)}) + \left(\frac{\partial^2 G}{\partial y \partial z}\right)*(\chi_1 B_{LC,y}^{(0)}) + \left(\frac{\partial^2 G}{\partial z^2}\right)*(\chi_1 B_{LC,z}^{(0)})\right) \quad . \tag{2.81}$$

Note that only the corrected fields will be used for the remainder of this thesis and the LC subscript will be omitted.

Fieldmap Calculation and the Single Voxel Solution

Eq. 2.81 allows the first-order field, $B_z^{(1)}$, to be calculated given the zeroth order field, $B^{(0)}$, and the susceptibility distribution χ_1. The zeroth order field represents the field present with no object in the scanner. For a constant field in the z direction, $B_x^{(0)} = B_y^{(0)} = 0$ and $B_z^{(0)} = B_0$, which allows Eq. 2.81 to be simplified. Assuming a main field along z, $B^{(0)} = B_0\hat{z}$, then a fieldmap, F, can be computed from the susceptibility distribution:

$$F = \delta B_z^{(1)} = \delta B_z^{(0)}\left[\frac{\chi_1}{3+\chi_0} - \frac{1}{1+\chi_0}\left(\left(\frac{\partial^2 G}{\partial z^2}\right)*\chi_1\right)\right] \quad . \tag{2.82}$$

This can be re-written as:

$$F = \left(\frac{\delta B_z^{(0)}}{3+\chi_0}\right)\chi_1 - \left(\frac{\delta B_z^{(0)}}{1+\chi_0}\right)\left(\frac{\partial^2 G}{\partial z^2}\right)*\chi_1 \tag{2.83}$$

$$= (c_1\delta_0 - c_2 k)*\chi_1 \quad , \tag{2.84}$$

where $c_1 = (\delta B_z^{(0)})/(3+\chi_0)$, $c_2 = (\delta B_z^{(0)})/(1+\chi_0)$, δ_0 is the Dirac delta function and $k = (\partial^2 G)/(\partial z^2)$. Finally, this can be written as the convolution of a kernel K,

defined in continuous space, with the scaled susceptibility map (or segmentation), χ_1:

$$F(x,y,z) = K(x,y,z) * \chi_1(x,y,z) \quad , \tag{2.85}$$

where $K = c_1\delta_0 - c_2 k$. Note that χ_1 is a unitless quantity while K has the units of magnetic field (Tesla). In practice, the object and corresponding susceptibility distribution are approximated by discrete voxels, allowing the convolution in Eq. 2.82 to be calculated analytically for a single voxel with $\chi_1 = 1$ [62]:

$$H(x,y,z) = \iiint_{voxel} \frac{\partial^2 G}{\partial z^2}(x,y,z)\, dx\, dy\, dz \quad = \quad \frac{1}{4\pi} \tan^{-1}\left(\frac{xy}{zr}\right) \quad . \tag{2.86}$$

Due to the linearity of Eq. 2.82, the single voxel solutions can be added together to give the final fieldmap:

$$F(x,y,z) = K_s(x,y,z) * \chi_1(x,y,z) \quad , \tag{2.87}$$

where $K_s(x,y,z) = c_1\delta_0(x,y,z) - c_2 H(x,y,z)$ is the kernel computed in image space.

2.6.2 K-space Formulation of the Forward Model

The k-space formulation of the forward model developed by Marques and Bowtell [84], provides another method for estimating the magnetic induction, **B**, due to a macroscopic susceptibility distribution. This model has formed the basis for work in fieldmap prediction and QSM by several other investigators. The relevant theory is summarized below from [67] to provide a foundation for further discussion in subsequent chapters of this dissertation.

Maxwell's equation, $\nabla \cdot \mathbf{B} = 0$ implies **B** is the curl of a vector field **A**, called the vector potential:

$$\mathbf{B} = \nabla \times \mathbf{A} \tag{2.88}$$

For macroscopic media, assuming $\mathbf{J} = 0$ (no current), $\nabla \times \mathbf{B} = \mu_0(\nabla \times \mathbf{M})$[54].Combining

this with Eq. 2.88 and using the Coulomb gauge gives:

$$\nabla^2 \mathbf{A} = -\mu_0 \nabla \times \mathbf{M} \quad , \tag{2.89}$$

where $\mathbf{M}$ is the magnetization of the material. This poisson equation has a general solution:

$$\mathbf{A}(\mathbf{x}) = \frac{\mu_0}{4\pi} \int_V \frac{\nabla' \times \mathbf{M}(\mathbf{x}')}{\mid \mathbf{x} - \mathbf{x}' \mid} d^3x' + \frac{\mu_0}{4\pi} \int_S \frac{\mathbf{M}(\mathbf{x}') \times \mathbf{n}'}{\mid \mathbf{x} - \mathbf{x}' \mid} da' \quad , \tag{2.90}$$

where $\mathbf{x}$ is the generalized position vector and $\mathbf{n}'$ represents a unit vector perpendicular to the surface S [67]. Since $\mathbf{B} = \nabla \times \mathbf{A}$, taking the curl of a multipole expansion of the vector potential in Eq. 2.90 gives an expansion of $\mathbf{B}$. Retaining only the first non-vanishing term in this expansion results in

$$\mathbf{B}(\mathbf{x}) \approx \mathbf{B}_d(\mathbf{x}) = \frac{\mu_0}{4\pi} \int_V \left(\frac{3\mathbf{n}'(\mathbf{M}(\mathbf{x}) \cdot \mathbf{n}') - \mathbf{M}(\mathbf{x}')}{\mid \mathbf{x} - \mathbf{x}' \mid^3} \right) d^3x' \quad , \tag{2.91}$$

which approximates $\mathbf{B}$ as the field produced from a general magnetic dipole distribution [54, 67]. The work of Marques and Bowtell begins with this assumption [84]. They show that taking the fourier transform of Eq. 2.91 and a Cauchy limit in the rotating reference frame results in the expression first reported by Deville [33]:

$$\tilde{B}_d(\mathbf{k}) = \frac{\mu_0}{3} \frac{3\cos^2\beta - 1}{2} (\tilde{\mathbf{M}}(\mathbf{k}) - 3\tilde{M}_z(\mathbf{k})\hat{\mathbf{z}}) \quad , \tag{2.92}$$

where k is the coordinate location in k-space, $\tilde{\mathbf{M}}(\mathbf{k})$ and $\tilde{M}_z(\mathbf{k})$ are the three dimensional Fourier transforms of $\mathbf{M}(\mathbf{x})$ and $M_z(\mathbf{x})$, $\hat{\mathbf{z}}$ is a unit vector in the z-direction, and β is the angle between the direction of the main magnetic field and $\mathbf{k}$. From the geometry, $\cos^2\beta = k_z^2/(k_x^2 + k_y^2 + k_z^2)$ and the tranverse magnetization in the rotating frame can be ignored since we are only interested in the z-component of the field. Since $M_z(\mathbf{x}) \approx \chi(\mathbf{x})\frac{B_0}{\mu_0}$ for $\chi \ll 1$, taking the fourier transform of $M_z(\mathbf{x})$ and

substituting it into Eq. 2.92, gives the final approximation for the field:

$$\tilde{B}_{d,z}(\mathbf{k}) = B_0\left(\frac{1}{3} - \frac{k_z^2}{k_x^2 + k_y^2 + k_z^2}\right)\tilde{\chi}(\mathbf{k}) \tag{2.93}$$

$$= \tilde{K}_f(\mathbf{k})\tilde{\chi}(\mathbf{k}) \quad , \tag{2.94}$$

where $\tilde{K}_f(\mathbf{k})$ is the fourier space derivation of the kernel for a normalized field of $B_0 = 1$. Taking the inverse fourier transform of Eq. 2.94 gives the predicted fieldmap in image space [84]:

$$B_{d,z}(x, y, z) = K_f(x, y, z) * \chi(x, y, z) \quad . \tag{2.95}$$

2.6.3 Comparison of the Forward Models

Since the derivations of both the spatial and k-space formulations of the forward model begin with Maxwell's equations of magnetostatics, but differ in their approach and approximations, we are interested in determining if they are in fact equivalent. To address this question, we begin with the spatial formulation of the forward model in continuous space (Eq. 2.85):

$$F = K * \chi_1 \tag{2.96}$$

$$F = \delta B_z^{(0)}\left[\frac{\delta_0}{3 + \chi_0} - \frac{1}{1 + \chi_0}\left(\frac{\partial^2 G}{\partial z^2}\right)\right] * \chi_1 \quad . \tag{2.97}$$

Taking the Fourier transform, $\mathcal{F}$, of Eq. 2.97 gives:

$$\tilde{F} = \delta B_z^{(0)}\left[\frac{\mathcal{F}\{\delta_0\}}{3 + \chi_0} - \frac{1}{1 + \chi_0}\mathcal{F}\left\{\left(\frac{\partial^2 G}{\partial z^2}\right)\right\}\right]\tilde{\chi}_1 \quad , \tag{2.98}$$

where $\tilde{\chi}_1$ is the Fourier transform of the scaled susceptibility map, χ_1. Given that $\mathcal{F}\{\delta_0\} = 1$ and $\mathcal{F}\{f'(z)\} = ik_z\mathcal{F}\{f(z)\}$, Eq. 2.98 becomes:

$$\tilde{F} = \delta B_z^{(0)}\left[\frac{1}{3 + \chi_0} - \frac{1}{1 + \chi_0} ik_z \mathcal{F}\left\{\left(\frac{\partial G}{\partial z}\right)\right\}\right]\tilde{\chi}_1 \quad , \tag{2.99}$$

where $k_z = \gamma \int G_z(t)\,dt$. Applying the derivative property of the Fourier transform a second time gives:

$$\tilde{F} = \delta B_z^{(0)}\left[\frac{1}{3+\chi_0} + \frac{1}{1+\chi_0}k_z^2\mathcal{F}\{G\}\right]\tilde{\chi}_1 \quad , \tag{2.100}$$

The Fourier transform of the Green's function can be written as $\mathcal{F}\{G\} = \mathcal{F}\{-1/(4\pi r)\} = \frac{-1}{4\pi}\mathcal{F}\{\frac{1}{r}\}$ where $r = \sqrt{x^2+y^2+z^2}$. Since $\mathcal{F}\{\frac{1}{r}\} = \frac{4\pi}{k^2}$ (a derivation of this is given in Appendix A), Eq. 2.100 becomes:

$$\tilde{F} = \delta B_z^{(0)}\left[\frac{1}{3+\chi_0} - \frac{1}{1+\chi_0}\left(\frac{k_z^2}{k_x^2+k_y^2+k_z^2}\right)\right]\tilde{\chi}_1 \quad . \tag{2.101}$$

Recall from Eq. 2.60 that the scaled susceptibility, χ_1, is related to the the susceptibility, χ, according to $\chi_1 = (\chi - \chi_0)/\delta$. Taking the Fourier transform of this equation gives:

$$\mathcal{F}\{\chi_1\} = \frac{1}{\delta}(\mathcal{F}\{\chi\} - \mathcal{F}\{\chi_0\}) \tag{2.102}$$

$$= \frac{1}{\delta}(\tilde{\chi} - \chi_0\delta_0) \quad . \tag{2.103}$$

Substituting Eq. 2.103 into Eq. 2.101 gives:

$$\tilde{F} = B_z^{(0)}\left[\frac{1}{3+\chi_0} - \frac{1}{1+\chi_0}\left(\frac{k_z^2}{k_x^2+k_y^2+k_z^2}\right)\right](\tilde{\chi} - \chi_0\delta_0) \quad . \tag{2.104}$$

Since $\chi_0 << 1$, we can neglect the χ_0 terms in the denominators in Eq. 2.104 and re-write it as:

$$\tilde{F} \approx B_z^{(0)}\left[\frac{1}{3} - \left(\frac{k_z^2}{k_x^2+k_y^2+k_z^2}\right)\right]\tilde{\chi} - B_z^{(0)}\left[\frac{1}{3} - \left(\frac{k_z^2}{k_x^2+k_y^2+k_z^2}\right)\right](\chi_0\delta_0) \quad . \tag{2.105}$$

Eq. 2.105 can be written more concisely as:

$$\tilde{F} = \tilde{K}_f\tilde{\chi} - \tilde{K}_f(\chi_0\delta_0) \quad , \tag{2.106}$$

where $\tilde{K}_f$ is the kernel from the k-space formulation of the forward model (Eq. 2.94). The second term in Eq. 2.106 is zero everywhere except at the origin, $(k_x, k_y, k_z) = (0, 0, 0)$, where it is undefined since the value of $\tilde{K}_f(0, 0, 0)$ is undefined. The value at the origin of k-space corresponds to the 'DC offset' of phase in image space. Therefore, taking an inverse Fourier transform of Eq. 2.106 gives the fieldmap in image space:

$$F(x, y, z) = K_f(x, y, z) * \chi(x, y, z) + C \quad , \tag{2.107}$$

where C is the unknown DC offset. By comparing Eq. 2.107 to Eq. 2.95, we see that the spatial formulation of the forward model in continuous space is equivalent to the k-space formulation of the forward model within a constant that represents the unknown DC value of the acquisition. If we choose $C = 0$, we see that the two models are in fact effectively equivalent.

It is important to note that the spatial formulation of the forward model approximates the object as a collection of discrete voxels, which allows the convolution in Eq. 2.82 to be calculated analytically for a single voxel as described in Eq. 2.86 and Eq. 2.87. This aspect of the implementation requires further investigation to determine if the equivalency of the two models still holds after introduction of the single voxel approximation.

2.7 Solving the Inverse Problem: Quantitative Susceptibility Mapping

There is increasing evidence that excessive iron deposition in specific regions of the brain is associated with neurodegenerative disorders such as Alzheimer's and Parkinson's disease [125]. The role of iron in the pathogenesis of these diseases remains unknown and is difficult to determine without a non-invasive method to quantify its concentration in-vivo. Since iron is a ferromagnetic substance, changes in iron concentration result in local changes in the magnetic susceptibility of tissue.

In MRI experiments, differences in susceptibility cause perturbations in the local

magnetic field, which can in principle be computed from the phase of the MR signal, as described in Section 2.5. The forward models presented in Section 2.6 show how these field perturbations can also be computed if the spatial susceptibility distribution, χ, is known. The advent of high field MRI has made it possible for subtle differences in susceptibility to measurably affect the phase of the MR signal. This has raised the possibility that estimating unknown magnetic susceptibility distributions from high field phase data may provide a new means for quantifying iron concentration in-vivo.

Solving the inverse problem of estimating susceptibility from phase or field measurements is challenging for several reasons. In the forward models described in Section 2.6, field pertubations caused by magnetic susceptibility differences can be modeled as the convolution of the dipole-like kernels, K_s or K_f, with the spatial susceptibility distribution. In the Fourier domain, these kernels exhibits zeros at the magic angle, preventing direct inversion of the fieldmap [79]. Critically, observations of the field are limited due to the presence of air (where there is no signal) and the problem is ill-posed. The observed data is also corrupted by confounding biasfields (ie. those from tissue-air interfaces, mis-set shims, and other non-local sources). Eliminating these fields is critical for accurate susceptibility estimation since they corrupt phase contributions from the local susceptibility sources of interest.

Existing methods for inferring susceptibility values from MR phase data are generally thought of as susceptibility-related methods or QSM techniques. Haacke et al., have shown that a high-pass filter can be used to remove the predominantly low frequency biasfield and produce a filtered phase image in a post-processing method referred to as susceptibility weighted imaging (SWI)[47]. While SWI has shown some correlation with magnetic susceptibility differences due to iron and other sources, it produces only an indirect measure of susceptibility due to the non-local effects of the convolution kernel. In addition, the filtering process may remove some low frequency fields due to sources inside the brain, reducing the accuracy of the resulting SWI data, which is used as a proxy for susceptibility.

In [4], a method termed the field dependent transverse relaxation rate increase (FDRI) was proposed in which maps of the transverse relaxation time, $R_2 = 1/T_2$,

are acquired at two different field strengths (ie. 1.5 and 3 Tesla). The difference in R_2 divided by the difference in field strength gives the FDRI. In [91], the mean FDRI in several regions of interest was compared to the mean iron concentration obtained from postmortem analysis and showed stronger correlation with iron content than the SWI maps computed for the same subjects. Obtaining FDRI measurements would be impractical for most studies, however, since it requires images to be collected on two separate scanners.

Others have proposed methods to estimate magnetic susceptibility from fieldmaps. A method for quantitative susceptibility mapping described by de Rochefort et al. [31] has shown good results, but relies on sequential biasfield filtering and susceptibility estimation and therefore may not be able to recover from imperfections in biasfield removal. The technique presented by Liu et al. [79] showed some success, but requires data to be acquired at multiple object orientations, which is impractical for human studies. Recently, Schweser et al. published a technique for QSM [98] that showed good correlation between relative susceptibility values from averaged single angle acquisitions and those obtained from multi-angle protocols. Results showed strong correlation between estimated susceptibility values and postmortem iron concentration in a subset of brain regions, but relied on estimates computed from multi-angle data.

In general, QSM methods that rely heavily on agreement between observed and predicted field values computed using kernel-based forward models [31, 79, 98] are inherently limited since they cannot distinguish between low frequency biasfields from external susceptibility sources and identical fields produced by certain local susceptibility distributions. Susceptibility distributions that are eigenfunctions of K in Eq. 2.85 are one example of this; they include constant and linear functions of susceptibility along the main field (ie. 'z') direction. Applying the forward model to these distributions, cancels the second term in Eq. 2.84 resulting in predicted fields that are proportional to the local susceptibility sources, but also identical in form to non-local biasfields (ie. those produced by a z-shim). Therefore, removing all low frequency fields prior to susceptibility estimation will eliminate the biasfield as well

as fields due to the sources of interest, potentially preventing accurate calculation of the underlying susceptibility values. In contrast, inadequate removal of the biasfield may result in the estimation of artifactual susceptibility eigenfunctions in areas where the biasfield is strong, such as regions adjacent to tissue-air interfaces. This suggests that additional information such as boundary conditions or priors may be necessary to regularize an incomplete forward model and prevent the mis-estimation of low frequency biasfields.

Chapter 3

Synthetic Fieldmap Calculation for Distortion Correction of Echo Planar Images

Echo planar imaging (EPI) is the standard pulse sequence employed in functional magnetic resonance imaging (fMRI) and diffusion tensor imaging (DTI) studies due to its high temporal resolution. In order to extract meaningful information from EPI data, scientists and clinicians typically register low resolution EPI data to high resolution anatomical images. As discussed in detail in Chapter 2, a critical problem in achieving accurate registration is the inherent distortion of EPI data due to B_0 field inhomogeneity.

Fieldmap-based uwarping remains the standard method for correcting geometric distortion in EPI data [63, 30, 53]. Fieldmap techniques, however, require additional scan time, suffer from low signal-to-noise ratios (SNR) at tissue/air boundaries, and may be invalid for unwarping EPI data if there are significant effects due to motion or respiration. Also, fieldmaps are not available for most retrospective studies.

Recently, magnetic field models such as those described in section 2.6 have been developed to estimate synthetic fieldmaps from susceptibility distributions of the object of interest. Using these models for distortion correction is difficult for two reasons. First, subject-specific susceptibility maps are difficult to obtain in practice. For bio-

logical samples, susceptibility maps are obtained from tissue/air/bone segmentations since substantial susceptibility differences occurs between these materials: soft tissue and bone are diamagnetic ($\chi_{tissue} = -9.1$ ppm and $\chi_{bone} = -11.4$ ppm), while air is paramagnetic ($\chi_{air} = 0.4$ ppm) [62, 50]. Once a segmentation is obtained, accurate field estimates can be computed from 2 class susceptibility maps by setting: $\chi_{bone} \approx \chi_{tissue} = -9.1$ ppm [62, 67]. Tissue/air/bone segmentations are easily obtained from CT, given the large intensity differences between these materials, but CT is often not available in neuroscientific and clinical studies due to limits on radiation exposure. T1-weighted MRI is generally available, but bone and air are difficult to segment accurately due to their similar intensities in structural images.

The second problem with applying existing forward models for distortion correction is that these models do not account for the shim fields present during acquisition, which decrease B_0 inhomogeneity. The total field, including shim, must be estimated to accurately unwarp EPI data. Koch et al. investigated correcting distortion using synthetic fieldmaps, but their method relies on registering another subject's CT to the subject of interest to generate the susceptibility map, which may not account well for anatomical differences. It also requires detailed knowledge of the shim system to implement the unwarping [67].

In this chapter, we describe a Fieldmap-Free (FF) method to correct geometric distortion in EPI, without obtaining fieldmaps, modifying EPI acquisition parameters, requiring CT data for the subject of interest or having detailed knowledge of the shim system. We use acquired fieldmaps and CT data from neurosurgical patients for validation only, making this method suitable for retrospective clinical and neuroscientific studies in which fieldmaps and CT are not available. Our approach consists of two parts. First, a classifier is used to segment structural MRI into a tissue/air susceptibility model. This is used as input to the spatial formulation of the forward model described in section 2.6.1 to compute a subject-specific fieldmap. Second, a registration algorithm is developed to solve for the lower order field perturbations (shim parameters) needed to accurately unwarp and register the EPI data.

3.1 Methods

3.1.1 Data Acqusition

Structural MRI, EPI and dual gradient echo fieldmaps were acquired for six subjects. Neurosurgery patients were selected so that CT data would be available for validation and training. All MRI imaging was done in the Radiology department at Brigham and Women's Hospital on a 3T GE magnet. The MRI acquisition protocol included (1) whole-brain axial 3D-SPGR, slice thickness = 1 mm, TE = 3 msec, TR = 8 msec, acquisition matrix = 512 x 512, voxel size = 0.5 x 0.5 x 1 mm (2) single-shot EPI, slice thickness = 4 mm, TE = 40 msec, TR = 2000 msec, acquisition matrix = 128 x 128, voxel size = 2 x 2 x 4 mm (3) dual gradient echo fieldmap, slice thickness = 4 mm, TE_1 = 5 msec, TE_2 = 15 msec, TR = 600 msec, acquisition matrix = 256 x 256, voxel size = 1 x 1 x 4 mm. CT data sets for subjects 1 and 2 were acquired with 0.46 x 0.46 x 4.8 mm voxels spanning 36 slices and 512 x 512 in-plane voxels. CT from subject 1 was used for training, while CT from subject 2 was used for validation.

3.1.2 Validation using Acquired Fieldmaps

Synthetic fieldmaps computed using the Fieldmap-Free method will be validated against acquired fieldmaps and FF distortion correction and registration results will be compared to those obtained using the measured fieldmaps. Each acquired fieldmap was reconstructed from a dual gradient echo sequence. First, phasemaps were computed from the real and imaginary data obtained from each echo:

$$\phi(x,,y,z) = \arctan\left(\frac{\mathrm{Im}(x,y,z)}{\mathrm{Re}(x,y,z)}\right) \quad , \tag{3.1}$$

where $\phi(x,y,z)$ is the phasemap with values wrapped between 0 and 2π, $\mathrm{Im}(x,y,z)$ is the imaginary component of the complex data, and $\mathrm{Re}(x,y,z)$ is the real component. Second, FSL (FMRIB's Software Library) tools PRELUDE [58] and FUGUE [59]

were applied to unwrap the phase and compute the fieldmap according to:

$$\Delta B_0 = \frac{\Delta\phi(x,y,z)}{2\pi\gamma\Delta TE} \quad , \tag{3.2}$$

where $\Delta B_0(x,y,z)$ is the B_0 field inhomogeneity, $\Delta\phi(x,y,z)$ is the difference between unwrapped gradient echo phase maps acquired at two separate echo times (TE), ΔTE is the difference in echo times, and γ is the gyromagnetic ratio. FUGUE was also used to compute the distortion:

$$\Delta y = \frac{\gamma\Delta B_0(x,y,z)N_y t_{dwell}}{2\pi} \quad , \tag{3.3}$$

where Δy is the pixel shift in the phase encode direction, N_y is the number of voxels in the y direction, and t_{dwell} is the dwell time of the EPI sequence. Pre-processing of the EPI data was carried out using FSL FEAT [101]: spatial smoothing using a Gaussian kernel of FWHM 5 mm, mean-based intensity normalisation, and highpass temporal filtering was applied. Brain extraction of the structural MR was done using FSL BET [100]. The pixel shift map was applied to correct the distortion, and registration of the unwarped EPI to the high resolution structural MR was carried out using a seven degree of freedom (DOF) (rigid-body + scaling) transformation via the FLIRT registration algorithm [61]. Correlation ratio was used as the cost function [61, 60]. The signal loss was calculated and used for cost function weighting (to prevent FLIRT from trying to achieve agreement in regions of signal dropout) according to:

$$SL = \int \frac{exp(i\gamma\Delta B_0(x,y,z)TE)}{L} dz \quad , \tag{3.4}$$

where z is the through slice direction, L is the slice thickness, and TE is the echo time. Registration without unwarping was also carried out using FEAT and FLIRT. Both seven DOF rigid-body/scaling and twelve DOF affine transformations were applied.

3.1.3 Segmentation of Tissue/Air Susceptibility Maps

In the first part of the FF distortion correction method structural MRI is segmented into a tissue/air susceptibility model using a MR intensity classifier. To construct the classifier, CT data was registered to the fieldmap magnitude image for each subject using FLIRT so the estimated fieldmaps would be in the same space as the acquired fieldmaps for validation. The CT data was also resampled to 1x1x1 mm voxels and ROIs surrounding the head were extracted to improve the speed of subsequent fieldmap estimation. The CT from both subjects was thresholded to obtain an accurate tissue/air segmentation of the entire field of view (FOV). The tissue/air labels and structural MR intensity values from subject 1 were used to train a classifier that calculates the probability of tissue given MR intensity according to:

$$P(T \mid I_i) = \frac{P(I_i \mid T)P(T)}{P(I_i \mid T)P(T) + P(I_i \mid T^c)P(T^c)} \quad . \tag{3.5}$$

$P(I_i) = P(I_i \mid T)P(T) + P(I_i \mid T^c)P(T^c)$ denotes the probability a voxel is in the i^{th} MR intensity bin, while $P(T)$ and $P(T^c)$ are the prior probabilities of tissue and air, respectively. The conditional and prior probabilities were obtained from normalized intensity histograms. The classifier was then applied to segment the structural MR of five additional test subjects. If available, CT data for the test subject was used for validation of the MR-based segmentation results.

3.1.4 Initial Calculation of Synthetic Fieldmaps

Initial fieldmap calculations were performed using the spatial formulation of the forward model [62] described in Chapter 2, which is briefly reviewed here. In this model, a first order perturbation solution of Maxwell's equations is estimated from a tissue/air susceptibility model, where each voxel has an associated χ_1 variable that takes continuous values between 0 (air) and 1 (tissue) corresponding to susceptibility values of $\chi = \chi_0 - \delta\chi_1$, where χ_0 is the susceptibility of air (0.4 ppm) and δ is the difference in susceptibility between tissue and air (−9.5 ppm). Here, χ_1 is set equal to the tissue probability map, $P(T \mid I_i)$ computed in Eq. 3.5.

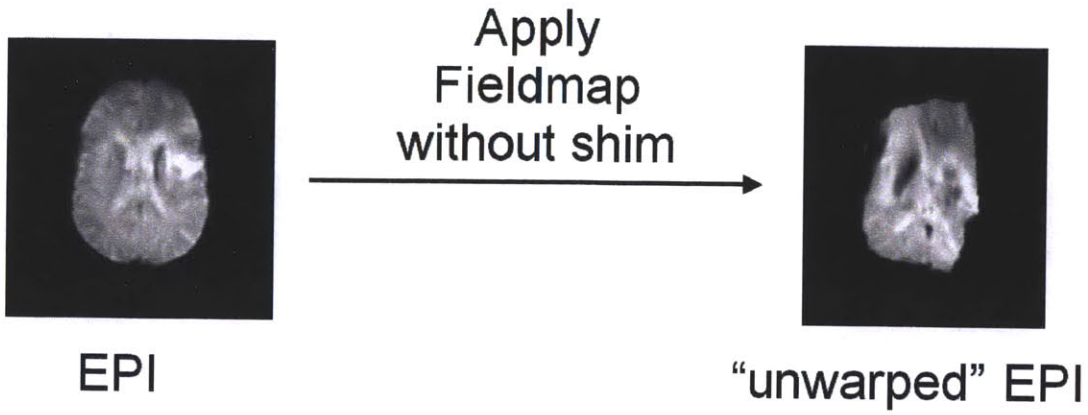

(a)

Figure 3-1: Unwarping using an Estimated Fieldmap Without Shim. Applying the initial estimate of the fieldmap from the forward field model without an estimate of the shims and other fields from anatomy outside the field of view results in a severely distorted image.

The field calculations are implemented as a linear convolution, which is fast and requires knowledge of only the voxel-based susceptibility model and MR field strength. The segmentation obtained from structural MR was used as input to the forward model to obtain an estimated synthetic fieldmap. If CT was available, a susceptibility map was obtained from the CT, the associated synthetic fieldmap was computed using the forward model, and the result was used for validation of the MR-based synthetic fieldmap.

3.1.5 Registration-based Shim Estimation

Current field modeling techniques, including the one described in [62], do not account for the shim fields that reduce B_0 inhomogeneity prior to fieldmap acquisition. Therefore, in order to compare an estimated fieldmap to an acquired one, the shim fields must be factored out of the acquired fieldmap (or added to the estimated one). Recall from Section 2.4 that MR systems typically have a set of room temperature shim coils consisting of the three linear gradients and five second order shims, which produce fields based on the spherical harmonic series [27]. Each shim field consists of a baseline value plus subject-specific offset, both of which, in principle, are known. The baseline

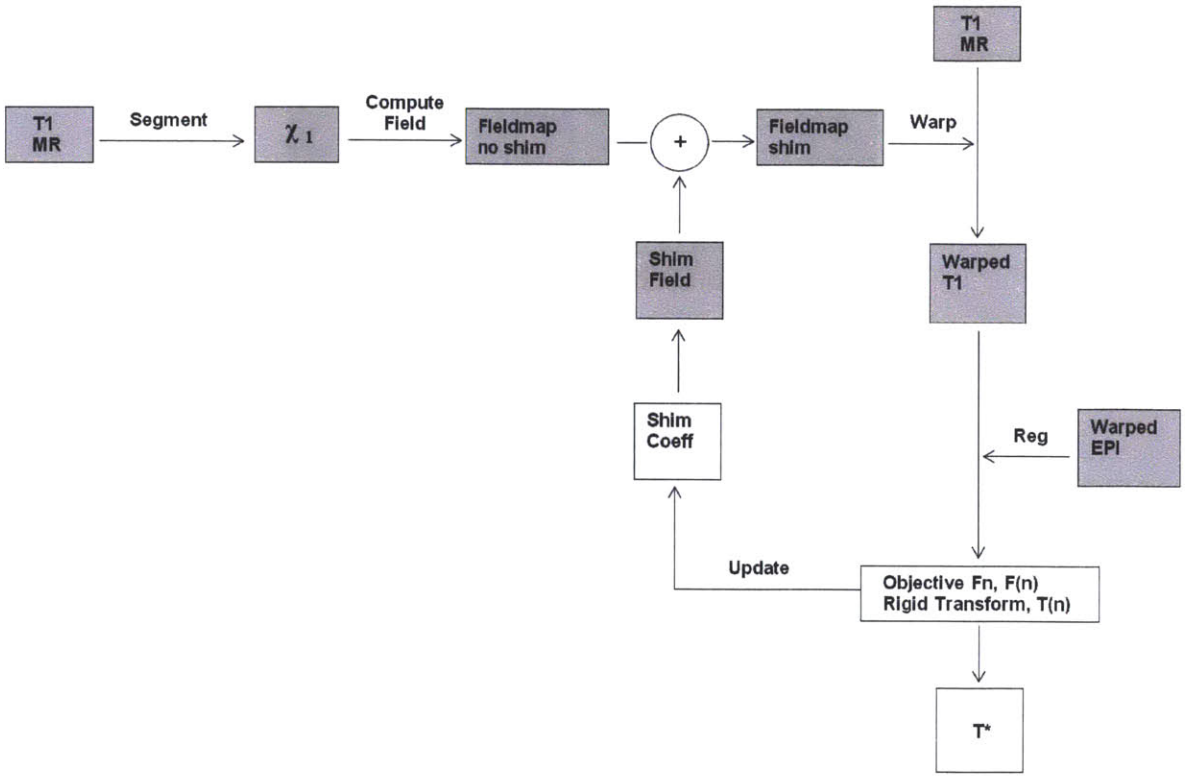

Figure 3-2: Fieldmap-Free Registration and Distortion Correction Algorithm. The susceptibility map obtained from segmenting the structural MR, χ_1, is used as input to the forward field model to obtain an initial estimate of the synthetic fieldmap. The shim coefficients are combined with the first and second order spherical harmonic basis functions to compute an estimate of the shim field that is then added to the initial fieldmap. The fieldmap (with shim) is used to warp the registered structural MR and the warped structural image is registered to the observed warped EPI data. This is repeated until optimal agreement between the warped EPI and warped structural image is obtained. Agreement is quantified using correlation ratio as the cost function and the matlab fminsearch algorithm is used to search over shim coefficients. The optimal transformation, T^*, can be applied to the final estimate of the synthetic fieldmap to register it to the warped EPI. The registered fieldmap is then used to correct the distortion.

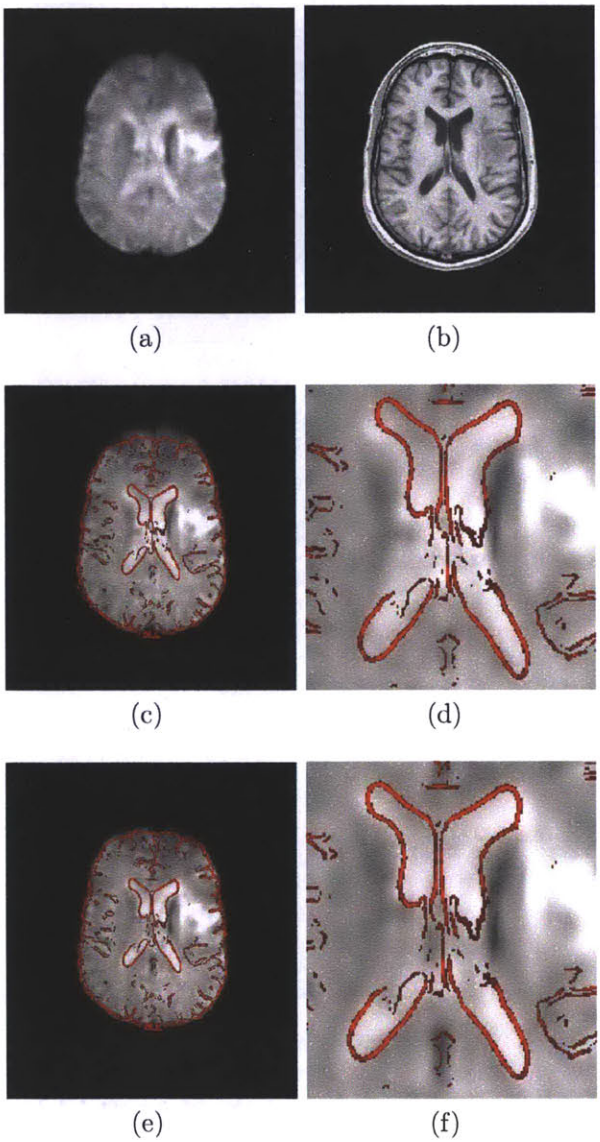

Figure 3-3: Fieldmap-based Unwarping and Registration. Registration of distorted EPI (a) to structural MR (b) using a 12 DOF affine transformation results in significant disagreement (c,d). Registration of the EPI following correction with an acquired fieldmap produces much better results (e,f). An edge strength image of the structural MR (red) is overlaid on the registered EPI (c-f) for visualization.

value can be obtained by calibration with a phantom; the offset is recorded in the fieldmap Dicom header. Factoring these known values out of the acquired fieldmap for validation purposes will still result in significant error between the estimated and acquired fieldmaps. This is because the estimated fieldmap does not include lower order spatial variations of the perturbation (or susceptibility-induced) field that are caused by anatomy outside the FOV (ie. the segmentation does not include the neck and torso). However, these neglected susceptibility fields from the body can be modeled using the same low order basis functions used to model the shims. Both can then be estimated and factored out by least squares fitting of the basis functions to the residual map (the difference between the estimated and acquired fieldmaps).

This approach works well for validation purposes [62], but presents a problem when the goal is to use an estimated fieldmap in place of an acquired fieldmap for distortion correction. Then both the shims and neglected susceptibility fields from outside the FOV are unknown and cannot be obtained from a simple fitting of the basis functions, since an acquired fieldmap is not available. Unwarping without accounting for shim can produce large errors as shown in Fig. 3-1. To overcome this problem, we model the shims and lower order susceptibility fields using the first and second order spherical harmonics and apply a simultaneous shim estimation and registration algorithm to solve for the expansion coefficients (shim parameters), which maximize agreement between the EPI and structural MR.

Our Fieldmap-Free registration and distortion correction algorithm is summarized in Fig. 3-2. An initial estimate of the shim parameters was obtained from the training data set of subject 1 using the least squares fitting method described previously. The initial estimate of the shim fields obtained from the training data was then added to the estimated fieldmap for the test subject and the fieldmap was masked to exclude non-brain voxels. This synthetic fieldmap must be registered to the EPI data before the unwarping can be done. Since the fieldmap is undistorted, but the EPI is distorted, registration errors may result, leading to inaccurate distortion correction. To prevent this, the synthetic fieldmap was used to warp the structural MR, which was previously co-registered to it. This warped structural image was then registered to

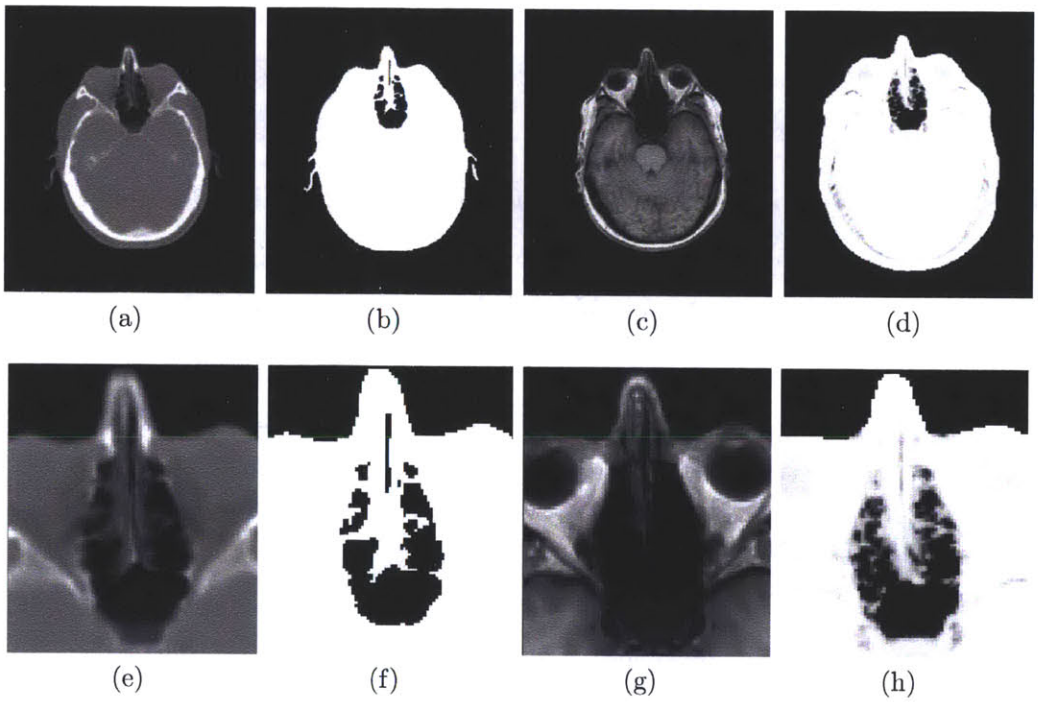

Figure 3-4: Results of the Classifier. The CT (a,e) is thresholded to produce a tissue/air susceptibility map (b,f) and the T1 (c,g) is segmented using the MR classifier to produce an estimated susceptibility map (d,h). Comparison of the MR-based and CT-based results shows good overall agreement, even in sinus regions where air/bone segmentation is difficult.

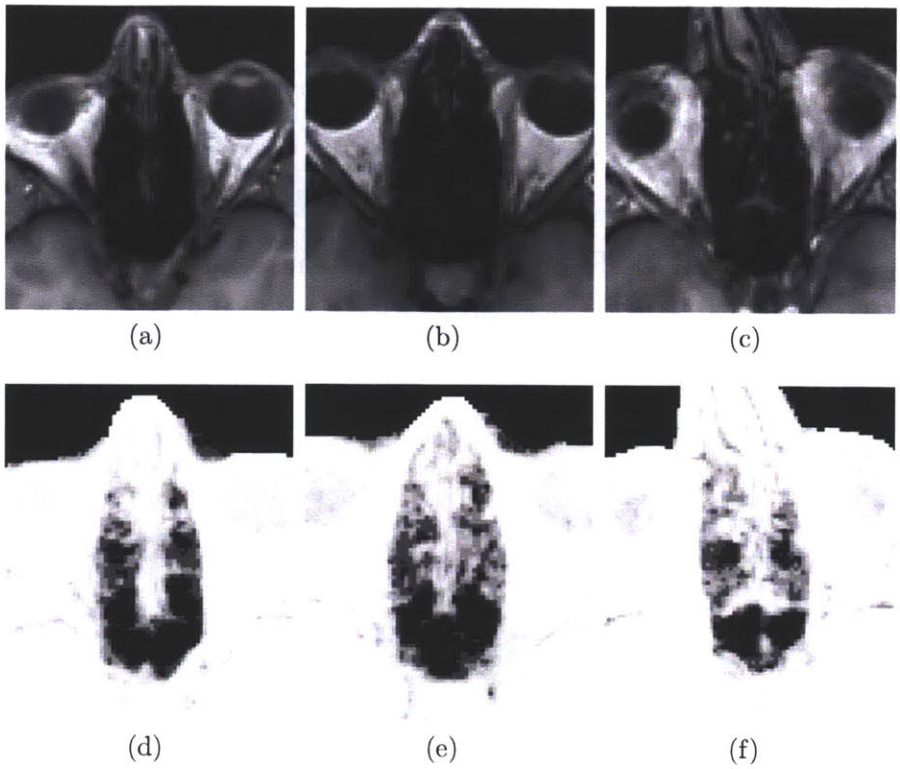

Figure 3-5: Results of the Classifier for Additional Subjects. The T1 structural images from three additional subjects show little signal from bone in the sinus region (a-c). The corresponding tissue/air segmentations are shown in (d-f). The MR classifier recovers tissue voxels in central regions of the sinuses that are likely to be bone (CT for these subjects was not available for validation).

the warped EPI and the process was repeated using a Matlab fminsearch algorithm (unconstrained nonlinear Nelder-Mead direct search method) to solve for the shim parameters (coefficients) which optimized agreement between the warped images. Once the optimal transform was obtained, it was applied to the fieldmap to register it to the distorted EPI and the fieldmap was used to unwarp the EPI data. Finally, the unwarped EPI was registered to the structural MR, using 6 DOF and correlation ratio as the cost function. All unwarping and registration was done using FUGUE and FLIRT. All calculations were programmed and executed in Matlab 2007a on a PC workstation running Debian Linux.

3.2 Experimental Results

The importance of correcting distortion in EPI prior to registration is illustrated in Fig. 3-3. Distorted EPI (Fig. 3-3a) from subject 2 is shown adjacent to the corresponding structural MR (Fig. 3-3b). Attempting to register the EPI directly to the structural MR using a 12 DOF affine transformation results in significant disagreement, which is most evident in the anterior region of the brain and the ventricles (Fig. 3-3c, Fig. 3-3d). In Fig. 3-3e, and Fig. 3-3f the EPI is first unwarped using the fieldmap-based method described in section 3.1.2. This significantly improves the agreement between the images, which is consistent with previously published work on this topic [30, 53].

3.2.1 Segmentation Results

The results of the MR classifier for subject 2 are shown in Fig. 3-4. While the CT (Fig. 3-4a) can clearly distinguish between bone and air, regions of the skull and sinuses have similar intensities in the MR (Fig. 3-4c), making segmentation more difficult. Segmentation using the MR classifier (Figs. 3-4d, 3-4h), however, agrees reasonably well with the segmented CT (Fig. 3-4b). Results for additional subjects are shown in Fig. 3-5.

3.2.2 Synthetic Fieldmap Results

The segmentations obtained from CT and structural MR were used as input to the forward field model to produce a fieldmap from the CT and an initial estimate of the synthetic fieldmap from MR. The fieldmap computed from the segmented CT is shown in Fig. 3-6a and the top of Fig. 3-6c, while the fieldmap from the segmented MR is shown in Fig. 3-6b and the bottom of Fig. 3-6c. The fieldmaps show excellent qualitative agreement. Quantitative analysis of the absolute error in the B_0 field between these images is given in the table in Fig. 3-6. Subvoxel error is achieved in 85% of voxels while the Mean and 90^{th} percentile values are significantly decreased relative to the error measurements reported by Koch et al [67].

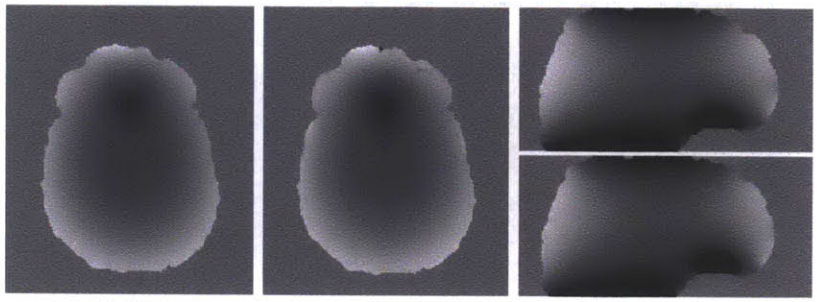

(a) (b) (c)

Absolute Difference in Field	Mean	Median	P85	P90	P95	P99
CT and MR fieldmaps (voxel shift)	0.544	0.342	0.849	1.014	1.331	2.650
CT and MR fieldmaps (Hz)	6.644	4.173	10.362	12.373	16.246	32.351
Koch et al. (Hz)	12.5	—	—	23.5	—	—

Figure 3-6: Results of the Initial Fieldmap Estimation. The fieldmap computed from the segmented CT (a, c-top) and the fieldmap computed from the segmented MR(b, c-bottom) show excellent agreement. The absolute difference in the fieldmaps from both segmentations is given in units of voxel shift in row 1 of the table and in Hz in row 2. P90 is the 90th percentile, etc. Results of Koch et al. [67] are given in Hz in row 3. The scale of the fieldmaps is ±200 Hz

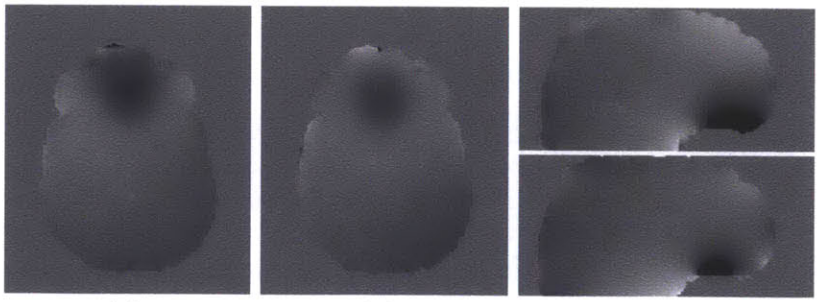

(a) (b) (c)

Figure 3-7: Synthetic Fieldmap Results from the Fieldmap-Free Algorithm. The acquired fieldmap (a,c-top) and the synthetic fieldmap estimated from the Fieldmap-Free registration algorithm (b,c-bottom) show good overall agreement. The scale of the fieldmaps is ±200 Hz.

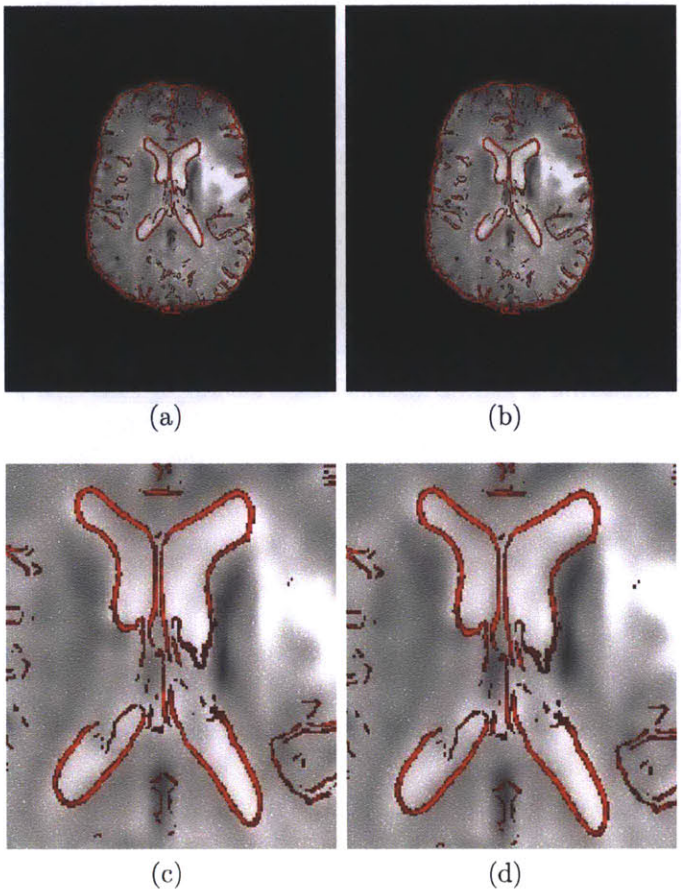

Figure 3-8: Registration Results. An edge strength image of the structural MR is overlaid on the registered EPI (a-d). Unwarping and registration with the acquired fieldmap is shown in (a,c). Unwarping and registration using the final synthetic fieldmap (b,d) results in excellent agreement between the EPI and structural MR.

The optimal shim fields were estimated using the simultaneous shim estimation and registration algorithm and added to the estimated fieldmap to produce the final synthetic fieldmap shown in Fig. 3-7b and the bottom of Fig. 3-7c. This result can now be compared to subject 2's acquired fieldmap, shown in Fig. 3-7a and the top of Fig. 3-7c. While some difference between the fieldmaps can be seen in the region closest to the air-filled sinuses, this does not result in a significant difference in the registration results.

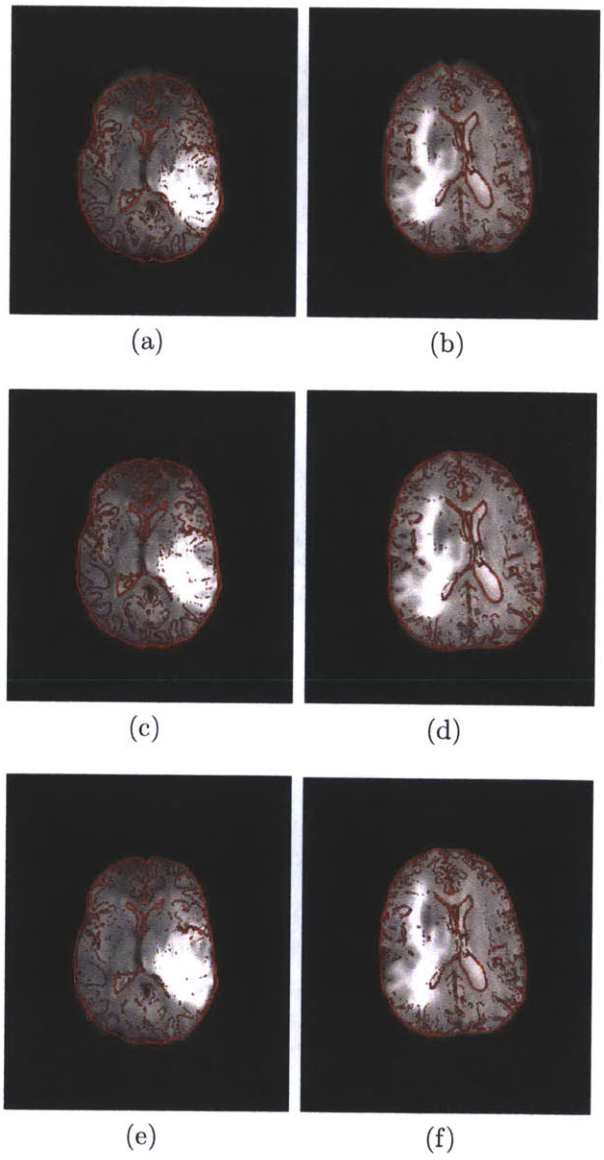

Figure 3-9: Results of the Distortion Correction on Additional Subjects. Registration of EPI data to structural MR (edge strength image shown in red) for 2 additional subjects without distortion correction shows poor agreement (a-b). Registration following correction with acquired fieldmaps shows good agreement (c-d). Registration results following correction with the FF method shows agreement that is comparable to those obtained with the measured fieldmaps (e-f).

3.2.3 Fieldmap-Free Distortion Correction and Registration Results

Visual inspection of the registration results (Fig. 3-8) shows equally good agreement between the EPI and T1 using either the synthetic fieldmap or acquired fieldmap. Quantititive comparison of the correlation ratio between the EPI and T1 also supports this conclusion: a value of 0.1516 was obtained when the acquired fieldmap was used for unwarping prior to registration versus a value of 0.1477 when the synthetic fieldmap was used. The discrepancy in the fieldmaps does not translate to the registration results because it occurs in areas in which there is severe signal loss in the EPI. In these areas there is little to no information to drive the estimation of more accurate shim parameters. Essentially, this region of the EPI is not sensitive to inaccuracies in the fieldmap because much of the signal intensity was lost during acquisition. Registration results for additional subjects are shown in Fig. 3-9.

3.3 Application to Diffusion Tensor Imaging

Acquisition of a set diffusion-weighted images (DWIs) allows diffusion tensors and tensor-derived quantities such as fractional anisotropy (FA) and trace (TR) to be computed and used to infer information about the underlying white matter structure in the brain. DWIs are usually acquired with an echo planar imaging (EPI) pulse sequence that produces images degraded by B_0 field inhomogeneity, eddy current distortion and head motion. The distortion results in errors in diffusion tensors and tensor-derived quantities such as FA. The B_0 distortion in EPI-based DWI can be corrected using acquired fieldmaps but these are typically unavailable in clinical studies. Eddy currents at acquisition time can be reduced, but not eliminated with gradient correction schemes [43]. In the remaining sections of this chapter, we apply our retrospective Fieldmap-Free (FF) method for B_0, eddy current and motion correction in the context of EPI-based DWI and compare it to previous work that uses acquired fieldmaps and registration-based eddy current correction [94, 121].

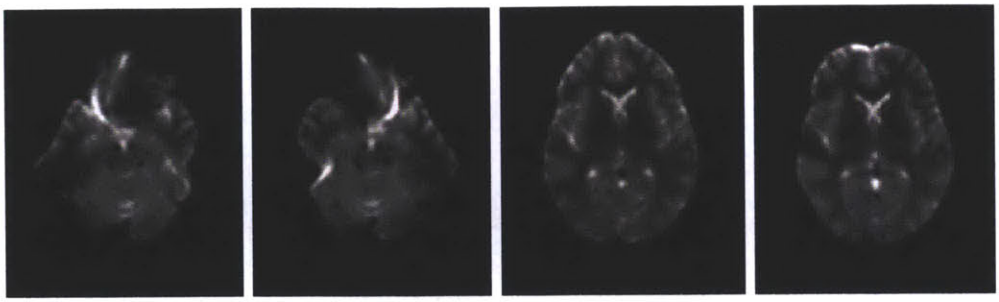

(a) (b) (c) (d)

Figure 3-10: DWI Data from a single subject in the DTI distortion correction study. Diffusion weighted images of a single subject with R/L phase encoding (a,b) and A/P phase encoding (c,d).

Performance of the FF method is evaluated using the experimental framework previously described by M. Wu and C. Pierpaoli et al [121]: distortion of EPI data due to B_0 and eddy current effects occurs primarily along the phase encode direction, allowing EPI data sets with different distortion conditions (determined by the phase encode direction and polarity of the gradient waveform) to be acquired for a single subject. Accurate unwarping of the distorted data sets should improve registration of the DWIs to structural T2-weighted images and reduce variability across distortion conditions in tensors, FA, and TR images for each subject.

3.3.1 Data Acquisition

Five young subjects (2 male; mean age = 35.95, range 24-48 years old) participated in [121]. Four axial DWI data sets for each subject were acquired: the phase encode direction was either anterior/posterior (A/P), or right/left (R/L), and the phase encode gradients had a positive or negative sign that resulted in four distortion conditions in which DWI data showed compression or expansion along the A/P and R/L axes as shown in Fig. 3-10. Data was acquired on a 1.5 Tesla GE scanner with a single-shot spin-echo EPI sequence: FOV = 24 x 24 cm, slice thickness = 2.5 mm, no gap, acquisition matrix = 96 x 96 zero filled to 128 x 128, and 60 axial slices. Each DWI data set consisted of 2 images with b = 0 s/mm^2 and 12 images with b = 1100 s/mm^2 with different orientations of diffusion sensitization. Undistorted T1-weighted (T1W) and

T2-weighted fast spin echo (T2WFSE) was acquired and two gradient echo images with different echo times were collected for B_0 mapping [121].

3.3.2 B_0 Distortion Correction using Acquired Fieldmaps

All DWI images were co-registered to the T2WFSE to correct for rigid body motion and eddy current distortion according to the method described in [94]. Distortion correction using the acquired B_0 fieldmaps (B0M) was performed using FSL's PRELUDE and FUGUE [58, 101] for comparison with FF results.

3.3.3 Fieldmap-Free Correction of B_0 and Eddy-Current Distortion

A tissue/air segmentation of the T1W data was obtained for fieldmap calculation as described in section 3.1.3. Unknown eddy current fields present in the DWIs (b = 1100 s/mm^2) were modeled using the same spherical harmonic basis used to model the shim fields. The FF method that was previously shown to be effective for correcting B_0 distortion in EPI-based functional data in section 3.2 was applied to correct the distorted DWIs. Following unwarping of each DWI in its native space, rigid body registration to the T2WFSE was carried out to allow comparison with the eddy plus acquired fieldmap correction method described in section 3.3.2.

3.3.4 Diffusion Tensor Calculations

In a DTI experiment, local diffusion is assumed to be characterized by a 3D Gaussian distribution, with a covariance matrix proportional to the diffusion tensor, **D**. The measured signal in each voxel for a given diffusion encoding direction, $\mathbf{g_i}$ and diffusion weighting, b_i, is modeled as:

$$S_i = S_0 \exp(-b_i \mathbf{g_i}^T \mathbf{D} \mathbf{g_i}) \quad , \tag{3.6}$$

where S_0 denotes the reference signal with no diffusion gradients applied [104, 8, 7, 66]. The diffusion tensor $\mathbf{D}$ is a 3 x 3 symmetric positive definite tensor given by:

$$\mathbf{D} = \begin{pmatrix} D_{xx} & D_{xy} & D_{xz} \\ D_{xy} & D_{yy} & D_{yz} \\ D_{xz} & D_{yz} & D_{zz} \end{pmatrix} .$$

The eigenvector corresponding to the largest eigenvalue of the diffusion tensor gives the principal diffusion direction, and a measure of the degree of anisotropy of diffusion is given by the fractional anisotropy (FA):

$$FA = \frac{\sqrt{3((\lambda_1 - \langle\lambda\rangle)^2 + (\lambda_2 - \langle\lambda\rangle)^2 + (\lambda_3 - \langle\lambda\rangle)^2)}}{\sqrt{2(\lambda_1^2 + \lambda_2^2 + \lambda_3^2)}} , \tag{3.7}$$

where λ_i with $i = 1, 2, 3$ are the eigenvalues of the diffusion tensor, $\langle\lambda\rangle$ is the mean value of these eigenvalues, and the FA $\in [0, 1]$ assuming the estimated diffusion tensor is positive definite. Maps of the FA and trace (TR) of the diffusion tensor were calculated using DTIfit in FSL which estimates eigenvalues using the probabilistic framework described in [10]. Standard Deviation (STD) maps of FA and TR across the four distortion conditions were computed for each subject.

3.3.5 Results

Fig. 3-11 shows STD maps of FA and Fig. 3-12 shows STD maps of TR. The maps were computed across the four distortion conditions for a representative subject using both the FF and B0M methods. Correction using the FF method agrees well with the B0M results, while the results without B_0 correction (NOC) show greater variability around the ventricles and frontal region. The mean FA and mean TR from data sets with FF correction are included as anatomical reference. Registration results are shown in Fig. 3-13 for a second subject. Results of the FF method for B_0 and eddy-current distortion correction agree well with those obtained by the eddy current and acquired fieldmap correction method and show improvement over the DWI corrected

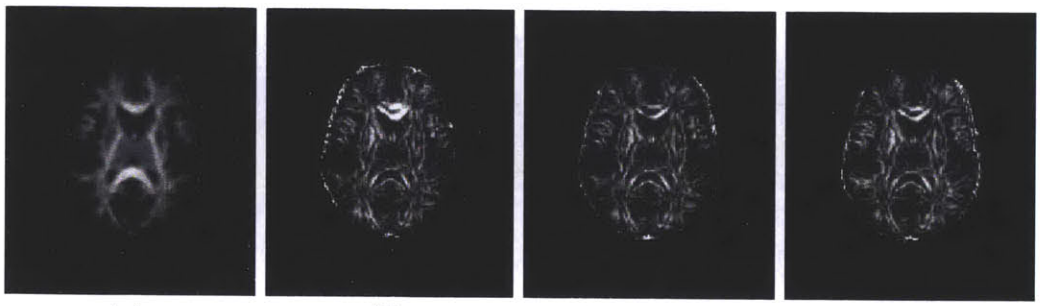

(a) (b) (c) (d)

Figure 3-11: Distortion Correction Results: Standard Deviation Maps of the Fractional Anisotropy (FA). The standard deviation of the FA for each subject was computed across the four distortion conditions with no correction applied (b), with correction using the acquired fieldmap (c) and correction using the FF method (d) (Display range: black = 0, white = 0.3). The mean FA image is shown in (a) for anatomical reference (Display range: 0, 0.95).

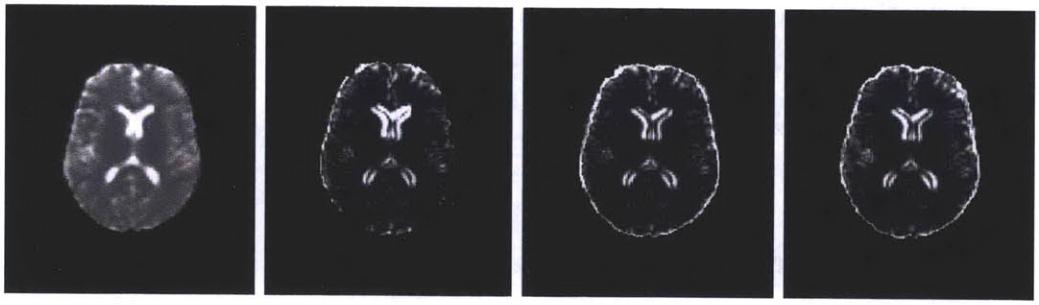

(a) (b) (c) (d)

Figure 3-12: Distortion Correction Results: Standard Deviation Maps of the Trace (TR). The standard deviation of the TR for each subject was computed across the four distortion conditions with no correction applied (b), with correction using the acquired fieldmap (c) and correction using the FF method (d) (Display range: black = 0 mm^2/s, white = $2.0 * 10^{-3} mm^2/s$). The mean TR image is shown in (a) for anatomical reference (Display range: 0, $5.0 * 10^{-3} mm^2/s$)

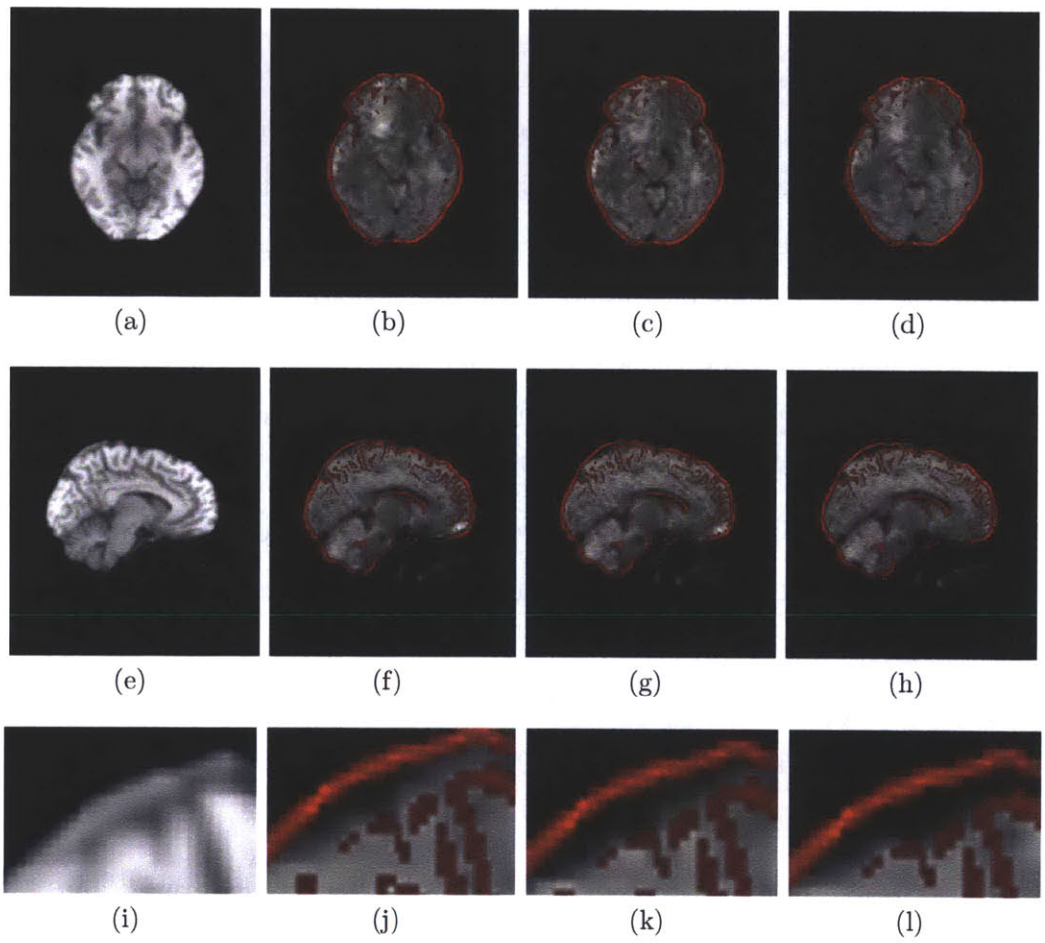

Figure 3-13: Registration Results for an Axial and Sagittal Slice of a Representative subject. Registration of DWIs following B_0 and eddy current distortion correction using the FF method (d,h) agree well with those obtained by the eddy plus B_0 fieldmap method (c,g) and show improvement over the DWI corrected for B_0 but not eddy distortion (b,f) An edge-strength image of the T1W data is shown in red for visualization of the registration results and a T1-weighted image is shown in (a,e) for reference. A closer view of the results in the saggital cross-section is shown in row 3.

for B_0 but not eddy current distortion. An edge-strength image of the T1W data is shown in red for visualization of the registration results.

3.4 Conclusions

We have demonstrated a novel Fieldmap-Free EPI Fieldmap-Free unwarping and registration algorithm. CT data was used to train an MR classifier that computes tissue/air susceptibility maps and its performance was evaluated on new data given only the relevant T1-weighted MR. The segmented MR was used as input to the shim estimation and registration algorithm to compute synthetic fieldmaps that agreed well with the corresponding acquired fieldmaps. Registration results following unwarping with synthetic fieldmaps showed excellent agreement with standard fieldmap-based methods.

In addition, the FF method was applied to correct the eddy-current and B0 distortion present in DWI data. The FF method reduced the variability of FA and TR computed from DWI data obtained from four different distortion conditions, and produced results that agreed well with the eddy-current correction plus acquired fieldmap technique (B0M) described in section 3.3.2. FF results also showed improvement over those obtained using fieldmap correction, but no eddy-current correction.

The FF approach overcomes limitations of current unwarping strategies such as the need for additional scan time, pulse-sequence modification, acquisition of CT data, or knowledge of shim parameters. Results from the DTI experiment show that the FF method provides a new technique for retrospective eddy-current and B0 distortion correction in EPI-based DWI. Therefore, this method provides a fieldmap-free, subject-specific EPI unwarping and registration technique particularly suitable for clinical applications and retrospective functional neuroimaging research.

Chapter 4

Atlas-based Improved Prediction of Magnetic Field Inhomogeneity for Distortion Correction of EPI data

In Chapter 3 we showed that tissue/air susceptibility models could be derived from structural MRI by using an intensity-based classifier trained with CT. Registration of the EPI and structural MR could be used to search over the unknown shim parameters allowing distortion correction of the EPI that agrees well with results obtained using acquired fieldmaps.

Variability in structural MR acquisitions, however, may limit the efficacy of an intensity-based classifier in cases where the MR intensity properties differ significantly from those of the training data. In Chapter 3, CT data sets with MR acquired on the same scanner as the subjects of interest could be used to train the classifier, but this may not be possible in many cases. Limited anatomical information below the brain may also prevent accurate estimation of the perturbing field. Therefore, obtaining more reliable susceptibility models from structural MR is critical for retrospective unwarping of EPI data sets that lack acquired fieldmaps. While previous results predicting fieldmaps from structural MR have shown good agreement with acquired fieldmaps, we hypothesized that improved segmentation methods would result in even greater accuracy.

In this chapter, we describe a method for atlas-based segmentation of structural MRI for calculation of synthetic fieldmaps. First, a set of 22 whole-head CT data sets are used to construct a probabilistic atlas of the head that provides priors on the probability of tissue, air, and bone at each location in the anatomy. Second, corresponding structural MR is used to train a classifier that segments structural data of the subject of interest into soft tissue, air, and bone. Subject-specific fieldmaps are computed from the segmentations using the spatial formulation of the forward field model. Finally, the MR classifier is used to obtain probabilistic bone segmentations from structural MR that show promising agreement with segmented CT.

4.1 Methods

4.1.1 Data Acquisition

For construction of the atlas, we obtained 22 datasets consisting of CT and MRI from three sources: the publicly available Retrospective Image Registration Evaluation (RIRE) database (17 neurosurgery patients), the Radiology department at Brigham and Women's Hospital (BWH) (4 neurosurgery patients) and the Zubal head phantom (1 subject) [127]. In the RIRE data, each CT image has 27 to 34 slices, 4 mm thick, acquisition matrix = 512 x 512, voxel size = 0.65 x 0.65 mm. The T1-weighted MRI was acquired on a Siemens SP 1.5 Tesla scanner. MRI for 8 of the 17 subjects has 20 to 26 axial slices, 4 mm thick, no gap, acquisition matrix = 256 x 256, voxel size = 1.25 x 1.25 mm, TE = 15 ms, TR = 650 ms. T1-weighted MPRAGE for the other 9 subjects had TE = 4 ms, TR = 10 ms, acquisition matrix = 128 x 256 x 256 and FOV = 160 x 250 x 250 mm. In the BWH dataset, the CT spanned 36 slices with 512 x 512 in-plane voxels of size 0.46 x 0.46 x 4.8 mm. 3D-SPGR MRI of these patients was obtained: slice thickness = 1mm, TE = 3 ms, TR = 8 ms, acquisition matrix = 512 x 512, voxel size = 0.5 x 0.5 x 1 mm. The Zubal data consists of CT of the head and neck: 1.2 mm isotropic voxels spanning 230 slices with 256 x 256 in-plane voxels, and T1-weighted MRI with 90 slices of thickness 0.2 cm, acquisition matrix = 256 x

256, and 25.6 x 25.6 cm in-plane resolution.

For validation of synthetic fieldmaps computed from atlas-based segmentations, we obtained T1-weighted MRI and gradient echo fieldmaps of 5 subjects previously acquired at Massachusetts General Hospital on a 3T Siemens TimTrio scanner as part of the FBIRN multi-center FMRI study [65]. The MPRAGE spanned 160 slices, with thickness = 1.2 mm, acquisition matrix = 256 x 256, voxel size = 0.86 x 0.86 mm, TE = 2.94 ms, and TR = 2300 ms. The fieldmaps had 30 slices, thickness = 5 mm, acquisition matrix = 64 x 64, voxel size = 3.44 x 3.44 mm, TE_1 = 3.03 ms, TE_2 = 5.49 ms, TR = 500 ms.

4.1.2 Atlas Construction

Automatic segmentation of neuroanatomical structures often relies on the use of probabilistic atlases [39, 110, 92, 48, 126]. These atlases are usually constructed by co-registering collections of manual segmentations or other training data. The atlas functions as a spatial prior to represent anatomical variability within a population and compensate for missing information in structural MR images [126]. Although atlas-based methods have typically been applied to the segmentation of brain structures, in this work, we construct a probabilistic tissue/air atlas from 22 CT data sets. By incorporating spatial information into the MR segmentation, we expect improved tissue/air classification in regions where bone is often mis-labeled as air.

For each subject, the CT data was registered to its corresponding MR using 6 degrees of freedom (DOF) and mutual information as the cost function. The MR was registered to standard space using the MNI152T1 atlas as the reference, 12 DOF affine transformation and normalized correlation ratio. These transformations were then applied to the co-registered CT. All registrations were carried out using FLIRT [61, 60]. Tissue/air labels were obtained by thresholding the CT data in standard space.

The wide variation in the field of view of the CT data results in highly varying amounts of data at each voxel; in particular only the zubal phantom includes observations in the neck. Probabilistic atlases are frequently constructed by counting the

number of occurrences of each tissue class at each voxel and normalizing the result to obtain a probability distribution. In the two class situation, this corresponds to Maximum Liklihood (ML) estimation of the parameter of a binomial distribution, i.e., if $k \sim \text{Binomial}(n, p)$, then, the ML estimate of p given observed k is $\hat{p} = k/n$. In the case of only one trial ($n = 1$), or one observation at a given voxel, this will lead to estimates of p that are zero or one, which may be unreasonably certain (i.e. when used as prior probability on tissue class in segmentation, these values would dominate any amount of data in these voxels).

One way to avoid this effect, is to put a prior on p; a natural choice is the beta distribution, which is conjugate to the binomial: $p \sim \text{Beta}(\alpha, \beta)$. (The special case of $\alpha = \beta = 1$ corresponds to a flat prior and Laplace's rule of succession). We have chosen to use $\alpha = \beta = \epsilon = 0.05$, and in this case, the posterior expected value of the parameter is $\bar{p} = \frac{k+\epsilon}{n+2\epsilon}$, which avoids, by ϵ, the probability zero and one cases mentioned above. In addition to the tissue/air atlas, a probabilistic atlas of bone was obtained by segmenting bone from CT data and applying the same binomial model and conjugate prior. This was applied to segment bone from MR, which may be useful in other applications such as calculation of attenuation maps for absorption correction in PET or dose calculation in radiotherapy planning.

4.1.3 Atlas-based Segmentation

Structural MR was segmented using an MR classifier that incorporates spatially dependent prior information from the probabilistic atlas and MR intensity information (from the subject of interest) to obtain a subject-specific susceptibility model. The classifier was trained using the CT/MR training data described in section 4.1.1, but applied to segment MR data acquired in the FBIRN study [65]. The accuracy of the segmentations was evaluated by comparing fieldmaps predicted from the atlas-based segmenter to acquired fieldmaps. The fieldmaps were also compared to those predicted using intensity information alone (ie. a spatially constant prior).

Rigid (6 DOF) registration of the FBIRN T1-weighted data to the fieldmap magnitude data was carried out using FLIRT [61] so the predicted fieldmaps would be

in the same space as the acquired fieldmaps for validation. The MNI152T1 reference image was registered to the fieldmap magnitude image using a 12 DOF affine deformation model and the resulting transformation was applied to the atlas-based probability maps. The probability of tissue given MR intensity can then be computed by:

$$P(T \mid I_i) = \frac{P(I_i \mid T)P(T \mid X_n)}{P(I_i \mid T)P(T \mid X_n) + P(I_i \mid T^C)P(T^C \mid X_n)} \quad , \tag{4.1}$$

where I_i denotes the i^{th} MR intensity bin and the random variable $t \in \{T, T^C\}$, corresponding to labels {Tissue, Air}. The prior probabilities of tissue, $P(T \mid X_n)$, and air, $P(T^C \mid X_n)$, at each voxel location X_n were obtained from the co-registered atlas. For each of the 22 T1 images in the training data, the MR was scaled according to the parameter that minimized the Kullback-Leibler Distance to the MR of the subject of interest. The data that showed the minimal distance to the subject of interest was used to compute the likelihood terms, $P(I_i \mid T)$ and $P(I_i \mid T^C)$, using tissue/air labels from the corresponding CT. The posterior probability of tissue was computed and applied to segment the MR of the subject of interest. Intensity-based segmentation using spatially stationary priors computed from normalized intensity histograms of the training data was also carried out for comparison to the atlas-based approach.

Bone segmentations were obtained in similar fashion and evaluated using a 'leave-one-out' framework in which one CT was withheld as ground truth and the remaining CT data sets were used to construct the probabilistic bone atlas. A non-linear direct search was performed to solve for the thresholds that maximized the similarity of the estimated bone segmentations to the ground truth segmentation. The similarity was quantified using the dice score, which is defined as the number of intersecting voxels divided by the average number of voxels in each volume; a value of 0 indicates the volumes have no overlapping voxels and a value of 1 indicates they are exactly the same [34, 74].

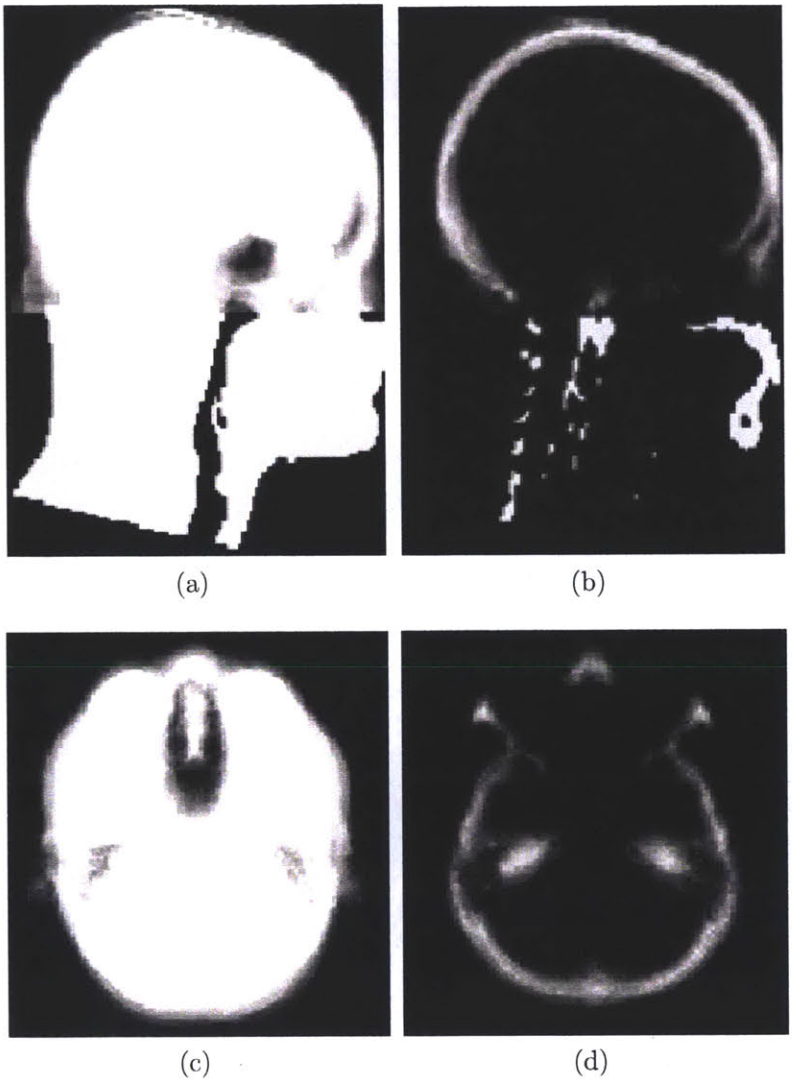

Figure 4-1: Results of the Atlas Construction. Sagittal views of the tissue/air atlas (including both soft tissue and bone) is shown in (a) and the atlas showing the probability of bone is shown in (b). The corresponding axial views are shown in (c) and (d), respectively. The probability maps account well for variability across subjects in the brain and upper head region. In the more inferior regions of the head and neck, only a single observation from the Zubal CT was available. The intensity scale is $[0, 1]$.

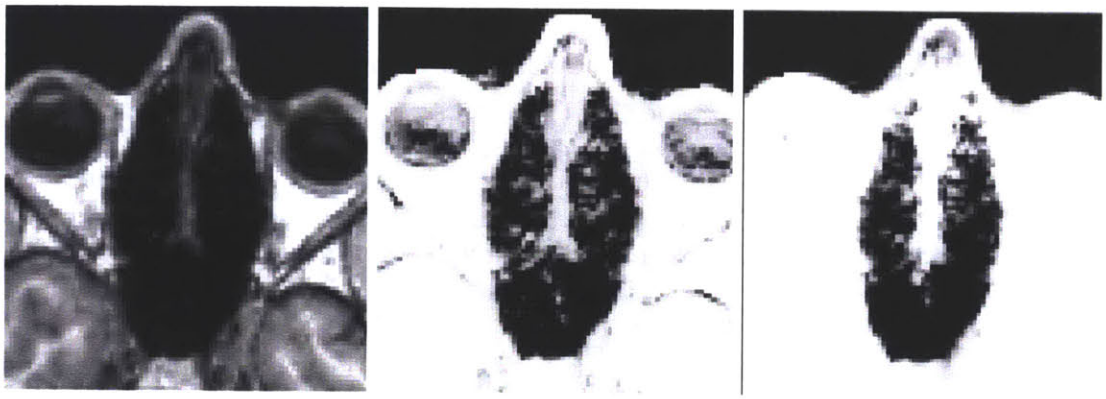

(a) (b) (c)

Figure 4-2: Results of the Segmentation. The T1-weighted MR for a representative subject is shown in (a). The tissue probability map computed using the intensity classifier (b) shows misclassification of voxels outside the sinus region where intensities are low in MR. Using the atlas-based classifier significantly reduces these errors while adequately resolving much of the subject-specific sinus anatomy (c).

4.1.4 Fieldmap Estimation

Synthetic fieldmaps are predicted from the atlas and intensity-based segmentations using the spatial formulation of the forward field model described in detail in Chapter 2. In this model, a first order perturbation solution of Maxwell's equations is calculated from a tissue/air susceptibility model, where each pixel, χ_1, takes continuous values between 0 (air) and 1 (tissue). The χ_1 labels were set equal to the posterior probabilities, $P(T \mid I_i)$, and used to compute subject-specific fieldmaps.

Current field modeling techniques, including the forward model used here, do not account for the shim fields that reduce the B_0 inhomogeneity prior to fieldmap acquisition. In order to compare an estimated fieldmap to an acquired one, the shim fields must added to the predicted fieldmaps. Since the shim coils are manufactured to produce fields based on a spherical harmonics expansion [27], they can be modeled using the set of first and second order spherical harmonic basis functions in cartesian form. In addition, a global scaling of the predicted fieldmap must be estimated since the model assumes the magnetic susceptibility throughout the brain ($\chi_t \approx -9.1 \times 10^{-6}$) is constant [62], but this may not be accurate near bone interfaces where both partial volume effects and mis-estimation of segmentation values are most likely

to occur. Furthermore, the perturbing fieldmaps are calculated assuming a perfectly homogeneous B_0 field, which cannot be achieved in practice due to constraints on the hardware. The fieldmap scaling and shim parameters, θ, can be obtained by least squares fitting to the acquired fieldmap: $\hat{\theta} = \arg\min_{\theta} [\mathbf{B} - \mathbf{A}\theta]^2$ where $\mathbf{A} = \left[\hat{\mathbf{B}}, \mathbf{S_1}, \mathbf{S_2}, ..., \mathbf{S_8}\right]$. The column vectors $\mathbf{B}$, $\hat{\mathbf{B}}$, and $\mathbf{S_i}$, represent the acquired fieldmap, predicted fieldmap, and shim basis functions, respectively. Once these coefficients are known, the predicted fieldmap with shim, $\hat{\mathbf{B}}_\mathbf{s} = \mathbf{A}\hat{\theta}$, can be compared to the acquired fieldmap.

4.2 Experimental Results

4.2.1 Results of the Atlas Construction

The results of the atlas construction are shown in Fig 4-1. The atlas contains two volumes: a map of the probability of tissue (where tissue includes both soft tissue and bone) and a map of the probability of bone. From these volumes the probabilities of soft tissue, bone, and air can be obtained for each point in the field of view (FOV). The probability maps successfully capture the anatomical variability across subjects in the brain and superior head. In the inferior parts of the head and neck, only a single observation from the zubal CT was available, corresponding to a $P(T \mid I_i) \approx 0.9545$ and the choice of $\alpha = \beta = \epsilon = 0.05$ as described in Section 4.1.2. The atlases shown in Fig. 4-1 can then be used as priors in the segmentation of structural MR.

4.2.2 Segmentation Results

Results of atlas-based segmentation of structural MR is shown in Fig. 4-2. Fig. 4-2a shows T1-weighted MR of the sinus region. Fig. 4-2b shows the limitations of using the intensity classifier to segment the MR. While it produces reasonable results for many of the voxels in the sinuses, voxels outside this region which are clearly soft tissue or bone are mislabeled with values close to zero (ie. in the eyes). In contrast, using the atlas-based segmenter (as shown in Fig. 4-2c) achieves similar results for

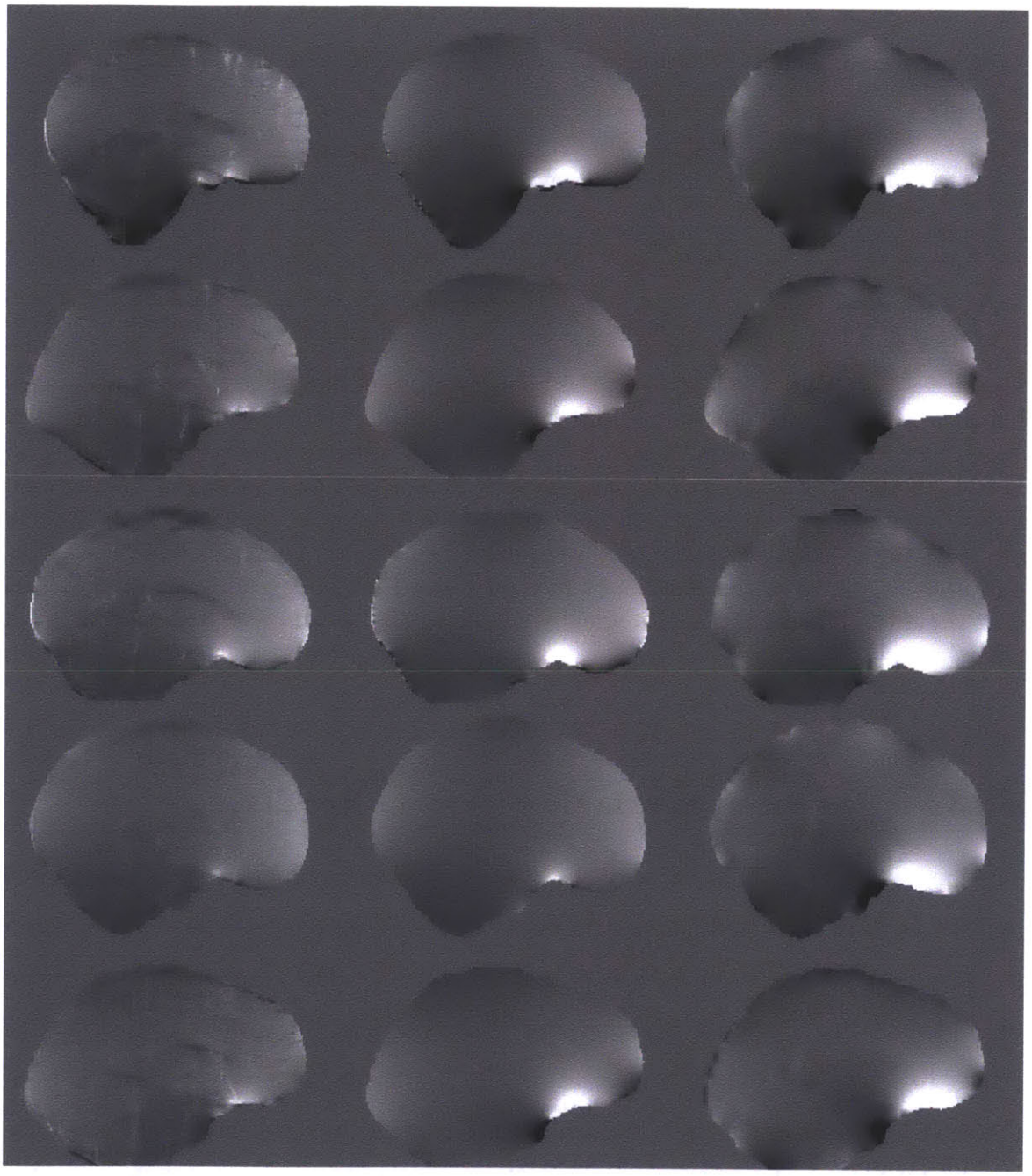

Figure 4-3: Results of the Fieldmap Estimation. Predicted and acquired fieldmaps for subjects 1-5 are shown in rows 1-5 respectively. Fieldmaps predicted using the intensity classifier (column 1) show significant differences relative to the acquired fieldmaps (column 3), while those computed from the atlas-based segmentation show improved agreement (column 2). The scale of the fieldmaps is ± 100 Hz.

the highly variable subject-specific anatomy within the sinus region, while producing fewer errors in the surrounding area.

Difference in Field (Hz)	Mean	P80	P85	P90	P95	P99
Subject 1	8.8	12.2	15.0	19.8	31.0	69.1
Subject 2	8.2	11.7	14.2	18.3	27.4	59.8
Subject 3	8.4	12.3	15.1	19.3	27.6	54.6
Subject 4	9.0	12.7	15.7	20.3	30.2	72.6
Subject 5	6.5	8.8	11.0	14.8	22.9	50.1
Koch et al.	**12.5**	—	—	**23.5**	—	—
$\mu_{intensity}$	**10.0**	14.1	17.5	**23.2**	34.9	74.8
μ_{atlas}	**8.2**	11.5	14.2	**18.5**	27.8	61.2
p-values	**0.0080**	0.0087	0.0081	**0.0079**	0.0093	0.0106

Figure 4-4: Quantitative Results of the Fieldmap Estimation. The absolute difference between the acquired fieldmaps and the atlas-based fieldmaps are given for each subject in the table above. 90% of voxels show differences that are less than 22.3 Hz, the bandwidth/pixel for the FBIRN EPI data. Results reported by Koch et al. [8] for a single subject are shown, as well as mean statistics across all five subjects for both the intensity classifier and atlas-based classifier. The atlas-based classifier performs better than the Koch and intensity-based methods and the improvement over the intensity method is statistically significant (all p-values < 0.05 for left-sided paired t-test).

4.2.3 Atlas-based Synthetic Fieldmap Results

The intensity and atlas-based segmentations were used as input to the forward field model to obtain predicted fieldmaps. The scaling and shim parameters were fit from the acquired fieldmaps as described in section 4.1.4. The shim fields could then be added to the predicted fieldmaps for comparison to the acquired fieldmaps as shown in Fig. 4-3. The first column of Fig. 4-3 shows fieldmaps computed from the intensity-based segmentations, which show significant differences relative to the acquired fieldmaps shown for each subject in column 3. These are especially noticable in areas that have lower signal in MR, such as in the ventricles and major sulci. Fieldmap results from the atlas-based segmentations are shown in the second column of Fig. 4-3 and show improved agreement with acquired fieldmaps. Quantitative analysis of the absolute error in the B_0 field between these images is given in Fig. 4-4. Since the bandwidth/pixel for the EPI data acquired in this study is 22.3 Hz, 90%

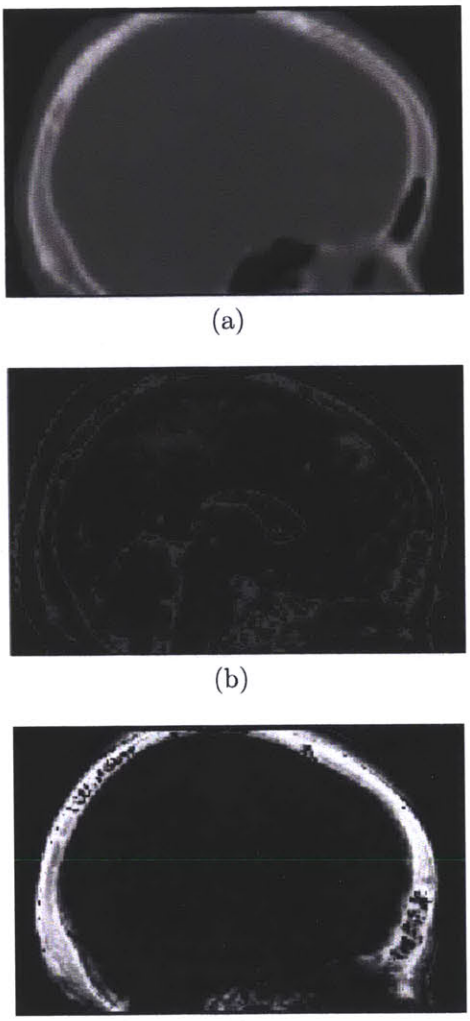

(a)

(b)

(c)

Figure 4-5: Results of the Bone Segmentation. Segmentation of bone using the intensity classifier (b) results in significant errors when compared with CT (a), while the atlas-based classifier (c) shows good overall agreement

of the voxels in the atlas-based fieldmaps show subvoxel error. The mean of these statistics across all five subjects is also shown for both the intensity ($\mu_{intensity}$) and atlas-based classifiers (μ_{atlas}). The intensity classifier shows a slight improvement over the results reported by Koch et al. [67] for a single subject. The atlas-based classifier out performs both the intensity and Koch methods. Paired t-tests comparing the means of the intensity and atlas-based results shows this improvement is statistically significant (all p-values < 0.05).

4.2.4 Results of the Bone Segmentation

Results of the segmentation of bone from structural MR for a representative subject are shown in Fig. 4-5. The CT shown in Fig. 4-5a can be easily thresholded to segment bone from air and soft tissue. Fig. 4-5b and Fig. 4-5c show the results of using the intensity and atlas-based classifiers, respectively. While the intensity classifier has some success in segmenting MR into tissue/air classes, it is much less effective in segmenting bone (Fig. 4-5b). Inspection of the the atlas-based segmentation (Fig. 4-5c), however, shows good general agreement with the CT, with a dice score of 0.780 for this subject.

4.3 Conclusions

In this chapter we showed that atlas-based fieldmap prediction provides results that agree well with acquired fieldmaps: 90% of voxel shifts from synthetic fieldmaps show subvoxel disagreement compared to those computed from acquired fieldmaps. In addition, our fieldmap predictions show statistically significant improvement following inclusion of the atlas. Finally, we showed that the MR classifier can be used to obtain probabilistic bone segmentations from structural MR that show promising agreement with segmented CT.

Chapter 5

An Atlas-based Approach to Quantitative Susceptibility Mapping

In this chapter, we describe an atlas-based approach for quantitative susceptibility mapping. We derive an inhomogeneous wave equation that relates the Laplacian of the observed field to the D'Alembertian of susceptibility, and eliminates confounding biasfields. Since active shims produce fields that can be modeled with a spherical harmonic expansion, which is a solution of the Laplace equation, the effects of any mis-set shims and remote susceptibility distributions (ie. the neck/chest) are effectively eliminated by taking the Laplacian of the observed magnetic field [76, 98]. In Chapter 2 we described how local susceptibility distributions can produce low-order fields that may appear to be due to sources outside the region of interest, requiring some form of regularization in the form of prior models, or atlases to obtain accurate susceptibility estimates. In this work, we investigate two regularization strategies. The first uses the fieldmap magnitude image as a prior on spatial frequency structure by enforcing agreement between the estimated susceptibility distribution and magnitude data in k-space. The second enforces agreement between the estimated susceptibility distribution and the tissue/air susceptibility atlas described in Chapter 4. The performance of the first method is evaluated using phantom data. The

atlas-based susceptibility mapping (ASM) technique is evaluated using in-vivo data by comparison of mean susceptibility values in the thalamus (TH), caudate (CD), putamen (PT) and globus pallidus (GP) to previously reported postmortem iron measurements. In addition, ASM results are compared to those obtained using both susceptibility-weighted imaging (SWI) and field dependent transverse relaxation rate imaging (FDRI) in a study of iron accumulation in normal aging.

5.1 Methods

5.1.1 Derivation of an Inhomogeneous Wave Equation for Susceptibility Estimation

Biasfield removal can be accomplished by application of the Laplacian to the measured field. For discrete media, the Lorentz Corrected solution of Maxwell's equations for the perturbing field results in the forward model given in Eq. 2.81:

$$B_z^{(1)} = \frac{\chi_1}{3+\chi_0} B_z^{(0)} - \frac{1}{1+\chi_0}\left(\left(\frac{\partial^2 G}{\partial x \partial z}\right) * (\chi_1 B_x^{(0)}) + \left(\frac{\partial^2 G}{\partial y \partial z}\right) * (\chi_1 B_y^{(0)}) + \left(\frac{\partial^2 G}{\partial z^2}\right) * (\chi_1 B_z^{(0)})\right) \quad . \tag{5.1}$$

For notational clarity, we will omit the subscript from χ_1 and the factor of 4π in the Green's function. Since $\chi_0 << 1$ and assuming a main field along the z-direction, $B^{(0)} = B_z^{(0)} = B_0$, we can begin with the simplified model:

$$B = B_0\left(\frac{\chi}{3} - \left(\frac{\partial^2}{\partial z^2}\frac{1}{r} * \chi\right)\right) \quad , \tag{5.2}$$

where χ is the unknown susceptibility map, and $r = \sqrt{x^2+y^2+z^2}$. This equation consists of a local term, $B_0(\chi/3)$, and the convolution of χ with the second z-derivitive of the $1/r$ distribution, where $1/r$ is the Green's function for the Laplacian [62].

Eq. 5.2 can be rearranged to give:

$$\frac{B}{B_0} - \frac{\chi}{3} = -\left(\frac{\partial^2}{\partial z^2}\frac{1}{r} * \chi\right) \tag{5.3}$$

$$= \frac{1}{r} * -\frac{\partial^2 \chi}{\partial z^2} \quad . \tag{5.4}$$

Using the fact that $1/r$ is the Green's function for the Laplacian (which we denote here by Δ) Eq. 5.4 can be written:

$$\Delta\left(\frac{B}{B_0} - \frac{\chi}{3}\right) = -\frac{\partial^2 \chi}{\partial z^2} \quad . \tag{5.5}$$

Rearranging Eq. 5.5 gives:

$$\frac{\Delta B}{B_0} = \frac{\Delta \chi}{3} - \frac{\partial^2 \chi}{\partial z^2} \tag{5.6}$$

$$= \frac{1}{3}\left[\frac{\partial^2}{\partial x^2} + \frac{\partial^2}{\partial y^2} - 2\frac{\partial^2}{\partial z^2}\right]\chi \tag{5.7}$$

This can be written concisely as an inhomogeneous wave equation,

$$\Box\chi = 3\Delta B/B_0 \quad \text{where} \quad \Box = \frac{\partial^2}{\partial x^2} + \frac{\partial^2}{\partial y^2} - \frac{1}{c^2}\frac{\partial^2}{\partial t^2} \quad , \tag{5.8}$$

here $\Box$ is the D'Alembertian wave equation operator with two space dimensions, x and y, with z taking the place of time, and speed, $c = 1/\sqrt{2}$. Since χ represents the object in the scanner and needs to be specified as a continuous function of space for application of Eq. 5.2, this makes the required convolutions analytically intractable and therefore a discrete approximation of the object using voxels is required. The convolution in Eq. 5.2 can then be calculated analytically for a single voxel [62], yielding the discrete approximation, $H = \frac{\partial^2}{\partial z^2}\frac{1}{r} * \chi \propto \text{atan}(\frac{xy}{zr})$, for a constant main field along the z-direction. The single voxel solution is convolved, via 3D Fast Fourier Transforms (FFTs), with the susceptibility map and added to the local term in Eq. 5.2

to give the total field:

$$B = B_0(\frac{\chi}{3} - H * \chi) \quad = \quad B_0(\frac{\delta}{3} - H) * \chi \quad = \quad C * \chi \quad , \tag{5.9}$$

where δ is the Dirac delta function and $C = B_0(\frac{\delta}{3} - H)$. The convolution in Eq. 5.9 can be implemented efficiently using FFTs and written in matrix form as $B = K\chi$.

5.1.2 Regularization using a Magnitude Prior in Fourier Space

Previous work has shown that MR images can be successfully reconstructed from under-sampled observations by exploiting the sparsity of in-vivo data under various transformations using methods from compressed sensing [80]. In susceptibility estimation, the forward model results in under-sampling of the data in the Fourier domain, but we hypothesized that accurate estimates can be obtained using the Laplacian and L1 norm, which promote sparse solutions while removing external field artifacts. Enforcing agreement of spatial frequency structure between the estimated susceptibility map and fieldmap magnitude data provides regularization, resulting in the optimization problem:

$$\min_{\chi} \left| F\left(\frac{\chi}{c_1}\right) - F\left(\frac{M}{c_2}\right) \right|_2^2 \quad s.t. \quad \left| W\left(\Delta B - \frac{B_0}{3}\Box\chi\right) \right|_1 < \epsilon \quad , \tag{5.10}$$

where M represents the fieldmap magnitude image, F denotes the Fourier transform, W is a mask of the region of interest, and c_1 and c_2 are constants. The second term penalizes departures from Eq. 5.8, effectively, by enforcing agreement of high frequency phase effects while removing low order bias fields. The optimization is implemented using Lagrange multipliers and solved using conjugate gradient.

5.1.3 Atlas-based Susceptibility Estimation

Quantifying susceptibility from MR phase data is difficult since operations that map susceptibility to field measurements or the Laplacian of the field, such as K or $\Box$, result in information loss due to derivitives or the presence of zeros in the Fourier

space kernel. Using a magnitude prior to provide regularization as described in section 5.1.2 assumes very similar spatial frequency structure between the magnitude image and unknown susceptibiliy distribution, which may not be true for in-vivo brain data. Probabilistic atlases are frequently used to compensate for missing information in MR data and for segmentation of neuroanatomical structures [92, 126]. In Chapter 4 it was shown that structural MR images of the head can be segmented into tissue/air susceptibility maps using a tissue/air atlas constructed from CT data. Voxels in the resulting atlas-based segmentation take continuous values between $[0, 1]$ corresponding to susceptibilities ranging from $\chi_{air} \approx 0.4$ ppm to $\chi_{tissue} \approx -9.1$ ppm. In this section, we describe a variational approach for atlas-based susceptibility mapping that performs simultaneous susceptibility estimation and biasfield removal using the Laplacian and a tissue/air susceptibility atlas. Prior anatomical information is incorporated through the atlas-based susceptibility model.

The tissue/air atlas described in Chapter 4 is transformed from standard space to each magnitude image by registering the standard space MNI152T1 atlas to the subject of interest, using 12 degrees of freedom and normalized correlation ratio, and the resulting transform is then applied to the atlas. A tissue/air susceptibility map can be obtained from each subject's structural MR using the atlas-based segmentation method described in Chapter 4. This prior can then be used in the following variational method:

$$\chi^* = \arg\min_{\chi} \lambda_1 \left| W\left(\Delta B - \frac{B_0}{3}\Box\chi\right)\right|_1 + \lambda_2 \left| M_0\left(B - K\chi\right)\right|_2^2 + \lambda_3 \left| M_0\left(\chi - \chi_A\right)\right|_2^2 \quad , \quad (5.11)$$

where B is the observed field, B_0 is the main field strength, χ is the unknown susceptibility map, χ_A is the atlas-based susceptibility prior, K is the kernel from the forward model, and λ_1, λ_2 and λ_3 are constants. The first term penalizes departures from Eq. 5.8, by enforcing agreement of high frequency phase effects, while removing low order bias fields. Following section 5.1.2, the L1 norm is used to promote sparse solutions. To prevent noise in the acquired field map from biasing the predicted χ values, the weighting factor W is set to $|\Delta B|$, where $|\cdot|$ denotes the absolute value.

Voxels in W that fall within 2σ are set to 0, where σ is the standard deviation of the signal in a noise region of the magnitude image. In addition, the L2 norm was also investigated and shown to be robust to noise, with negligible loss of high frequency structure in the estimated χ maps. In this case, W can be replaced by the brain mask, M_0.

In Chapter 2, we noted that certain susceptibility distributions in the brain (ie. those that are eigenfunctions of the kernel, K) produce fields that cannot be distinguished from low frequency biasfields using phase information alone, and therefore additional modeling in the form of priors or atlases is needed to resolve this ambiguity. In this method, term 3 penalizes large deviations from the susceptibility atlas. This discourages the estimation of artifactual susceptibility values in regions near tissue-air boundaries where the Laplacian may not be sufficient to eliminate the contribution of non-local sources and substantial signal loss corrupts the observed field. In term 2, M_0 enforces agreement of predicted and observed fields within the brain, but deviations in estimated susceptibility values outside the brain are not penalized by Term 3, allowing susceptibility values at the boundary to vary from the atlas-based prior to account for unmodeled external field sources (ie. shims). Although the method in [31] estimates boundary sources for biasfield removal, no prior information concerning external head or sinus geometry is included, making the method less robust to differences in implementation (ie. choice of stopping criteria), and subsequent susceptibility estimation cannot recover from imperfections in biasfield removal. In addition, the method in [31] may be prone to error when incomplete coverage of the brain is acquired or in cases where the magnitude prior does not share significant edges with the unknown susceptibility map (ie. tumor patients). The method in [98] utilizes a Laplacian-based pre-processing method to remove external fields, but does not provide a prior on susceptibility within the brain or modeling of internal air spaces, which may result in estimation of artifactual susceptibility distributions. Finally, solving the partial differential equation (PDE) in Eq. 5.4 using traditional PDE techniques would not allow priors such as χ_A to be incorporated into the estimation problem, which can be easily done using the variational approach. The optimization

in Eq. 5.11 was implemented in Matlab R2010a; given a voxel-based model of the object, the approximation described in Section 5.1.1 was applied when computing $\square\chi$, and the solution was obtained using standard conjugate gradient techniques.

Following estimation of the χ map, the mean susceptibility in each ROI (TH, CD, PT, and GP) from both hemispheres was calculated. The ROIs were manually identified by an expert as described in [91]. Mean susceptibility values in each ROI were plotted against the mean postmortem iron concentrations reported in [3]. SWI results were computed following [91, 117]. The FDRI was filtered using a Gaussian kernel with $\sigma = 2$ mm to compensate for a low signal-to-noise ratio (SNR) prior to visualization. SWI results with inverted contrast were computed by swapping the real and imaginary components for visualization purposes only.

5.2 Phantom Experiments

5.2.1 Data Acquisition

For validation, two phantoms were constructed using Magnevist (gadopentetate dimeglumine) solutions of 0.5, 1.0, 2.0, and 3.0 mM corresponding to susceptibility values of 0.15, 0.31, 0.62, and 0.94 ppm respectively. Samples were placed in NMR tubes 10 cm in length and 3.43 mm inner diameter, and the molar susceptibility of 0.027 cgs units/mol Gd was used for conversion [119]. In the first experiment, a 'rectangular phantom' was imaged: the 2.0 mM sample was placed horizontally in a rectangular tank, transverse to the B0 field. Phase maps of the tube's center slice previously acquired by [23] were obtained: 256 x 256 pixels, FOV = 180 mm, thickness = 7 mm, TR = 100 ms, TE = 5.0, 7.25 ms, and 10 averages. In the second experiment, a 'cylindrical' phantom was imaged: the tubes were separated by plastic disks and placed in a plastic cylinder 22.5 cm in length by 22 cm inner diameter and imaged using a 3D multi-echo GRE sequence: 128 x 128 pixels, 128 mm FOV, thickness = 3 mm, TR = 19 ms, TE = 6, 12 ms. Scanning was done on a 3T Siemens Trio MRI. B0 maps from both experiments were computed following phase unwrapping with

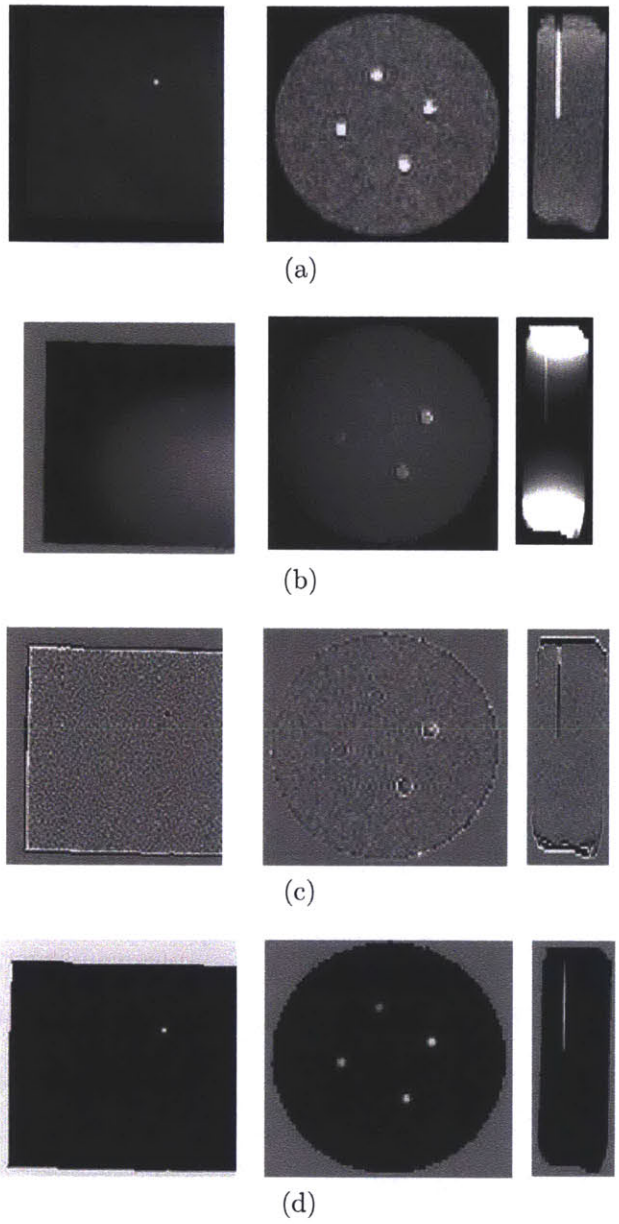

Figure 5-1: Phantom Experiments: Results of the Biasfield Removal and Susceptibility Estimation. Axial cross-sections of the magnitude data for the rectangular and cylindrical phantoms and a sagittal cross-section of the cylindrical phantom is shown in (a). The corresponding fieldmaps, which show substantial biasfields are shown in (b). Application of the Laplacian removes these external field artifacts (c). The final estimated susceptibility maps are shown in (d).

PRELUDE [58].

5.2.2 Results: K-Space Magnitude Prior on Phantom Data

Application of the Laplacian removes the substantial inhomogeneity effects in both phantoms as seen in Fig. 5-1. In the rectangular phantom, mean estimated susceptibility values for the water region and Gd tube were -9.049 and 0.6273 ppm with actual values of -9.05 and 0.6270 ppm. In the cylindrical phantom, the reconstructed susceptibility map allowed tubes that differed by less than 1 ppm to be clearly identified and reasonable accuracy was obtained in the presence of significant noise and bias due to external field effects.

5.3 In-vivo Experiments

5.3.1 Data Acquisition

We obtained structural MRI and phase maps for 12 elderly subjects (74.4 $\pm$ 7.6 years) and 11 younger adults (24 $\pm$ 2.5 years) previously acquired by [91] on a 1.5 T GE Signa with 62 slices, 2.5 mm thick: 3D SPGR for structural imaging, TR = 28 ms, TE = 10ms, FA = 30°, acquisition matrix = 256 x 256, 24 cm FOV; Susceptibility-weighted 3D SPGR with flow compensation for SWI and phase map reconstruction, TR = 58 ms, TE = 40 ms, FA = 15°, acquisition matrix = 512 x 256, 24 cm FOV [91, 46, 44]. High resolution phase maps were reconstructed from the real and imaginary components of the flow-compensated SWI-SPGR after phase unwrapping with PRELUDE [58]. FDRI maps collected at 1.5 and 3.0 Tesla were calculated from the following T2-weighted sequences with 62 slices, 2.5 mm thick: multi-shot Echo Planar Spin Echo(EPSE), TR = 6000 ms, TE = 17 ms, FA = 90°, 256 x 192 inplane, FOV = 24 cm; multi-shot EPSE, TR = 6000 ms, TE = 60 ms, FA = 90°, 256 x 192 inplane, FOV = 24cm; 3D SPGR was also obtained at both field strengths for registration [91]. Structural and FDRI images were rigidly registered to the same subject's SWI magnitude image.

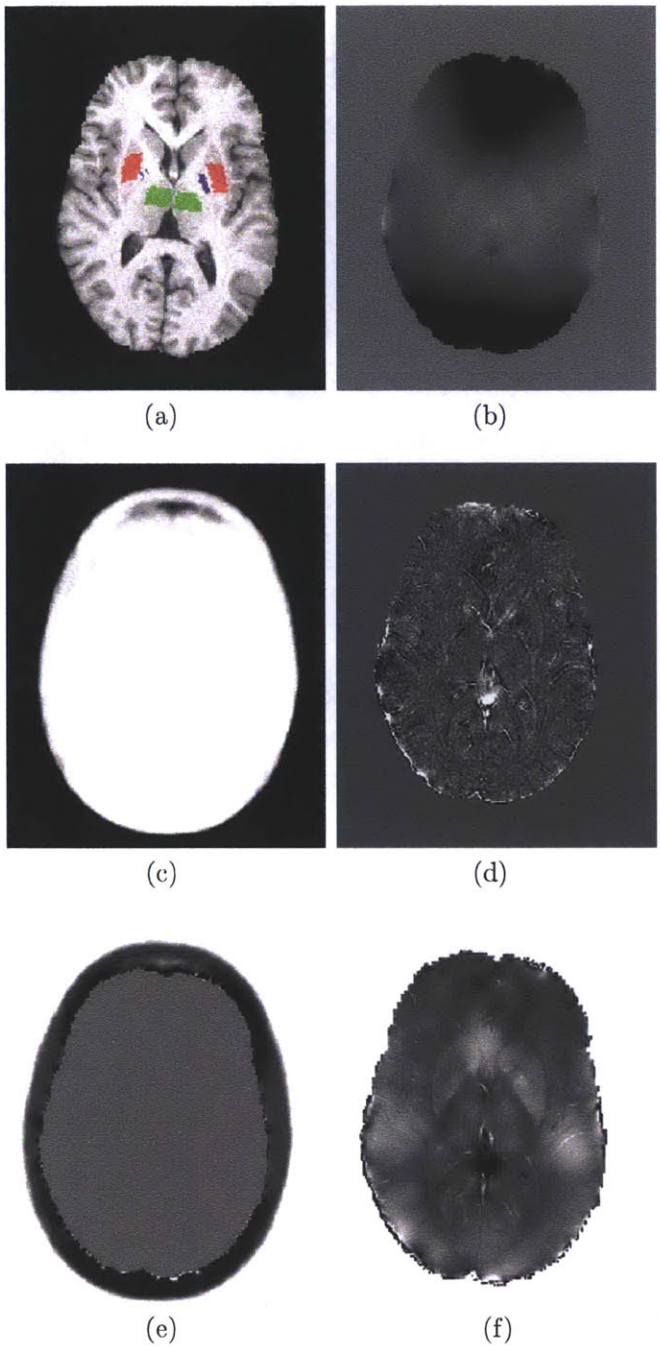

Figure 5-2: ASM Results for a representative young subject. The first row shows the T1-weighted structural image (a) including the PT (red), GP (blue), and TH (green), and the fieldmap (b), which shows substantial inhomogeneity. Row 2 shows the susceptibility atlas (c), in which voxels take continuous values between [0,1] corresponding to susceptibility values between χ_{air} and χ_{tissue}. Taking the Laplacian of the fieldmap successfully eliminates biasfields (d). Estimates of external susceptibility sources are shown in (e). The estimated susceptibility map (f) shares similar high frequency structure with the Laplacian of the observed field while low frequency structure is preserved by enforcing agreement with the atlas-based prior and observed field. The intensity scale of the estimated susceptibility map is $[-9.055, -9.04]$ ppm.

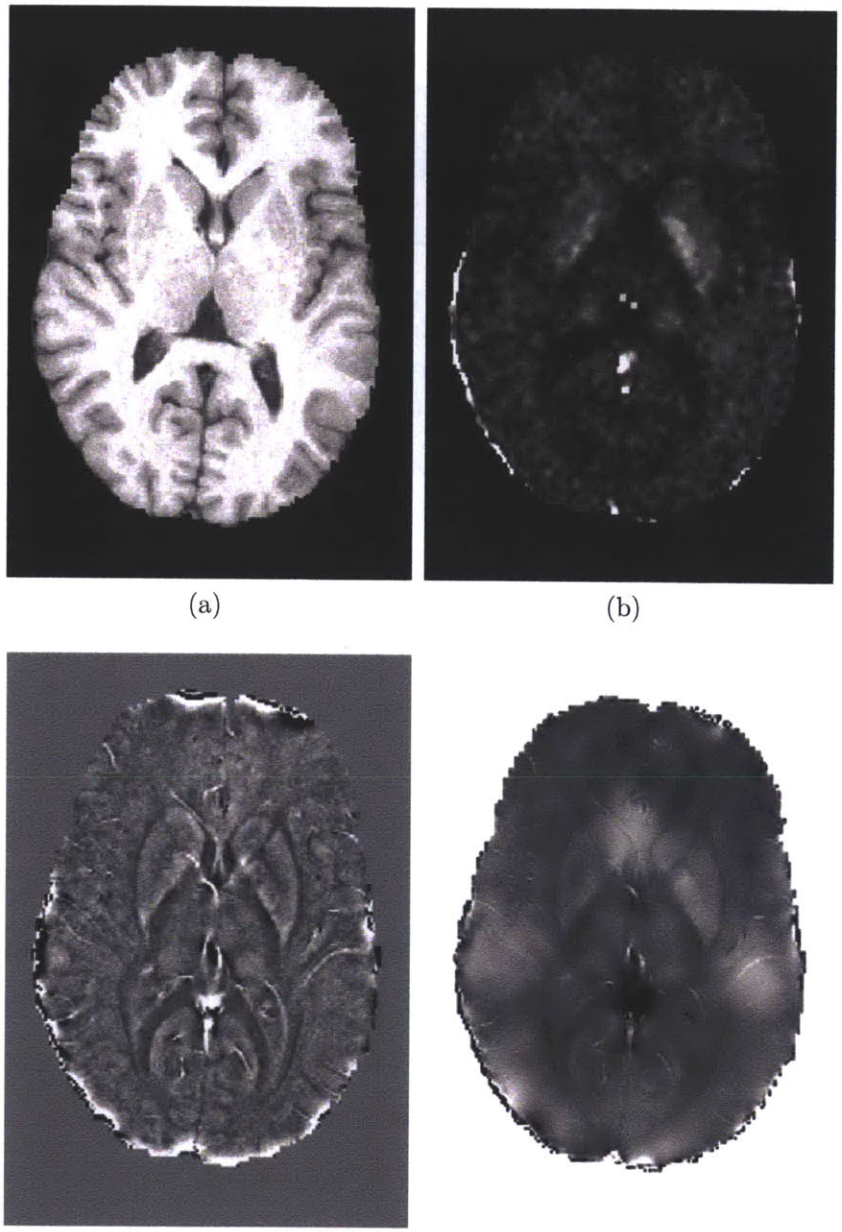

Figure 5-3: Comparison of ASM to FDRI and SWI. T1 structural image (a), FDRI (b), SWI (c) and ASM (d) results are shown for a young subject. The FDRI shows strong constrast between ROIs and adjacent tissue, but less high frequency structure than the SWI. The SWI retains high frequency phase effects, but indiscriminately removes low order fields from both internal and external sources, resulting in artifactual low frequency structure. ASM accurately preserves the high frequency structure seen in SWI while showing improved estimation of low order susceptibility distributions. The intensity scale of the estimated susceptibility map is $[-9.055, -9.04]$ ppm.

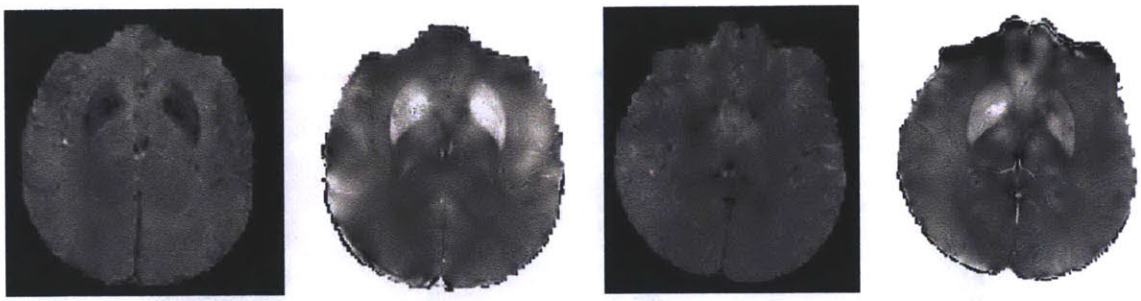

(a) (b) (c) (d)

Figure 5-4: ASM Results in Elderly Subjects. ASM results for two elderly subjects are shown above in (b) and (d). The corresponding magnitude images are shown in (a) and (c). The intensity scale of the estimated susceptibility maps is $[-9.055, -9.04]$ ppm.

5.3.2 Results: ASM

ASM results for a representative young subject are shown in Fig. 5-2. Row 1 shows the T1-weighted structural image (Fig. 5-2a) with regions of interest corresponding to the PT (red), GP (blue), and TH(green), and the acquired fieldmap (Fig. 5-2b). Applying the Laplacian to the fieldmap removes substantial B_0 inhomogeneities that bias the observed field (Fig. 5-2d). The susceptibility atlas is shown in Fig. 5-2c and estimated external sources are shown in Fig. 5-2e. The estimated susceptibility map (Fig. 5-2f) shares high frequency structure with the Laplacian of the observed field, while low frequency structure is preserved by enforcing agreement with additional information provided by the atlas-based prior and observed field.

Fig. 5-3 shows structural MRI and results from FDRI (Fig. 5-3b), SWI (Fig. 5-3c), and ASM for a representative young subject (Fig. 5-3d). The FDRI shows strong constrast between the ROIs and surrounding tissue, but less high frequency structure than the SWI. The SWI retains high frequency phase effects, but indiscriminately removes low order fields from both internal and external sources, resulting in artifactual low frequency structure. The ASM method accurately preserves the high frequency phase effects seen in SWI while showing improved estimation of low order susceptibility distributions. In addition, ASM provides direct estimates of susceptibility values rather than filtered phase proxies for susceptibility. ASM shows similar results for

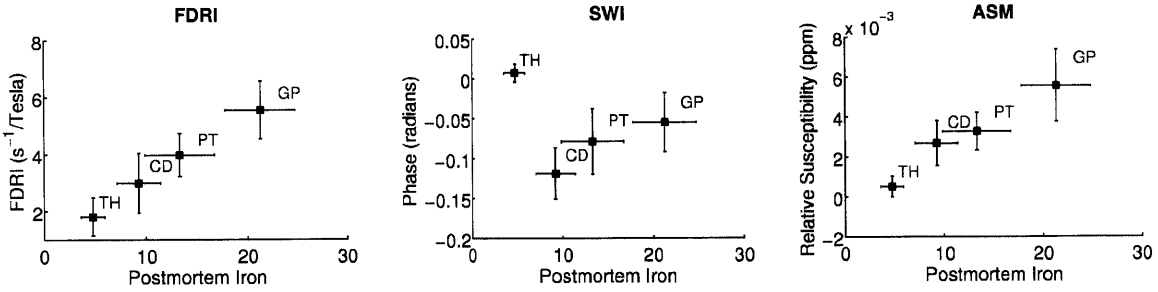

(a) (b) (c)

Figure 5-5: Quantitative ASM Results for Elderly Subjects. The Mean±SD iron concentration (mg/100g fresh weight) in each ROI determined from postmortem analysis [3] is plotted on the x-axis. The y-axes show the Mean±SD FDRI (s^{-1}/Tesla) in (a), Mean±SD SWI (radians) in (b), and Mean±SD ASM relative susceptibility (ppm) in (c). Mean susceptibility values from ASM show a high correlation with the postmortem data, which agrees well with FDRI results and shows improvement over SWI values previously reported for the same data [91].

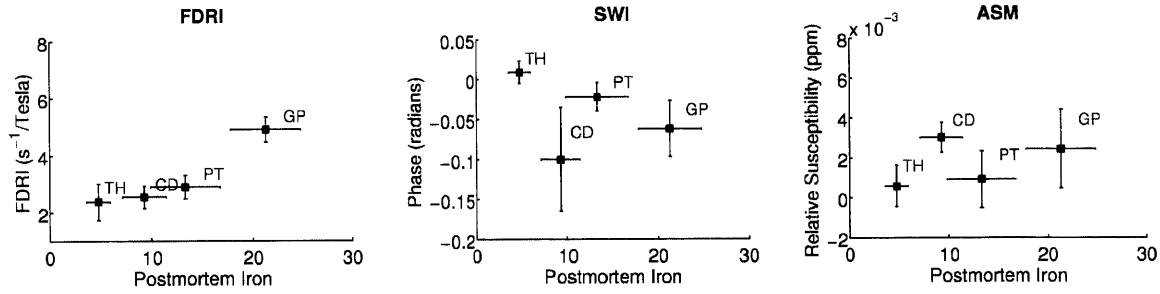

(a) (b) (c)

Figure 5-6: Quantitative ASM Results for Young Subjects. The Mean±SD iron concentration (mg/100g fresh weight) in each ROI determined from postmortem analysis [3] is plotted on the x-axis. The y-axes show the Mean±SD FDRI (s^{-1}/Tesla) in (a), Mean±SD SWI (radians) in (b), and Mean±SD ASM relative susceptibility (ppm) in (c). Mean susceptibility values from ASM show a linear correlation with postmortem data, which is better than SWI, but not as strong as FDRI results reported for the same data [91].

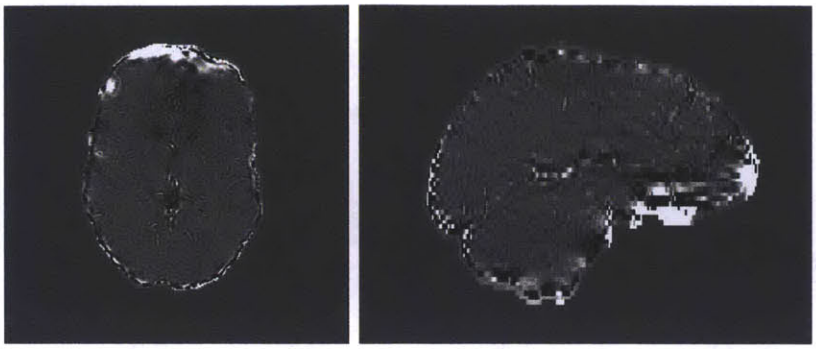

(a) (b)

Figure 5-7: Results of Susceptibility Estimation using Terms 1 and 3. Removing the fieldmap agreement term from the ASM objective function ($\lambda_2 = 0$ in Eq. 5.11) results in the estimation of artifactual susceptibility values and a lack of low-frequency structure especially in brain regions near tissue/air interfaces.

two elderly subjects (Fig. 5-4).

Quantitative results from ASM and previously reported results from FDRI and SWI for the same elderly subjects are shown in Fig. 5-5. The mean susceptibility values (relative to χ_{tissue}) in each ROI from all elderly subjects are plotted against the corresponding iron concentrations from postmortem analysis (only the mean and SD in each ROI was reported in [3]). ASM shows a high correlation with postmortem values, which is comparable to that seen in FDRI and substantially better than the correlation between phase and iron concentration obtained with SWI. In addition, for the structures that we analyzed, ASM results compare favorably to the correlation between postmortem iron and susceptibility estimates in corresponding ROIs computed from multi-angle acquisitions [98]. Quantitative ASM results for the young subjects (Fig. 5-6) also show a linear correlation with postmortem iron measurements, which shows improvement over SWI, but is not as strong as the FDRI results for this group.

5.4 ASM and the Dipole Field Assumption

The ASM approach described in the previous section addresses some of the limitations of previous QSM techniques. These include sequential susceptibility estimation, which may result in the calculation of artifactual susceptibility distributions in the

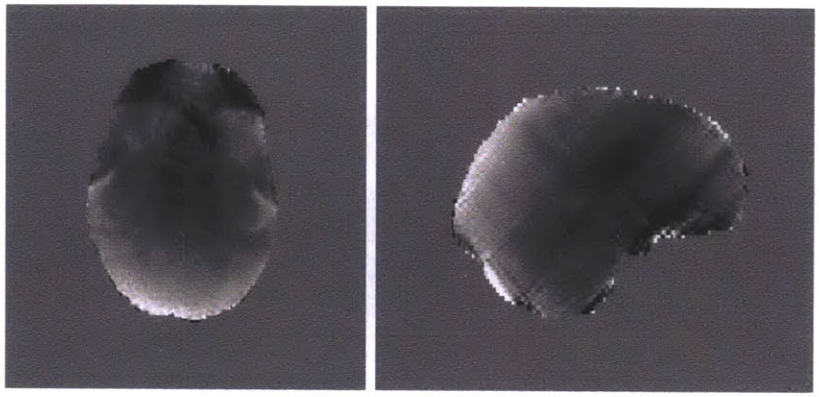

(a) (b)

Figure 5-8: Results of Susceptibility Estimation using Terms 1 and 2. Removing the atlas term from the ASM objective function ($\lambda_3 = 0$ in Eq. 5.11) results in substantial streaking artifacts in the brain due to the effects of confounding biasfields from external sources.

brain or mis-estimation of external susceptibility distributions, and disagreement between estimated χ values and postmortem iron measurements, even in the case of multi-angle acquisitions. The ASM method, however, also has important limitations related to each term in Eq. 5.11 that merit further discussion. First, any low order fields produced by internal susceptibility distributions will be eliminated by the Laplacian, resulting in a loss of information. This limitation is mitigated by incorporating term two into the model, which enforces agreement between the predicted field and the total field, but is compromised by the presence of confounding biasfields in B. The effect of the second term can be shown by comparing the results in Fig. 5-2 to those obtained using only terms one and three ($\lambda_2 = 0$) as illustrated in Fig. 5-7. The latter shows artifactual χ maps that lack low frequency structure. In addition, any Laplacian-based biasfield elimination assumes that all external sources produce low order biasfields in the brain. This is a sound assumption for fields produced by mis-set shim or remote sources (ie. the lungs), but may not be entirely valid near tissue/air interfaces. This assumption is relaxed, however, by use of the atlas to model the anatomical sources surrounding the brain. The second important limitation is that a strong atlas prior is needed to prevent the estimation of artifactual internal χ distributions. The result of removing the atlas from the model ($\lambda_3 = 0$) results in

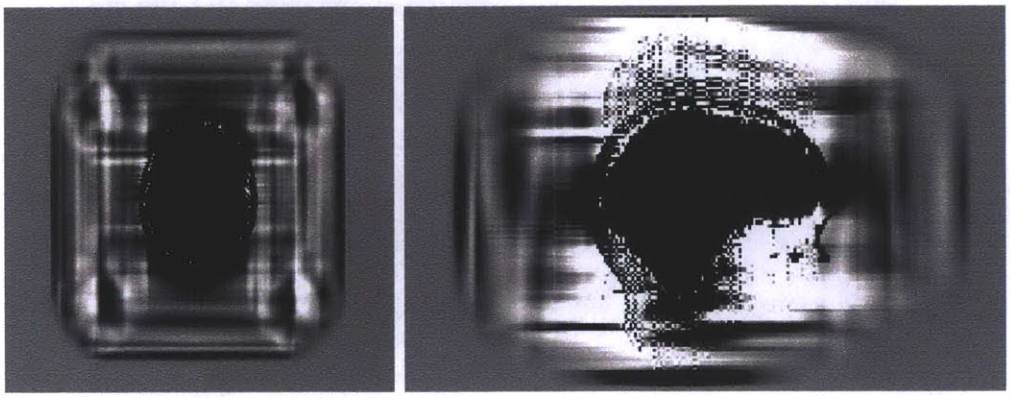

(a) (b)

Figure 5-9: Estimated External Sources. The estimated external sources are shown in axial (a) and sagittal (b) views.

the severe artifacts shown in Fig. 5-8. The atlas prior, however, may overly penalize estimation of the sources of interest in the brain, which would not affect the slope of the quantitative results shown in Fig. 5-5 and Fig. 5-6, but may account for an overall under-estimation of their absolute values. Given these limitations, we describe a modification to ASM that includes additional modeling of the external source distribution, and is based on the combined strengths of both forward models described in Chapter 2.

Recall from Chapter 2 that the k-space formulation of the forward model assumes the measured field is equivalent to a superposition of dipole fields, which is obtained by truncating an expansion of the magnetic induction, B. An expression for the Fourier transform of B can then be obtained with minimal additional assumptions, and is given by the product of the dipole kernel in Fourier space, and the Fourier transform of the susceptibility distribution. In practice, the kernel is computed in Fourier space over the finite range of spatial frequencies acquired during fieldmap (or phasemap) acquisition. Its finite extent in Fourier space implies that the susceptibility distribution is not necessarily finite in image space; Marques and Bowtell remark that care must be taken when computing 3D-FFTs to avoid problems due to the finite extent of the real and k-space domains considered during implementation. More specifically, they point out that χ must be defined over a much larger field of view

in image space than the actual region of interest [83]. Jenkinson et al, point out that spatial formulations of the forward model are advantageous in this respect since they can ensure the susceptibility distribution is of finite spatial extent [62]. This suggests that the k-space formulation of the forward model may be more appropriate for estimation of external susceptibility sources that create biasfields in the brain, than it is for internal ones, which are of finite extent.

The spatial formulation of the forward model consists of the addition of a local linear term that is proportional to the susceptibility and the convolution of the susceptibility distribution with a kernel computed in image space, which is based on the Green's function of the Laplacian. The convolution is implemented via 3D-FFTs, but the model assumes the observed fieldmap can be calculated from a voxel-based susceptibility model of finite extent. This assumption is more consistent with estimating internal susceptibility sources. The accuracy of this forward model is sensitive to spatial resolution, so that searching over a large enough field of view to accurately model the external sources at high voxel resolutions incurs a higher computational cost (the number of computations for N voxels is $O(N \log N)$) [62]. The errors associated with neglecting the higher order terms in the perturbation formulation are small (0.0001 ppm) compared to the errors due to the voxel-based modeling, but this can be reduced by solving for internal sources over a high resolution FOV surrounding the brain. In this method we exploit the strengths of both approaches and model the biasfield as the superposition of low order spherical harmonics that satisfy the Laplace equation, and higher order fields produced by a distribution of external dipoles. The new ASM estimator is:

$$\chi^* = \arg\min_{\chi} \lambda_1 \left| W\left(\Delta B - \frac{B_0}{3}\Box\chi\right)\right|_1 + \lambda_2 \left| M_0\left(B - \left(K_s\chi + B_{ext}\right)\right)\right|_2^2 + \lambda_3 \left| M_0^C \chi\right|_2^2 \tag{5.12}$$

$$\text{where} \quad B_{ext} = K_f \chi_{ext}^* \quad , \tag{5.13}$$

where W is the weighting factor from Eq. 5.11, B is the acquired fieldmap, B_0

is the main field strength, M_0 is a mask of the brain, and K_s is the kernel from Eq. 5.11 corresponding to the spatial formulation of the forward field model. M_0^C is the complement of M_0, representing the region outside the brain. χ^*_{ext} is calculated by:

$$\chi^*_{ext} = \arg\min_{\chi} |M(B - K_f(M_0^C\chi))|_2^2 \quad \text{where} \quad \chi_i = \chi_A \quad , \tag{5.14}$$

where χ_i is the initial estimate of the susceptibility values, which is equal to the tissue/air atlas, χ_A; M is the normalized magnitude image of the brain, B is the acquired fieldmap, and K_f is the kernel from the k-space formulation of the forward model.

In Eq. 5.14 the external sources are initialized to the tissue/air atlas and a search over χ values is performed to find the values which optimize agreement between the predicted and measured field in the brain. The field due to the optimal external sources is computed and used in the second term of Eq. 5.12. By including this estimate of the field from external sources in Eq. 5.12, estimating internal χ values that are eigenfunctions of K_s and artifacts of the biasfield contained in B is discouraged. Additional external sources can be estimated to recover from imperfections in the initial estimate, but are penalized with a strength determined by λ_3. By combining the forward models with the atlas and laplacian-based modeling, a revised approach that successfully addresses the previous limitations of ASM is obtained. We will refer to this method as 'ASM-2K' since it incorporates both kernels.

Results of the external source estimation are shown in Fig. 5-9. Sources resembling anatomy outside the brain as well as more remote distributions can be seen. Results of ASM-2K for a representative young subject (Fig. 5-10d) show significantly reduced background field artifacts relative to the ASM result from Fig. 5-3d, while retaining the low frequency structure that is absent in the SWI (Fig. 5-3c). Results for two elderly subjects are shown in Fig. 5-11 and show similar improvement relative to those in Fig. 5-4. The quantitative results in elderly (Fig. 5-12) and young (Fig. 5-13) subjects show strong correlation with postmortem iron values in the re-

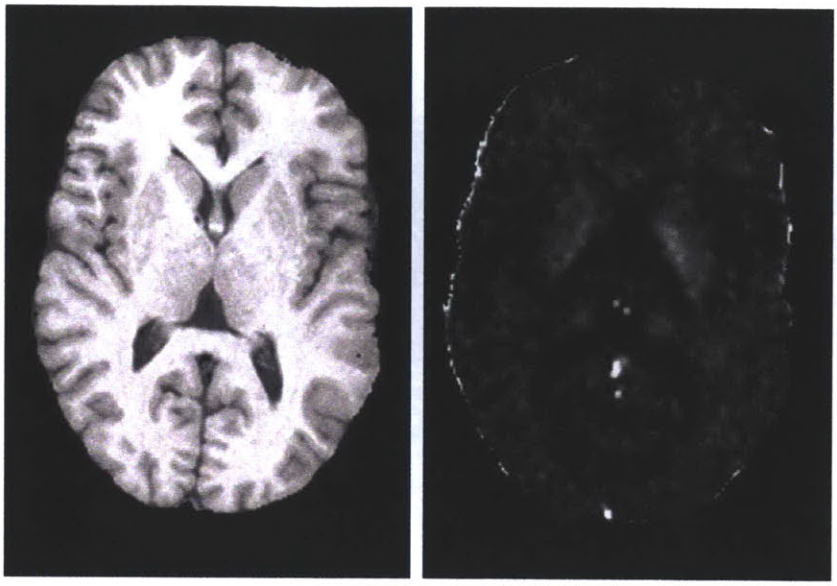

(a)

(b)

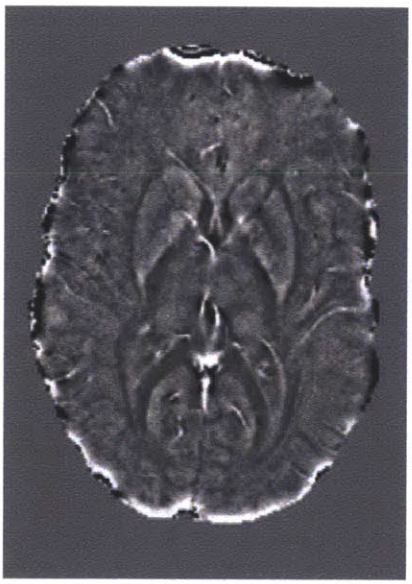

(c)

(d)

Figure 5-10: Comparison of ASM-2K to FDRI and SWI. T1 structural image (a), FDRI (b), SWI (c) and ASM-2K (d) results are shown for a young subject. The FDRI shows strong constrast between ROIs and adjacent tissue, but less high frequency structure than the SWI. The SWI retains high frequency phase effects, but indiscriminately removes low order fields from both internal and external sources, resulting in artifactual low frequency structure. The relative susceptibility map estimated with ASM-2K accurately preserves the high frequency structure seen in SWI while showing improved estimation of low order susceptibility distributions. In addition biasfield removal is substantially improved relative to previous results in Fig. 5-3. The intensity scale of the estimated relative susceptibility map is ± 0.2 ppm.

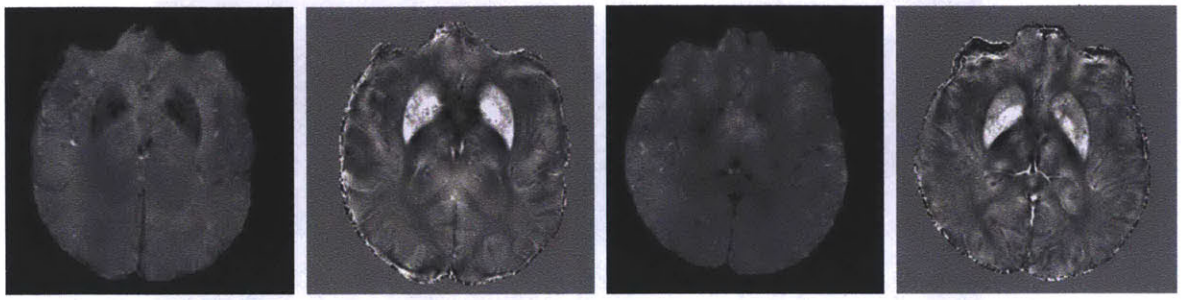

(a) (b) (c) (d)

Figure 5-11: Results of ASM-2K in Elderly Subjects. Estimated relative susceptibility maps for two elderly subjects using ASM-2K are shown above in (b) and (d). Biasfields are effectively removed showing improvement over results from Fig. 5-4. The corresponding magnitude images are shown in (a) and (c). The intensity scale of the estimated relative susceptibility maps is ± 0.2 ppm.

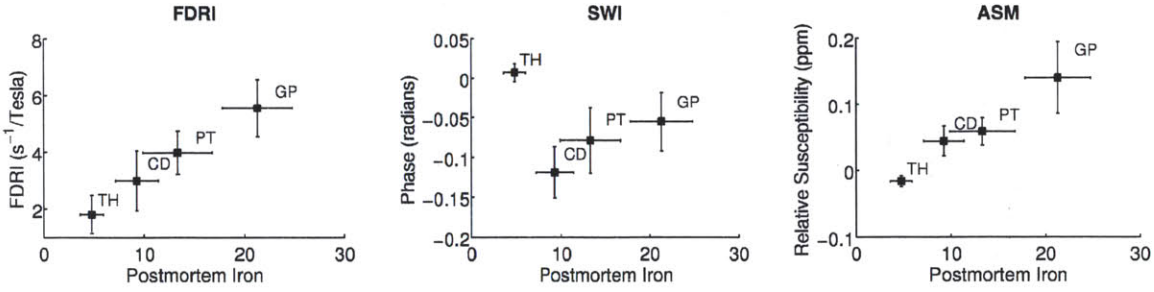

(a) (b) (c)

Figure 5-12: ASM-2K Results for Elderly Subjects. The Mean±SD iron concentration (mg/100g fresh weight) in each ROI determined from postmortem analysis [3] is plotted on the x-axis. The y-axes show the Mean±SD FDRI (s^{-1}/Tesla) in (a), Mean±SD SWI (radians) in (b), and Mean±SD ASM-2K relative susceptibility (ppm) in (c). Mean susceptibility values from ASM-2K show a high correlation with the postmortem data, which agrees well with previous results from FDRI and shows improvement over SWI values reported for the same data [91].

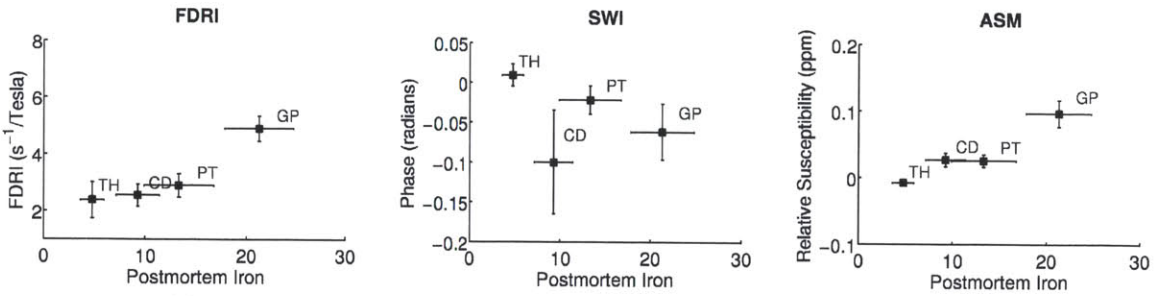

(a) (b) (c)

Figure 5-13: ASM-2K Results for Young Subjects. The Mean±SD iron concentration (mg/100g fresh weight) in each ROI determined from postmortem analysis [3] is plotted on the x-axis. The y-axes show the Mean±SD FDRI (s^{-1}/Tesla) in (a), Mean±SD SWI (radians) in (b), and Mean±SD ASM-2K relative susceptibility (ppm) in (c). Mean susceptibility values from ASM-2K show a high correlation with the postmortem data, which agrees well with previous results from FDRI and shows improvement over SWI values reported for the same data [91]. In addition these results show substantial improvement over ASM results reported previously in Fig. 5-6.

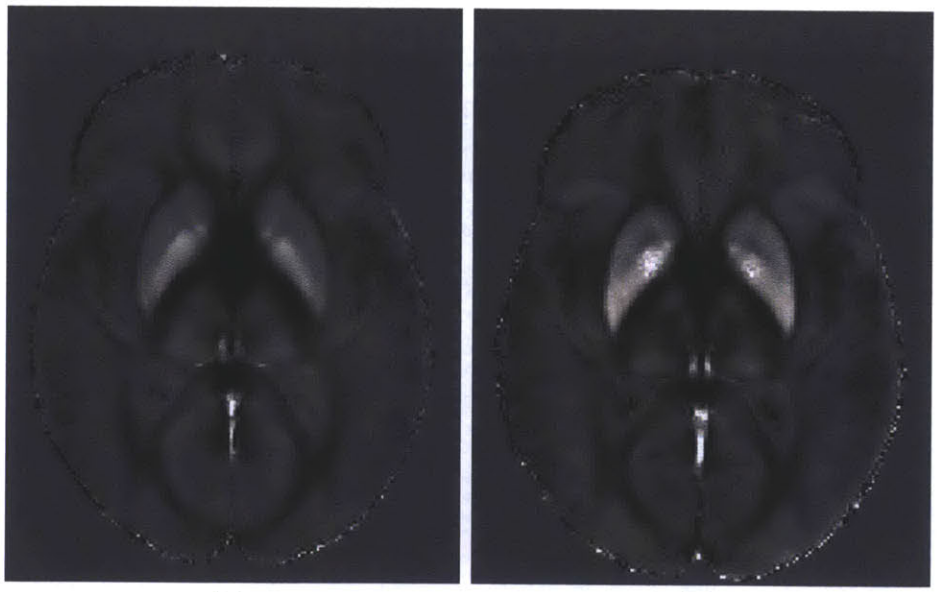

(a) (b)

Figure 5-14: Group Averages. Averages of the ASM-2K results for young (a) and elderly (b) subjects show an age dependent increase in estimated susceptibility values in sub-cortical regions known to accumulate iron in normal aging. The intensity scale of the estimated relative susceptibility maps is $[-0.1, 0.25]$ ppm.

gions of interest. In addition, ROI values using ASM-2K are in better agreement with previously published values [98], than those from Fig. 5-5 and Fig. 5-6. Finally, ASM-2K results were co-registered to standard space according to [91] and group averages were computed. Mean ASM-2K results show increased contrast in sub-cortical structures in elderly subjects, supporting an age-dependent increase in iron in these regions (Fig. 5-14).

5.5 Conclusions

Quantifying magnetic susceptibility in the brain from the phase of the MR signal provides a non-invasive method for measuring the accumulation of iron believed to occur with aging and neurodegenerative disease. Phase observations from local susceptibility distributions, however, are corrupted by external biasfields, which may be identical in form to fields from the sources of interest. Furthermore, only limited observations of the phase are available and the inversion is ill-posed. In this chapter, we described a variational approach to susceptibility estimation that incorporates a tissue/air atlas to resolve ambiguity in the forward model, while eliminating additional biasfields through application of the Laplacian. Results showed qualitative improvement over FDRI and SWI, two methods commonly used to infer underlying susceptibility values, and quantitative susceptibility estimates showed better correlation with postmortem iron concentrations than competing methods, including those obtained using multi-angle acquisitions.

Chapter 6

Conclusions and Future Directions

6.1 Future Directions

Given the promising results of our susceptibility-based distortion correction and quantitative susceptibility mapping techniques developed in this dissertation, we now consider future extensions and applications of this work. In this section, we discuss a few of these possibilities, elaborate on our preliminary work in applying ASM to calculate susceptibility time-series from perfusion MRI, and conclude with a synopsis of the main contributions of this thesis.

6.1.1 Calculation of Synthetic Fieldmaps for Correction of Motion and Distortion in EPI Data

Head motion during EPI acquisition is known to present a serious confound to fMRI analysis [64, 53, 1]. Small movements over the course of a study can lead to large signal changes that obscure the subtle task-related differences that are being studied [64]. To correct for this effect, most researchers co-register all EPI volumes using 6 parameter (rigid) or 12 parameter (affine) transformations prior to analysis. While these methods improve overall alignment, they cannot correct for local, non-linear distortions caused by B_0 field inhomogeneity. To unwarp the images, many researchers use a single acquired fieldmap to compute the deformation field ('pixel-shift map') and

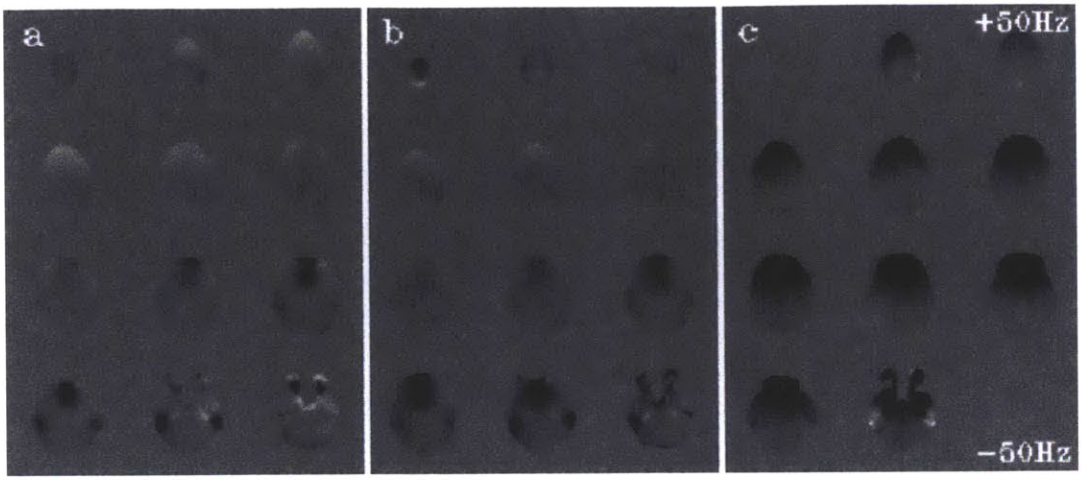

Figure 6-1: Effects of Motion on Acquired Fieldmaps. (A) A fieldmap collected from a subject at an arbitrary position. (B) A fieldmap collected after a 5° rotation to a second position. (C) A fieldmap difference image following registration of position 2 data to position 1 data and subtraction. Field differences of up to 50 Hz can be seen (reprinted, with permission, from [64]).

apply this to each motion-corrected EPI volume or simply compute statistics in the warped frame and then unwarp the statistical maps prior to identifying activations. This assumes, however, that the deformation field is constant throughout the times-series, which is not true if motion has occured, since B_0 field inhomogeneity is a function of object position. Previous work has shown that fieldmaps acquired before and after head rotations of 5° show field differences of up to 50 Hz, corresponding to pixel shifts of $2-3$ voxels (Fig. 6-1) [64]. Although this would be an unusual amount of motion for a typical fMRI experiment, smaller movements would increase the noise in the time-series. Also, larger motions are more common in patients and other less compliant subjects and smaller motions become an increasingly significant problem as field strength increases. Therefore, more accurate unwarping of the EPI data may be possible if the time-varying deviation in the fieldmap is known.

Accurate correction of motion and distortion in EPI data is possible if synthetic fieldmaps can be computed from a susceptibility model at each time-point. One approach to this problem would be to estimate the orientation of each EPI volume using standard motion-correction algorithms; segment the structural MR as described in Chapter 4 to obtain a tissue/air susceptibility model and produce multiple copies

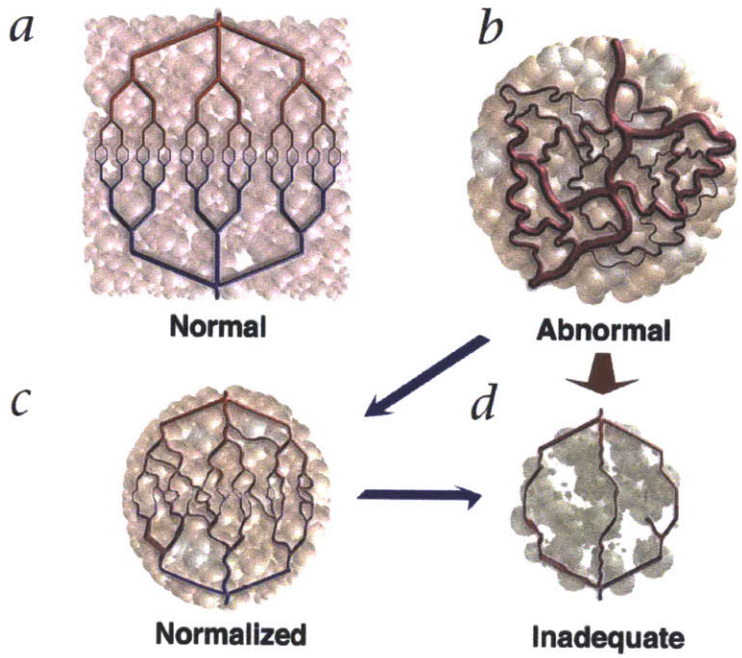

Figure 6-2: Proposed Theory of Vascular Normalization in Response to Anti-angiogenic Therapy. Tumor growth results in structurally and functionally abnormal vasculature (b) with increased vessel permeability, diameter, and tortuosity relative to normal tissue (a). This compromises the delivery of therapeutics and nutrients. Anti-angiogenic therapies may initially normalize tumor vasculature (c), improving drug delivery and reducing tumor growth, but prolonged, aggressive therapy may prune away vessels, causing resistance to further treatment (d) (reprinted, with permission, from [55]).

of this image at orientations corresponding to each of the EPI volumes. An initial estimate of the synthetic fieldmap could then be computed from each susceptibility map by applying the forward model. Unknown shim parameters and a final time-series of synthetic fieldmaps could be computed using the registration algorithm from Chapter 3. Finally, the fieldmaps could be applied to unwarp the EPI data, and existing registration algorithms such as FLIRT [60] could be used to motion-correct the unwarped EPI time-series.

A potential disadvantage of this approach is that it requires running the forward model once for each volume, which may be time-consuming for high resolution susceptibility models and long EPI time-series. The speed of the initial fieldmap estimation step could be improved by computing the x, y, and z components of the perturbing field produced from applying a $B^{(0)}$ field along either the x, y, or z direction. The re-

sulting basis set of nine synthetic fieldmaps can be computed using the forward model and combined with estimated rotation parameters of each EPI volume to compute a synthetic fieldmap for each orientation [62]. This requires only nine forward field calculations as opposed to one for each time-point.

6.1.2 Atlas-based Susceptibility Mapping of Gadolinium Perfusion and Vessel Morphology Following Anti-angiogenic Therapy

Dynamic contrast-enhanced susceptibility-weighted (DCS) perfusion MRI uses rapid EPI sequences to allow maps of the cerebral microcirculation to be reconstructed following injection of a contrast agent. Maps of cerebral blood volume (CBV), cerebral blood flow (CBF), mean transit time (MTT), and other paramters can be derived from the perfusion time-series and applied to assess pathologies affecting the microcirculation. Clinically, CBV maps are widely used to assess intracranial mass lesions and angiogenesis (the development of new blood vessels) [24].

More than four decades ago, Folkman et al. proposed that tumors rely on angiogenesis in order to grow beyond a few cubic millimeters [42, 41, 32]. Numerous studies have since supported this theory, including one by Burger et al., who found vascular proliferation to be the single differentiating characteristic between short and long term survival for patients suffering from malignant astrocytic gliomas, an aggressive form of brain cancer [21]. Since tumors are dependent on the formation of new blood vessels for growth and metastasis, anti-angiogenic drugs that prevent such growth by starving tumor cells of necessary oxygen and nutrients, should reduce morbidity and mortality [40]. Clinically, however, the results of anti-angiogenic drugs have been somewhat disappointing. When administered as single agents, they have produced only modest objective responses in clinical trials [122, 28] and overall they have not yielded long-term survival benefits [93, 56]. When given in combination with chemotherapy, however, the anti-angiogenic drug bevacizumab (trade name Avastin) produced an unprecedented increase in survival (5 months) in colorectal can-

cer patients [52]; (bevacizumab is an antibody targeted against the potent angiogenic molecule vascular endothelial growth factor (VEGF)) [56]. While the results in [52] are encouraging, it's counterintuitive that combined anti-angiogenic and chemotherapy would increase survival. Instead, one would expect that drugs designed to destroy tumor vasculature would reduce the efficacy of chemotherapeutics that rely on transport through intact vessels to reach tumor cells. Other studies, for example, have shown that anti-angiogenic therapy can compromise drug delivery to tumors [81] and the outcome of radiation therapy [86, 38].

Apart from increased vascularity, tumor vessels also display abnormal morphological and physiological properties; they are disordered, tortuous, and permeable structures with increased diameters [32]. Given these abnormal characteristics and the paradox presented by the results of combined therapy, R. Jain proposed the theory of vascular normalization: moderate doses of anti-angiogenic agents cause normalization of tumor vasculature, resulting in more efficient delivery of drugs and oxygen to targeted cancer cells [55]. In contrast, high or prolonged doses of anti-angiogenic drugs may destroy vessels sufficiently to impair drug delivery or radiation therapy, without entirely starving tumors of blood supply (Fig. 6-2). The combination of an anti-angiogenic agent and a cytotoxic drug, however, would increase the efficacy of the chemotherapeutic by improving delivery through a normalized vasculature. Characterizing changes in the morphological and physical properties of tumor vessels in response to anti-angiogenic drugs is critical for further validation of this theory. It is also essential for optimizing dosing and timing of combination therapy. Characterizing vessel morphology, however, is an arduous task that requires a biopsy followed by histology. In addition to being invasive, biopsies suffer from sampling errors and may not adequately capture the heterogeneity of tumor vasculature. Imaging techniques such as PET, perfusion MRI, and contrast-enhanced CT can provide measures of CBV and CBF, which provide an indication of overall vascularity, but tumor blood flow is highly heterogeneous. It is not the total flow or volume, but the distribution that is of interest [56]. In addition, these methods do not provide information about vessel permeability, structure, or shape.

There have been several attempts to characterize vessel morphology in more detail using MRI [32, 111, 109, 107, 108]. Dennie et al. showed that average vessel diameter within a voxel or ROI is proportional to $\Delta R2^*/\Delta R2$, where relaxation rates were computed from Monte Carlo simulations of the MRI signal [32]. In an animal study, they computed this metric from the MR signal before and after administration of a constrast agent and results agreed well with simulations based on vessel diameters obtained from histology. The vasculature in the simulations was modeled as an array of randomly oriented, infinite, and impermeable cylinders. In-vivo, however, tumor vessels are known to be highly permeable, which may weaken the correlation between $\Delta R2^*/\Delta R2$ and vessel diameter. In animal studies, a large contrast agent known as MION ($\approx$ 40 nm) can be used to ensure vessels are impermeable to the agent [32], but human studies are restricted to approved agents such as Gadolinium Diethylenetriamine Penta-acetic Acid (Gd-DTPA), which is prone to leakage. Thus, if $\Delta R2^*/\Delta R2$ were used to investigate vascular normalization in humans, reduced signal attenuation after therapy could be falsely attributed to a reduction in vessel diameter, when it might be due simply to leakage from abnormal tumor vasculature. Other studies have tried to measure vessel permeability (K^{trans}) from dynamic contrast enhanced (DCE) MRI [109, 107, 108], but these require the use of an accurate arterial input function (AIF) to properly model the tracer kinetics and extract permeability parameters, which can be difficult to obtain in practice [37].

Quantitative susceptibility mapping may provide a new means for investigating vascular normalization by providing quantitative estimates of contrast-agent induced susceptibility differences. By quantifying susceptibility directly, QSM would avoid many of the limitations of methods based on measurements of $\Delta R2$, $\Delta R2^*$, and K^{trans}. First, unlike the method of Dennie et al., QSM does not assume vessel impermeability and so inferences about vessel diameter drawn from susceptibility maps would not be confounded by contrast agent leakage from the vasculature. In addition, quantitative susceptibility maps reflect a local property of the tissue as opposed to $R2$ and $R2^*$ which are a function of magnetic field perturbations that can extend over larger distances. Second, QSM would not require estimation of the AIF,

which complicates calculation of accurate K^{trans} values. If vascular normalization does occur post therapy, we might expect this to be reflected in QSM results in several ways. Since normalization would reduce the total vascular space and permeability of tumor vessels, we would expect susceptibility values in these voxels to be reduced, as the contrast agent occupies a smaller fraction of the space per voxel and experiences more normal flow (less leakage). Second, as tumor vessels normalize and the average diameter decreases, the velocity of flow should increase, resulting in a more peaked time-course of the susceptibility values as the constrast agent is able to clear the tumor vasculature more quickly. Finally, if there is less leakage, we would expect susceptibility values in tumor voxels at the end of the perfusion study to be closer to their baseline values prior to injection.

To investigate whether quantitative susceptibility mapping can provide insight into vessel morphology, DSC data from 16 patients was acquired on a Siemens 3T Trio magnet at Massachusetts General Hospital using Gd-DTPA as the contrast agent. Magnitude and phase data from EPI gradient echo scans was obtained: TE = 31 ms, TR = 1.5 sec, FA = 80°, 100 volumes, 12 slices, thickness = 6.5 mm, voxel size = 1.2×1.2, matrix = 160×160. Patients were scanned both before and after receiving combined anti-angiogenic therapy and chemotherapy. The data was preprocessed: each phase volume was unwrapped using PRELUDE [58]; The MNI152T1 atlas in standard space was registered to the first volume of the magnitude data using 12 degrees of freedom and normalized correlation ratio as the cost function. The resulting transform was then applied to the tissue/air atlas. An initial estimate of the external susceptibility sources and corresponding biasfield was estimated for the first volume and used for all subsequent time-points. The ASM algorithm was then applied to estimate quantitative susceptibility maps for each time-point as described in Section 5.4.

An axial cross-section of selected susceptibility maps from the resulting time-series is shown in Fig. 6-3 for a representative patient. These results show increasing susceptibility values until the peak of the bolus is reached around volume 70, followed by decreasing susceptibility in the vessels as the agent clears the vasculature. Future

work will focus on quantitative analysis of susceptibility differences in regions of interest before and after anti-angiogenic therapy.

6.1.3 Atlas-based Susceptibility Mapping of Parkinson's Disease

Current treatment of Parkinson's disease (PD) is focused on alleviating symptoms. Although neuroprotective therapies have shown promising results in animal studies, none have proven effective in clinical trials [73]. Berg et al. suggested one reason for the failure of neuroprotection may be that neurodegeneration has advanced to a 60% to 70% reduction of neurons in the substantia nigra (SN) by the time the first clinical symptoms of PD are noticed by the patient [14, 15]. It's possible that neuroprotective strategies would be more effective if they could be initiated before there is substantial cell loss, which would require an ability to non-invasively detect pre-clinical markers of disease.

Recent studies using a form of ultrasound called transcranial sonography (TCS) have shown that hyper-echogenicity may be a valuable marker for SN injury [9, 113, 12, 14]. For example, healthy subjects with SN hyper-echogenicity who underwent fluorine 18-dopa ([18F]-dopa) PET exhibited significantly reduced [18F]-dopa uptake in the striatum, indicating a sub-clinical impairment of the dopaminergic nigral neurons [13]. The similarity in echo pattern of the SN between patients with PD and subjects with sub-clinical impairment of the nigrostriatal system has led to the hypothesis that one of the histological markers seen in PD may also be a causative factor in the increased echogenicity seen in healthy volunteers. A study of 20 post-mortem PD brains that included ultrasound and histopathological analysis, found a positive correlation between iron concentration and echogenicity in the SN [14]. The prevalence of hyper-echogenicity in PD, however, varies between 68% and 99% [113] depending on (1) the definition of hyper-echogenicity, (2) the ultrasound machine and quality of the temporal bone window, and (3) the experience of the investigator [14].

Given the recent success of ASM in detecting iron-dependent susceptibility effects

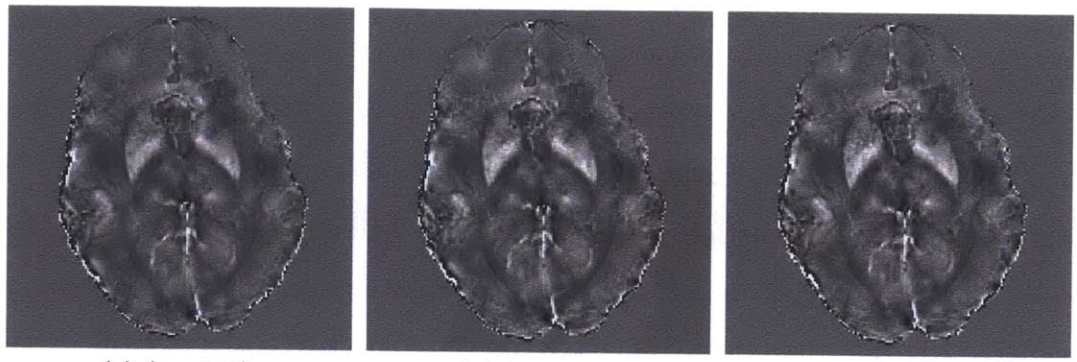

(a) ($t = 001$) (b) ($t = 020$) (c) ($t = 040$)

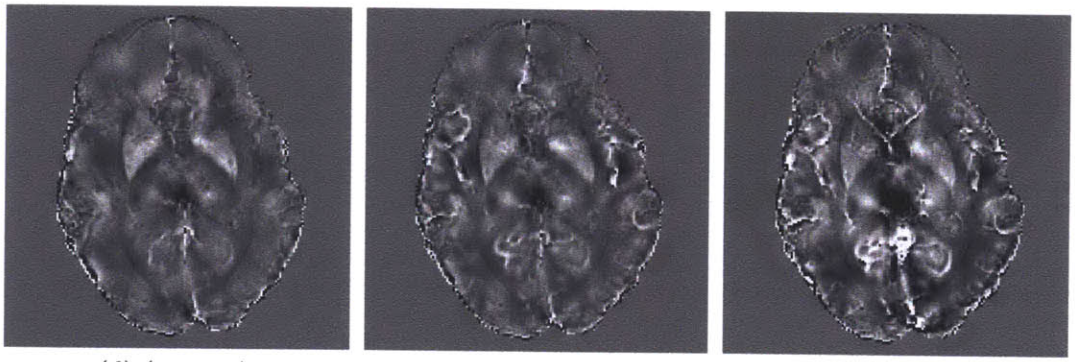

(d) ($t = 060$) (e) ($t = 065$) (f) ($t = 070$)

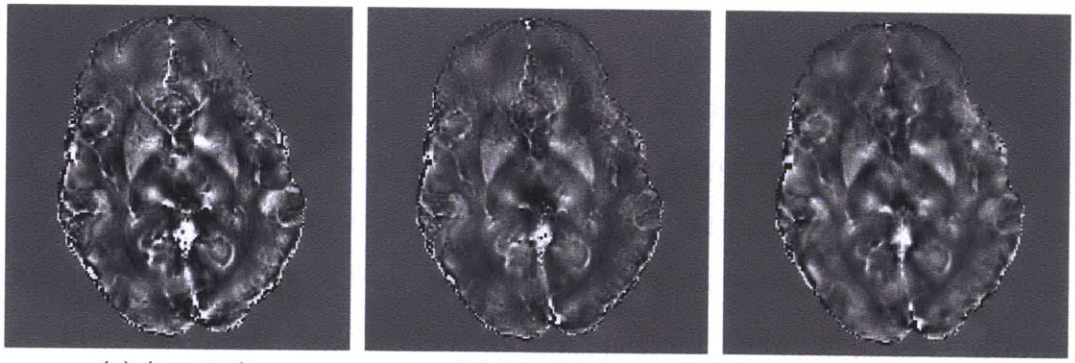

(g) ($t = 075$) (h) ($t = 080$) (i) ($t = 085$)

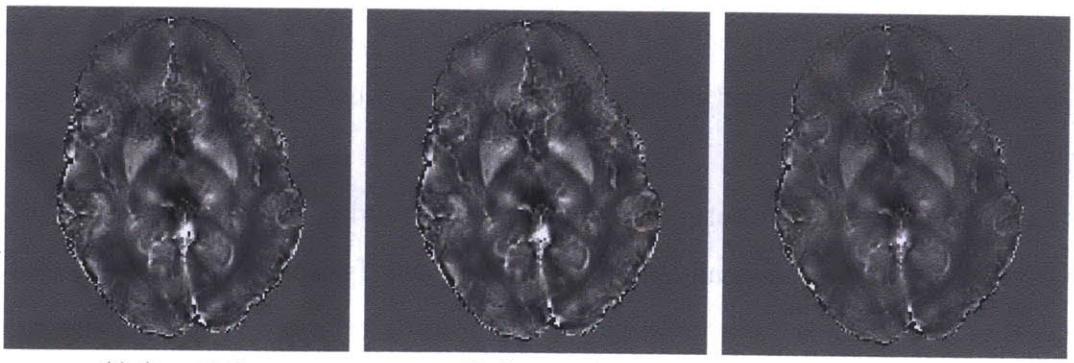

(j) ($t = 090$) (k) ($t = 095$) (l) ($t = 100$)

Figure 6-3: Susceptibility Time-series from Perfusion Data. The scale is $\pm$ 0.2 ppm.

in sub-cortical regions, this method may provide a valuable means for quantifying iron accumulation in Parkinson's patients and those at high risk for developing the disease. If ASM could detect statistically significant differences in SN susceptibility between patients and controls, this could be followed by combined PET/MRI studies. Such studies could elucidate whether subjects with PET findings indicative of pre-clinical PD also show elevated SN susceptibility values. Having a neuroimaging marker for pre-clinical PD that does not require the use of radioactive tracers or the expertise required for TCS could facilitate large-scale studies of healthy subjects at high risk for PD, and hopefully advance the development of neuroprotective drugs.

6.2 Conclusions

In this dissertation we investigated two closely related problems: the calculation of synthetic fieldmaps from tissue/air susceptibility models for distortion correction of EPI data, and the estimation of quantitative susceptibility maps from the inversion of measured fieldmaps. Correcting the distortion in EPI data is necessary for obtaining accurate registration to structural images, which is a fundamental problem in surgical planning, MR-guided intervention, and functional neuroimaging studies. We were interested in computing synthetic fieldmaps for distortion correction since fieldmap-based techniques have been shown to improve registration results and the accuracy of subsequent EPI analysis. Fieldmaps, however, are often not available in clinical studies since they require additional scan time. In addition, acquisition of a single fieldmap may not be sufficient for correcting distortion in EPI time series in which there are motion or respiration effects that cause substantial changes in the field during acquisition.

The calculation of synthetic fieldmaps required solving two related sub-problems: the segmentation of tissue/air susceptibility models from structural MRI and the estimation of unknown shim parameters. Computing accurate tissue/air susceptibility models was neccesary to obtain initial fieldmap estimates using existing forward models. These fieldmaps, however, cannot be applied directly for distortion correc-

tion without an estimate of the shim fields present during EPI acquisition. Both sub-problems were addressed in Chapter 3, and the segmentation methodology was developed further in Chapter 4. In Chapter 3, segmentation experiments showed promising results when an intensity-based classifier was trained with CT and corresponding structural data was obtained on the same scanner as the distorted EPI of the subjects of interest. We developed a novel registration algorithm for estimating unknown shim parameters and obtained final synthetic fieldmaps that agreeded well with measured fieldmaps. Corresponding distortion correction and registration results were also comparable to those obtained with measured fieldmaps, as shown in both fMRI and DTI studies. In Chapter 4 we constructed a tissue/air/bone atlas to serve as a prior on susceptibility values and obtained improved segmentation and synthetic fieldmap results, showing that the classifier generalized well to data acquired at a separate site.

After addressing the problem of susceptibility-based calculation of synthetic fieldmaps for distortion correction of EPI data, we became interested in the inverse problem of estimating susceptibility differences in the brain from measured fieldmaps. This work was motivated by increasing evidence of iron accumulation in specific brain regions due to neurodegenerative disease and normal aging. In Chapter 5, we approached this problem by inverting the spatial formulation of the forward model, which resulted in an expression relating local susceptibility sources to the Laplacian of the observed field and eliminated low frequency biasfields. Inversion of the k-space formulation of the forward model coupled with the use of a tissue/air atlas provided an initial estimate of external biasfields, that allowed for regularization of the susceptibility inversion. This atlas-based susceptibility mapping algorithm showed excellent results when validated against postmortem iron measurements reported in the literature and FDRI collected on the same subjects.

In conclusion, this thesis makes several contributions to the field of medical image analysis. We presented a novel atlas-based classifier for segmentation of structural MRI to obtain tissue/air/bone susceptibility models. We developed a registration algorithm for estimating unknown shim parameters, calculating synthetic fieldmaps

from tissue/air susceptibility models, and correcting distortion in EPI data. We derived a wave equation relating the D'Alembertion of susceptibility to the Laplacian of the observed field, which eliminates low frequency biasfields due to external sources. Finally, we developed an atlas-based susceptibility mapping technique, which uses a tissue/air atlas to resolve ambiguity in the spatial formulation of the forward model and incorporates Fourier-based modeling of external susceptibility sources. ASM-2K results correlated strongly with postmortem iron measurements and showed an age-dependent increase in susceptibility in sub-cortical brain regions. These results suggest that ASM-2K provides a valuable, non-invasive method to quantify iron accumulation in the brain, which may provide insight into the role of iron in the pathophysiology of neurodegenerative disease.

Appendix A

The Fourier Transform of $1/r$

In this appendix, we show that $\mathcal{F}\{\frac{1}{r}\} = \frac{4\pi}{k^2}$. This is obtained using the radial Fourier transform, which is defined in terms of a Hankel transform; therefore we start with the definition of the Hankel transform. The following derivation is summarized from [36]. More detailed descriptions can be found in [2, 102].

A.1 The Hankel transform

A function, $g(r)$, has a Hankel transform, $\tilde{g}_v(k)$, given by:

$$\tilde{g}_v(k) = \int_0^\infty J_v(kr)g(r)rdr \quad . \tag{A.1}$$

The Bessel function, $J_v(kr)$, is defined as:

$$J_v(kr) = \frac{(kr)^v}{(2\pi)^{v+1}}\omega_{2v}\int_0^\pi e^{-ikr\cos(\theta)}\sin(\theta)^{2v}d\theta \quad , \tag{A.2}$$

where,

$$\omega_{2v} = \frac{2\pi^{(2v+1)/2}}{\Gamma((2v+1)/2)} \quad . \tag{A.3}$$

A.2 The Fourier transform in n-dimensions

The Fourier transform in n-dimensions is given by:

$$\tilde{f}(\mathbf{k}) = \int e^{-i\mathbf{k}\cdot\mathbf{x}}f(\mathbf{x})d^n\mathbf{x} \quad , \tag{A.4}$$

where f is a function on $\mathbf{R}^n$, $\mathbf{x} = (x, y, z)$ and in the case of MRI, the components of $\mathbf{k}$ are given by $k_x(t) = \gamma\int G_x(t)\,dt$, $k_y(t) = \gamma\int G_y(t)\,dt$ and $k_z(t) = \gamma\int G_z(t)\,dt$.

The function of interest, $f(\mathbf{x}) = 1/\sqrt{(x^2+y^2+z^2)} = 1/r$ is a radial function since it depends only on the distance of the point $\mathbf{x}$ from the origin [2]. If we let $k_r = \sqrt{(k_x^2+k_y^2+k_z^2)}$, then $f(\mathbf{x})$ and $\tilde{f}(\mathbf{k})$ can be replaced with $F(r)$ and $\tilde{F}(k_r)$, respectively, which are functions of one variable.

A.3 The radial Fourier transform

The Fourier transform of a radial function in n-dimensions is given by:

$$\tilde{F}(k_r) = \frac{(2\pi)^{\frac{n}{2}}}{k_r^{\frac{n-2}{2}}} \int_0^\infty J_{\frac{n-2}{2}}(k_r r) r^{\frac{n-2}{2}} F(r) r dr \quad . \tag{A.5}$$

For $n = 3$, the Bessel function, $J_{\frac{n-2}{2}}$ is given by:

$$J_{\frac{1}{2}}(k_r r) = \frac{(k_r r)^{\frac{1}{2}}}{(2\pi)^{\frac{1}{2}}} 2\pi \int_0^\pi e^{-ik_r r \sin(\theta)} \sin(\theta) d\theta \tag{A.6}$$

$$= \frac{(k_r r)^{\frac{1}{2}}}{(2\pi)^{\frac{1}{2}}} 2 \frac{\sin(k_r r)}{k_r r} \quad . \tag{A.7}$$

If we substitute Eq. A.7 back into Eq. A.5 and set $F(r) = 1/r$, we obtain:

$$\tilde{F}(k_r) = \frac{(2\pi)^{\frac{3}{2}}}{k_r^{\frac{1}{2}}} \int_0^\infty (k_r r)^{\frac{1}{2}} (2\pi)^{\frac{1}{2}} 2 \frac{\sin(k_r r)}{k_r r} r^{\frac{1}{2}} r^{-1} r dr \tag{A.8}$$

$$= \frac{4\pi}{k_r} \int_0^\infty \sin(k_r) dr \quad , \tag{A.9}$$

where $\int_0^\infty \sin(k_r) dr$ is a Fourier sine transform with $f(r) = 1$, which is equal to $1/k_r$ [95]. Substituting this into Eq. A.9, gives:

$$\tilde{F}(k_r) = \frac{4\pi}{k_r^2} \tag{A.10}$$

$$= \frac{4\pi}{k_x^2 + k_y^2 + k_z^2} \quad . \tag{A.11}$$

Bibliography

[1] J.L.R. Andersson, C. Hutton, J. Ashburner, R. Turner, and K. Friston. Modeling geometric deformations in epi time series. Neuroimage, 13:903–919, 2001.

[2] J. Arsac. Fourier Transforms and the Theory of Distributions. Prentice Hall, 1996.

[3] Hallgren B; and Sourander P. The effect of age on the non-haemin iron in the human brain. J Neurochemistry, 3:41–51, 1958.

[4] G. Bartzokis, M. Aravagiri, W.H. Oldendorf, J. Mintz, and S.R. Marder. Field dependent transverse relaxation rate increase may be a specific measure of tissue iron stores. Magn Reson Med, 29(4):459–64, 1993.

[5] G. Bartzokis, M. Beckson, D.B. Hance, P. Marx, J.A. Foster, and S.R. Marder. Mr evaluation of age-related increase of brain iron in young adult and older normal males. Magn Reson Imaging, 15(1):29–35, 1997.

[6] G. Bartzokis, D. Sultzer, J. Mintz, L.E. Holt, P. Marx, C.K. Phelan, and S.R. Marder. In vivo evaluation of brain iron in alzheimer's disease and normal subjects using mri. Biol Psychiatry, 35(7):480–7, April 1994.

[7] P.J. Basser, J. Mattiello, and D. Lebihan. Mr diffusion tensor and imaging. Biophys J, 66:259–267, 1994.

[8] P.J. Basser and C. Pierpaoli. Microstructural and physiological features of tissues elucidated by quantitative-diffusion-tensor mri. J Magn Reson B, 111:209–19, 1996.

[9] G. Becker, J. Seufert, U. Bogdahn, H. Reichmann, and K. Reiners. Degeneration of substantia nigra in chronic parkinsons disease visualized by transcranial color-coded real-time sonography. Neurology, 45:182184, 1995.

[10] T.E. Behrens, M.W. Woolrich, M. Jenkinson, H. Johansen-Berg, R.G. Nunes, S. Clare, P.M. Matthews, J. M. Brady, and S.M. Smith. Characterization and propagation of uncertainty in diffusion-weighted mr imaging. Magn Reson Med, 50(5):1077–88, 2003.

[11] D. Berg. In vivo detection of iron and neuromelanin by transcranial sonography–a new approach for early detection of substantia nigra damage. J Neural Transm, 113(6):775–80, June 2006.

[12] D. Berg. Hyperechogenicity of the substantia nigra: pitfalls in assessment and specificity for parkinson's disease. J Neural Transm, 118(3):453–61, March 2011.

[13] D. Berg, G. Becker, B. Zeiler, O. Tucha, E. Hofmann, M. Preier, P. Benz, W. Jost, K. Reiners, and K. W. Lange. Vulnerability of the nigrostriatal system as detected by transcranial ultrasound. Neurology, 53(5):1026–31, September 1999.

[14] D. Berg, W. Roggendorf, U. Schrder, R. Klein, T. Tatschner, P. Benz, O. Tucha, M. Preier, K.W. Lange, K. Reiners, M. Gerlach, and G. Becker. Echogenicity of the substantia nigra: association with increased iron content and marker for susceptibility to nigrostriatal injury. Arch Neurol, 59(6):999–1005, June 2002.

[15] H. Bernheimer, W. Birkmayer, O. Hornykiewicz, K. Jellinger, and F. Seitelberger. Brain dopamine and the syndromes of parkinson and huntington. clinical, morphological and neurochemical correlations. J Neurol Sci, 20(4):415–55, December 1973.

[16] R. Bhagwandien, M.A. Moerland, C.J. Bakker, R. Beersma, and J.J. Lagendijk. Numerical analysis of the magnetic field for arbitrary magnetic susceptibility distributions in 2d. Magn Reson Imaging, 10(2):299–313, 1992.

[17] R. Bhagwandien, M.A. Moerland, C.J. Bakker, R. Beersma, and J.J. Lagendijk. Numerical analysis of the magnetic field for arbitrary magnetic susceptibility distributions in 3d. Magn Reson Imaging, 12(1):101–7, 1994.

[18] R.W. Bowtell, D.J. McIntyre, M.J. Commandre, P.M. Glover, and P. Mansfield. Correction of geometric distortion in echo planar images. Soc Magn Res Abstr, 2:411, 1994.

[19] G.M. Brittenham, D.E. Farrell, J.W. Harris, E.S. Feldman, E.H. Danish, W.A. Muir, J.H. Tripp, and E.M. Bellon. Magnetic-susceptibility measurement of human iron stores. N Engl J Med, 307(27):1671–5, December 1982.

[20] J.R. Burdo and J.R. Connor. Brain iron uptake and homeostatic mechanisms: an overview. Biometals, 16(1):63–75, 2003.

[21] P.C. Burger, F.S. Vogel, S.F. Green, and T.A. Strike. Glioblastoma multiforme and anaplastic astrocytoma. pathologic criteria and prognostic implications. Cancer, 56(5):1106–11, September 1985.

[22] J.T. Bushberg. The Essential Physics of Medical Imaging Second Edition, volume 30. Lippencott Williams and Wilkins, 2002.

[23] P. Cantillon-Murphy, L.L. Wald, M. Zahn, and E. Adalsteinsson. Measuring spio and gd contrast agent magnetization using 3 t mri. NMR Biomed, 22(8):891–7, Oct 2009.

[24] S. Cha, E.A. Knopp, G. Johnson, S.G. Wetzel, A.W. Litt, and D. Zagzag. Intracranial mass lesions: dynamic contrast-enhanced susceptibility-weighted echo-planar perfusion mr imaging. Radiology, 223(1):11–29, April 2002.

[25] N.K. Chen, K. Oshio, and L.P. Panych. Application of k-space energy spectrum analysis to susceptibility field mapping and distortion correction in gradient-echo epi. Neuroimage, 31:609–622, 2006.

[26] N.K. Chen and A.M. Wyrwicz. Removal of intravoxel dephasing artifact in gradient-echo images using a field-map based rf refocusing technique. MRM, 42:807–812, 1999.

[27] S. Clare, J. Evans, and P. Jezzard. Requirements for room temperature shimming of the human brain. MRM, 55:210–214, 2006.

[28] M.A. Cobleigh, V.K. Langmuir, G.W. Sledge, K.D. Miller, L. Haney, W.F. Novotny, J.D. Reimann, and A. Vassel. A phase i/ii dose-escalation trial of bevacizumab in previously treated metastatic breast cancer. Semin Oncol, 30(5):117–24, October 2003.

[29] C.M. Collins, B. Yang, Q.X. Yang, and M.B. Smith. Three-dimensional mapping of the static magnetic field inside the human head. Magn Reson Imaging, 20(5):413–24, 2002.

[30] R. Cusack, M. Brett, and K. Osswald. An evaluation of the use of magnetic field maps to undistort echo-planar images. Neuroimage, 18:127–142, 2003.

[31] L. de Rochefort, T. Liu, B. Kressler, J. Liu, P. Spincemaille, V. Lebon, J. Wu, and Y. Wang. Quantitative susceptibility map reconstruction from mr phase data using bayesian regularization: validation and application to brain imaging. MRM, 63(1):194–206, Jan 2010.

[32] J. Dennie, J.B. Mandeville, J.L. Boxerman, S.D. Packard, B.R. Rosen, and R.M. Weisskoff. Nmr imaging of changes in vascular morphology due to tumor angiogenesis. Magn Reson Med, 40(6):793–9, December 1998.

[33] G. Deville, M. Bernier, and J. Delrieux. Nmr multiple echoes observed in solid ^{3}he. Phys Rev B, 19:5666–5688, June 1979.

[34] L. Dice. Measures of the amount of ecologic association between species. Ecology, 26(3):297302, 1945.

[35] I. Drobnjak, D. Gavaghan, E. Sli, J. Pitt-Francis, and M. Jenkinson. Development of a functional magnetic resonance imaging simulator for modeling realistic rigid-body motion artifacts. Magn Reson Med, 56(2):364–80, August 2006.

[36] W. G. Faris. Radial functions and the fourier transform. http://math.arizona.edu/~faris/methodsweb/hankel.pdf.

[37] C.T. Farrar, W.S. Kamoun, C.D. Ley, Y.R. Kim, C. Catana, S.J. Kwon, B.R. Rosen, R.K. Jain, and A.G. Sorensen. Sensitivity of mri tumor biomarkers to vegfr inhibitor therapy in an orthotopic mouse glioma model. PLoS One, 6(3):17228, March 2011.

[38] B.M. Fenton, S.F. Paoni, and I. Ding. Effect of vegf receptor-2 antibody on vascular function and oxygenation in spontaneous and transplanted tumors. Radiother Oncol, 72(2):221–30, August 2004.

[39] B. Fischl, A. van der Kouwe, C. Destrieux, E. Halgren, F. Segonne, D. Salat, E. Busa, L. Seidman, J. Goldstein, D. Kennedy, V. Caviness, N. Makris, B. Rosen, and A. Dale. Automatically parcellating the human cerebral cortex. Cerebral Cortex, 14:11–22, 2004.

[40] J. Folkman. Tumor angiogenesis: therapeutic implications. N Engl J Med, 285(21):1182–6, November 1971.

[41] J. Folkman. What is the evidence that tumors are angiogenesis dependent? J Natl Cancer Inst, 82(1):4–6, January 1990.

[42] J. Folkman, P. Cole, and S. Zimmerman. Tumor behavior in isolated perfused organs: in vitro growth and metastases of biopsy material in rabbit thyroid and canine intestinal segment. Ann Surg, 164(3):491–502, September 1966.

[43] G.H. Glover and N.J. Pelc. General Electric Company Milwaukee WI assignee. Method for magnetic field gradient eddy current compensation. U.S. patent 4,698,591, 1987.

[44] E.M. Haacke, M. Ayaz, A. Khan, E.S. Manova, B. Krishnamurthy, L. Gollapalli, C. Ciulla, I. Kim I, F. Petersen, and W. Kirsch. Establishing a baseline phase behavior in magnetic resonance imaging to determine normal vs. abnormal iron content in the brain. J Magn Reson Imaging, 26:256–64, Aug 2007.

[45] E.M. Haacke, R.W. Brown, M.R. Thompson, and R. Venkatensan. Magnetic resonance imaging: physical principles and sequence design. J. Wiley & Sons, 1999.

[46] E.M. Haacke, N.Y. Cheng, M.J. House, Q. Liu, J. Neelavalli, R.J. Ogg, A. Khan, M. Ayaz, W. Kirsch, and A. Obenaus. Imaging iron stores in the brain using magnetic resonance imaging. Magn Reson Med, 23:1–25, Jan 2005.

[47] E.M. Haacke, Y. Xu, Y.C. Cheng, and J.R. Reichenbach. Susceptibility weighted imaging (swi). Magn Reson Med, 52:612–8, Sep 2004.

[48] R.A. Heckemann, J. Hajnal, P. Aljabar, D. Rueckert, and A. Hammers. Automatic anatomical brain mri segmentation combining label propagation and decision fusion. Neuroimage, 33:115–126, 2006.

[49] W.S. Hinshaw and A.H. Lent. An introduction to nmr imaging: From the bloch equation to the imaging equation. Proceedings of the IEEE, 71(3):338–354, March 1983.

[50] J.A. Hopkins and F.W. Wehrli. Magnetic susceptibility measurement of insoluable solids by nmr: magnetic susceptibility of bone. MRM, 37:494, 1997.

[51] H. Huang, C. Ceritoglu, X. Li, A. Qiu, M.I. Miller, P.C. van Zijl, and S. Mori. Correction of b0 susceptibility induced distortion in diffusion-weighted images using large-deformation diffeomorphic metric mapping. Magn Reson Imaging, 26(9):1294–302, November 2008.

[52] H. Hurwitz, L. Fehrenbacher, W. Novotny, T. Cartwright, J. Hainsworth, W. Heim, J. Berlin, A. Baron, S. Griffing, E. Holmgren, N. Ferrara, G. Fyfe, B. Rogers, R. Ross, and F. Kabbinavar. Bevacizumab plus irinotecan, fluorouracil, and leucovorin for metastatic colorectal cancer. N Engl J Med, 350(23):2335–42, June 2004.

[53] C. Hutton, A. Bork, O. Josephs, R. Deichmann, J. Ashburner, and R. Turner. Image distortion correction in fmri: A quantitative evaluation. Neuroimage, 16:217–240, 2002.

[54] J.D. Jackson. Classical Electrodynamics Third Edition, volume 67. Wiley, 1998.

[55] R.K. Jain. Normalizing tumor vasculature with anti-angiogenic therapy: a new paradigm for combination therapy. Nat Med, 7(9):987–9, September 2001.

[56] R.K. Jain. Normalization of tumor vasculature: an emerging concept in antiangiogenic therapy. Science, 307(5706):58–62, January 2005.

[57] K. Jellinger, W. Paulus, I. Grundke-Iqbal, P. Riederer, and M.B. Youdim. Brain iron and ferritin in parkinson's and alzheimer's diseases. J Neural Transm Park Dis Dement Sect, 2(4):327–40, 1990.

[58] M. Jenkinson. Fast, automated, n-dimensional phase-unwrapping algorithm. MRM, 49(1):193–7, 2003.

[59] M. Jenkinson. Improving the registration of b0-disorted epi images using calculated cost function weights. Tenth Int. Conf. on Functional Mapping of the Human Brain, 2004.

[60] M. Jenkinson, P. Bannister, M. Brady, and S. Smith. Improved optimisation for the robust and accurate linear registration and motion correction of brain images. Neuroimage, 17:825–841, 2 2002.

[61] M. Jenkinson and S.M. Smith. A global optimisation method for robust affine registration of brain images. Medical Image Analysis, 5:143–156, 2 2001.

[62] M. Jenkinson, J.L. Wilson, and P. Jezzard. Perturbation method for magnetic field calculations of nonconductive objects. MRM, 52(3):471–477, Sep 2004.

[63] P. Jezzard and R.S. Balaban. Correction for geometric distortion in echo planar images from b0 field variations. MRM, 34:65–73, 1995.

[64] P. Jezzard and S. Clare. Sources of distortion in functional mri data. Human Brain Mapping, 8:80–85, 1999.

[65] D.B. Keator, J.S. Grethe, D. Marcus, B. Ozyurt, S. Gadde, S. Murphy, S. Pieper, D. Greve, R. Notestine, H.J. Bockholt, P. Papadopoulos, BIRN Function, BIRN Morphometry, and BIRN-Coordinating. A national human neuroimaging collaboratory enabled by the biomedical informatics research network (birn). IEEE Trans Inf Technol Biomed, 12(2):162–72, 2008.

[66] C.G. Koay, J.D. Carew, A.L. Alexander, P.J. Basser, and M.E. Meyerand. Investigation of anomalous estimates of tensor-derived quantities in diffusion tensor imaging. Magn Reson Med, 55(4):930–6, 2006.

[67] KM. Koch, X. Papademetris, D. Rothman, and R.A. de Graaf. Rapid calculations of susceptibility-induced magnetostatic field perturbations for in vivo magnetic resonance. Phys Med Biol, 51:6381–6402, 2006.

[68] S.H. Koenig, R.D. Brown 3rd, J.F. Gibson, R.J. Ward, and T.J. Peters. Relaxometry of ferritin solutions and the influence of the fe3+ core ions. Magn Reson Med, 3(5):755–67, October 1986.

[69] S.H. Koenig, C.M. Baglin, and R.D. Brown 3rd. Magnetic field dependence of solvent proton relaxation in aqueous solutions of fe3+ complexes. Magn Reson Med, 2(3):283–8, June 1985.

[70] A.H. Koeppen. The history of iron in the brain. J Neurol Sci, 134:1–9, 1995.

[71] P. Konzbul and K. Sveda. Shim coils for nmr and mri solenoid magnets. Meas Sci Technol, 6:1116–1123, 1995.

[72] M.A. Kurian, A. McNeill, J.P. Lin, and E.R. Maher. Childhood disorders of neurodegeneration with brain iron accumulation (nbia). Dev Med Child Neurol, 53(5):394–404, 2011.

[73] J.W. Langston, I. Irwin, E.B. Langston, and L.S. Forno. Pargyline prevents mptp-induced parkinsonism in primates. Science, 225(4669):1480–2, September 1984.

[74] S. Larsen, R. Kikinis, I.F. Talos, D. Weinstein, W. Wells, and A. Golby. Quantitative comparison of functional mri and direct electrocortical stimulation for functional mapping. Int J Med Robot, 3(3):262–70, 2007.

[75] H. Lassmann. Mechanisms of neurodegeneration shared between multiple sclerosis and alzheimer's disease. J Neural Transm, 118(5):747–52, 2011.

[76] L. Li and J.S. Leigh. High-precision mapping of the magnetic field utilizing the harmonic function mean value property. J Magn Reson, 148:442–8, Feb 2001.

[77] S. Li, B.J. Dardzinski, C.M. Collins, Q.X. Yang, and M.B. Smith. Three-dimensional mapping of the static magnetic field inside the human head. Magn Reson Imaging, 36(5):705–14, 1996.

[78] T. Liu, I. Khalidov, L. de Rochefort, R. Spincemaille, J. Liu, and Y. Wang. Improved background field correction using effective dipole fitting. Proc ISMRM, 18, 2010.

[79] T. Liu, P. Spincemaille, L. de Rochefort, B. Kressler, and Y. Wang. Calculation of susceptibility through multiple orientation sampling (cosmos): a method for conditioning the inverse problem from measured magnetic field map to susceptibility source image in mri. Magn Reson Med, 61:196–204, Jan 2009.

[80] M. Lustig, D. Donoho, and J.M. Pauly. Sparse mri: The application of compressed sensing for rapid mr imaging. MRM, 58(6):1182–95, December 2007.

[81] J. Ma, S. Pulfer, S. Li, J. Chu, K. Reed, and J.M. Gallo. Pharmacodynamic-mediated reduction of temozolomide tumor concentrations by the angiogenesis inhibitor tnp-470. Cancer Res, 61(14):5491–8, July 2001.

[82] P. Mansfield. Multi-planar image formation using nmr spin-echoes. J. Phys. C: Solid State Phys, 10:L55L58, 1977.

[83] J.P. Marques and R. Bowtell. Evaluation of a fourier-based method for calculating susceptibility induced magnetic field perturbations. Proc ISMRM, 11:1020, 2003.

[84] J.P. Marques and R. Bowtell. Application of a fourier-based method for rapid calculation of field inhomogeneity due to spatial variation of magnetic susceptibility. Concepts in Magnetic Resonance Part B, 25(1):6578, 2005.

[85] A. McNeill and P.F. Chinnery. Neurodegeneration with brain iron accumulation. Handb Clin Neurol, 100:161–72, 2011.

[86] R. Murata, Y. Nishimura, and M. Hiraoka. An antiangiogenic agent (tnp-470) inhibited reoxygenation during fractionated radiotherapy of murine mammary carcinoma. Int J Radiat Oncol Biol Phys, 37(5):1107–13, March 1997.

[87] D.C. Noll, C.H. Meyer, J.M. Pauly, D.G. Nishimura, and A. Macovski. A homogeneity correction method for magnetic resonance imaging with time varying gradients. IEEE Trans Med Im, 10:629–637, 1991.

[88] S. Ogawa, T.M. Lee, A.R. Kay, and Tank D.W. Brain magnetic resonance imaging with contrast dependent on blood oxygenation. Proc. Natl. Acad. Sci. U. S. A., 87(24):9868–72, 1990.

[89] S.H. Koenig P. Gillis. Transverse relaxation of solvent protons induced by magnetized spheres: application to ferritin, erythrocytes, and magnetite. Magn Reson Med, 5(4):323–45, October 1987.

[90] G. Perry, L.M. Sayre, C.S. Atwood, R.J. Castellani, A.D. Cash, C.A. Rottkamp, and M.A. Smith. The role of iron and copper in the aetiology of neurodegenerative disorders: therapeutic implications. CNS Drugs, 16(5):33952, 2002.

[91] A. Pfefferbaum, E. Adalsteinsson, T. Rohlfing, and E.V. Sullivan. Mri estimates of brain iron concentration in normal aging: comparison of field-dependent (fdri) and phase (swi) methods. Neuroimage, 47:493–500, Aug 2009.

[92] K. Pohl, S. Bouix, R. Kikinis, and W. Grimson. Anatomical guided segmentation with nonstationary tissue class distributions in an expectation-maximization framework. ISBI, pages 81–84, 2004.

[93] Mayer RJ. Two steps forward in the treatment of colorectal cancer. N Engl J Med, 350(23):2406–8, June 2004.

[94] G.K. Rohde, A.S. Barnett, P.J. Basser, S. Marenco, and C. Pierpaoli. Comprehensive approach for correction of motion and distortion in diffusion-weighted mri. Magnetic Resonance in Medicine, 51:103–114, 2004.

[95] D. Saintillan. Fourier transforms. `http://mechse.illinois.edu/research/dstn/teaching_files2/fouriertransforms.pdf`.

[96] R. Salomir, B. D. de Senneville, and C.T.W. Moonen. A fast calculation method for magnetic field inhomogeneity due to an arbitrary distribution of bulk susceptibility. Concepts in Magnetic Resonance Part B, 19:26–34, 2003.

[97] F. Schweser, M. Atterbury, A. Deistung, B.W. Lehr, K. Sommer, and J.R. Reichenbach. Harmonic phase subtractionmethods are prone to b1 background components. Proc ISMRM, 19, 2011.

[98] F. Schweser, A. Deistung, B.W. Lehr, and J.R. Reichenbach. Quantitative imaging of intrinsic magnetic tissue properties using mri signal phase: an approach to invivo brain iron metabolism. Neuroimage, 54:2789–807, Feb 2011.

[99] J. Schwinger, L. DeRaad Jr, K.A. Milton, and W.Y.Tsai. Classical Electrodynamics. Perseus Books, 1998.

[100] S. Smith. Fast robust automated brain extraction. Human Brain Mapping, 17:143–155, 2002.

[101] S.M. Smith, M. Jenkinson, M.W. Woolrich, C.F. Beckmann, T.E.J. Behrens, H. Johansen-Berg, P.R. Bannister, M. De Luca, I. Drobnjak, D.E. Flitney, R. Niazy, J. Saunders, J. Vickers, Y. Zhang, N. De Stefano, J.M. Brady, and P.M. Matthews. Advances in functional and structural mr image analysis and implementation as fsl. NI, 23(1):209–219, 2004.

[102] I. N. Sneddon. Fourier Transforms. McGraw-Hill, 1951.

[103] A. Sodickson and D. G. Cory. A generalized k-space formalism for treating the spatial aspects of a variety of nmr experiments. Progress in Nuclear Magnetic Resonance Spectroscopy, 33:77–108, 1998.

[104] E.O. Stejskal and J.E. Tanner. Spin diffusion measurements: spin echos in the presence of a time dependent field gradient. J Chem Phys, 42:288292, 1965.

[105] E.C. Theil. The ferritin family of iron storage proteins. Adv Enzymol Relat Areas Mol Biol, 63:421–49, 1990.

[106] K.R. Thulborn, A.G. Sorensen, N.W. Kowall, A. McKee, A. Lai, R.C. McKinstry, J. Moore, B.R. Rosen, and T.J. Brady. The role of ferritin and hemosiderin in the mr appearance of cerebral hemorrhage: a histopathologic biochemical study in rats. Am J Neuroradiol, 11(2):291–7, 1990.

[107] P.S. Tofts. Modeling tracer kinetics in dynamic gd-dtpa mr imaging. J Magn Reson Imaging, 7(1):91–101, January 1997.

[108] P.S. Tofts, G. Brix, D.L. Buckley, J.L. Evelhoch, E. Henderson, M.V. Knopp, H.B. Larsson, T.Y. Lee, N.A. Mayr, G.J. Parker, R.E. Port, J. Taylor, and R.M. Weisskoff. Estimating kinetic parameters from dynamic contrast-enhanced t(1)-weighted mri of a diffusable tracer: standardized quantities and symbols. J Magn Reson Imaging, 10(3):223–32, September 1999.

[109] P.S. Tofts and A.G. Kermode. Measurement of the blood-brain barrier permeability and leakage space using dynamic mr imaging. 1. fundamental concepts. Magn Reson Med, 17(2):357–67, February 1991.

[110] D. Tosun, M. Rettmann, X. Han, X. Tao, C. Xu, S. Resnick, D. Pham, and J. Prince. Cortical surface segmentation and mapping. Neuroimage, 23:108–118, 2004.

[111] I. Troprs, S. Grimault, A. Vaeth, E. Grillon, C. Julien, J.F. Payen, L. Lamalle, and M. Dcorps. Vessel size imaging. Magn Reson Med, 45(3):397–408, March 2001.

[112] T.K. Truong, B.D. Clymer, D.W. Chakeres, and P. Schmalbrock. Three-dimensional numerical simulations of susceptibility-induced magnetic field inhomogeneities in the human head. Magn Reson Imaging, 20(10):759–70, 2002.

[113] A.M. Vlaar, A. Bouwmans, W.H. Mess, S.C. Tromp, and W.E. Weber. Transcranial duplex in the differential diagnosis of parkinsonian syndromes: a systematic review. J Neurol, 256:530538, 2009.

[114] L. Wald. Mr image encoding. Lecture Notes from MIT Course HST.584J Magnetic Resonance Analytic, Biochemical, and Imaging Techniques.

[115] L. Wald. Mr physics for fmri and dti. Presented at the 15th Annual Meeting of the Organization for Human Brain Mapping, San Francisco, CA, 2009.

[116] X. Wan, G.T. Gullbert, and D.L. Parker. Reduction of geometric distortion in echo-planar imaging using a multi-reference scan. Soc Magn Res Abstr, 3:103, 1995.

[117] Y. Wang, Y. Yu, D. Li, K.T. Bae, J.J. Brown, W. Lin, and E.M. Haacke. Artery and vein separation using susceptibility-dependent phase in contrast-enhanced mra. J Magn Reson Imaging, 12:661–70, Nov 2000.

[118] R.M. Weisskoff and T.L. Davis. Correcting gross distortion on echo planar images. Soc Magn Res Abstr, 11:4515, 1992.

[119] R.M. Weisskoff and S. Kiihne. Quantitative susceptibility map reconstruction from mr phase data using bayesian regularization: validation and application to brain imaging. MRM, 24(2):375–83, Apr 1992.

[120] W.M. Wells, W.E.L. Grimson, R. Kikinis, and F.A. Jolesz. Adaptive segmentation of mri data. IEEE Trans Med Imag, 15(4):429–442, 1996.

[121] M. Wu, L.C. Chang, L. Walker, H. Lemaitre, A.S. Barnett, S. Marenco, and C. Pierpaoli. Comparison of epi distortion correction methods in diffusion tensor mri using a novel framework. LNCS MICCAI, 11(6):321–9, 2008.

[122] J.C. Yang, L. Haworth, R.M. Sherry, P. Hwu, D.J. Schwartzentruber, S.L. Topalian, S.M. Steinberg, H.X. Chen, and S.A. Rosenberg. A randomized trial of bevacizumab, an anti-vascular endothelial growth factor antibody, for metastatic renal cancer. N Engl J Med, 349(5):427–34, July 2003.

[123] B. Yao, T.Q. Li, P. Gelderen, K. Shmueli, J.A. de Zwart, and J.H. Duyn. Susceptibility contrast in high field mri of human brain as a function of tissue iron content. Neuroimage, 44:1259–66, Feb 2009.

[124] L. Zecca, D. Berg, T. Arzberger, P. Ruprecht, W.D. Rausch, M. Musicco, D. Tampellini, P. Riederer, M. Gerlach, and G. Becker. In vivo detection of iron and neuromelanin by transcranial sonography: a new approach for early detection of substantia nigra damage. Mov Disord, 20(10):1278–85, October 2005.

[125] L. Zecca, M.B. Youdim, P. Riederer, J.R. Connor, and R.R. Crichton. Iron, brain ageing and neurodegenerative disorders. Nat Rev Neurosci, 5:863–73, Nov 2004.

[126] L. Zollei, M. Shenton, W. Wells, and K. Pohl. The impact of atlas formation methods on atlas-guided brain segmentation. MICCAI, 2007.

[127] I.G. Zubal, C.R. Harrell, E.O. Smith, Z. Rattner, G.R. Gindi, and P.B. Hoffer. Computerized three-dimensional segmented human anatomy. Med Phys, 21:299–302, 1994.